To my mom and dad.

Julien Chaput
New Mexico Institute of Mining and Technology
December, 2012

Scattered Wavefield Studies in West Antarctica and at Erebus Volcano

by

Julien Chaput

Submitted in Partial Fulfillment

of the Requirements for the Degree of

Doctor of Philosophy in Earth and Environmental Science with Dissertation in Geophysics

New Mexico Institute of Mining and Technology

Socorro, New Mexico

December, 2012

ABSTRACT

Correctly interpreting complex scattered wavefields to recover meaningful information about a medium is one of the most fundamental issues broached by seismologists. Such studies encompass the full spectrum of frequencies presented by seismic signals, and methods to identify coherency from otherwise chaotic looking signatures vary as broadly as do the studied scales and media. This body of work investigates the use of two different branches of scattered wavefield experiments conducted on very different scales. Works detailing high frequency coda-related seismic interferometry applied to Erebus volcano on Ross Island, Antarctica, and P-wave receiver functions applied to the whole of West Antarctica are developed, with a variety of innovations and implications for future imaging efforts.

Chapters 1 through 3 detail the results of a novel pseudo-reflection technique based on recently identified theoretical principles pertaining to the recovery of specular information from multiply scattered wavefields. Wavefield modal equipartitioning in the coda of high frequency transient signals such as icequakes and Strombolian eruptions is identified at Erebus volcano using a small dense array, thus demonstrating the satisfaction of theoretical requirements for Green's function recovery via seismic interferometry. Green's function estimates are calculated from the coda of Strombolian eruptions using 94 stations from dense broadband and short period arrays deployed during the 2007-2009 field seasons. Using

a rotation approach, the Green's functions are shaped and then back-propagated into the volcanic edifice, and the resulting scattering intensity depth slices are compared to concurrent active source tomography slices to image and assess the character of the magmatic system. The resulting image suggests a sharply W-NW off-axis bifurcating shallow conduit system with a gradual re-centralization at depths greater than 1 km. Furthermore, Green's function estimates were also calculated at the long running Mount Erebus Volcanic Observatory permanent network from 2005-2011, displaying substantial temporal variability that shows some associations with changes in VLP-SP timing lags. Several such changes are identified, and associated Green's function features are back-propagated into the previous scattering model to identify regions of the volcano that are most sensitive to structural change affecting eruptive behavior.

Chapter 4 describes the application of P-receiver functions (PRFs) to 35 broadband stations deployed in the POLENET project, a multi-institutional IPY NSF venture to characterize the structural and evolutionary behavior of West Antarctica and the West Antarctic Rift System (WARS). Most stations in West Antarctica are deployed over thick ice sheets, creating high amplitude receiver function multiples that do not decay quickly, thus complicating efforts to identify conventionally interpreted converted phases (particularly from the Moho). Furthermore, ice sheet thickness estimates in West Antarctica are sparse, thus not permitting a direct constraint of this layer for a synthetic model in many instances. We design an approach based on a combination of forward modeling to determine rough prior models, and a regularized Markov Chain Monte Carlo approach to invert the waveforms for deeper structure. We also jointly merge results from surface wave tomography with the results from our PRFs to generate a new crustal

map of Antarctica. We find that crustal thicknesses across West Antarctica are generally thin, with modest thickening into the Marie Byrd Land dome (MBL) and under the Ellsworth mountains. Crustal thinning observed under deep sub-glacial basins in West Antarctica is indicative of ductile thinning in response to extension of the WARS. When corrected for elevation, these basins are shown to be largely compensated in the crust, suggestive of a cool, stable upper mantle under the WAIS, while crustal thinning in the MBL dome and Trans-Antarctic Mountains is indicative of mantle compensation in light of the elevation of these features. Body wave tomography has revealed a low velocity anomaly under the MBL that does not seem to extend under the WAIS, thus bolstering our results.

Keywords: Seismic interferometry; receiver functions; West Antarctica; Erebus volcano; seismic imaging

ACKNOWLEDGMENTS

Foremost, I'd like to thank my advisor Rick Aster for his constant support and advice through the good results and the bad. I'd also like to thank my committee, Dr. Philip Kyle, Dr. William McIntosh, Dr. Susan Bilek, and Dr. Brian Borchers, who have when necessary steered me towards more focused ideas, and allowed this end product to take shape. I promise to bring a truly lovely cake for my defense. This research could not have been possible without the support of IRIS PASSCAL and UNAVCO employees, as well as the NSF Office of Polar Programs, Raytheon Polar Services, and the Mount Erebus and POLENET field teams over the seasons. Funding for these studies was provided by the National Science Foundation Office of Polar Programs grant numbers 0538414, and 0632185. Finally, to my colleagues and friends, thanks for putting up with my antics, my general reclusiveness, and my overzealous need to climb objects, natural or otherwise. To my parents, I'll always be 10 years old. Thanks for not making me grow up. This work is for you.

This dissertation was typeset with LaTeX[1] by the author.

[1]The LaTeX document preparation system was developed by Leslie Lamport as a special version of Donald Knuth's TeX program for computer typesetting. TeX is a trademark of the American Mathematical Society. The LaTeX macro package for the New Mexico Institute of Mining and Technology dissertation format was written for the Tech Computer Center by John W. Shipman.

CONTENTS

LIST OF TABLES

LIST OF FIGURES

This dissertation is accepted on behalf of the faculty of the Institute by the following committee:

Richard Aster, Advisor

I release this document to the New Mexico Institute of Mining and Technology.

Julien Chaput Date

PREFACE

The subject of volcanic seismology is not only the most beautiful and spectacular, but also the most difficult to study of all the subjects seismologists have encountered on Earth. This is because seismic sources in volcanoes involve dynamic motion of gas, fluid, and solid, and propagation paths in volcanoes are usually extremely heterogeneous, anisotropic, and absorptive, with irregular topographies and interfaces including cracks of all scales and orientations. Thus, volcanic seismology is the most challenging to seismologists, requiring ingenuity in designing experiments and interpreting observations.
-Kei Aki

GENERAL INTRODUCTION

Studies of scattered wavefields constitute perhaps the most expansive branch of explored seismological tools for the study of complex media. Whereas travel-time based methodologies tend to either ignore the lengthy scattered coda of a typical recorded seismic signal (e.g. active or passive P or S wave body wave tomography [*Zandomeneghi et al.,* 2012, *Nyblade,* 2011]), or simply use very low frequency bands that are far less sensitive to small scale structures, scattering methodologies seek to analyze energy incident after the first onset of the seismogram. Such methods range from rigorously controlled industrial active-source reflection experiments [*Clowes et al.,* 2005, *Rost and Thomas,* 2002], largely pioneered by the oil and gas industry, to the use of well documented converted/reflected arrivals from known discontinuities deep within the earth's crust and mantle regions (e.g. receiver functions [*Wilson et al.,* 2005, *Winberry,* 2004, *Ammon,* 1991]), to the use of more exotic statistical approaches such as coda envelope beamforming [*Hong,* 2012], seismic interferometry [*Campillo,* 2003, *Wapenaar,* 2006, *Snieder,* 2004], and other such applications of multiply scattered wavefields [*Margerin et al.,* 2000, *Barros et al.,* 2012]. A given approach is generally selected based on the availability of sources/stations, the frequency content of the signals of interest, and perhaps most importantly, the properties of the medium itself and the scale of its internal structures.

This dissertation encompasses the development and application of several of these techniques in two drastically different problems in Antarctica. Firstly, a novel study of the multiply scattered coda of Strombolian eruptions on Erebus volcano, Ross Island, Antarctica, and a full method detailing how it is possible to recover a high resolution pseudo-reflection image of Erebus' magmatic system will be presented. Subsequently, through the use of temporally/spatially resampled arrays, it will be demonstrated that this sort of approach is theoretically and practically robust, and that it may be used to constrain details concerning the structural and temporal evolution of Erebus. This work paves the way towards real-time passive structural monitoring of actively deforming systems with a much higher resolution than many methods put forth to date, such as tomography [*Zandomeneghi et al.,* 2012, *Nyblade,* 2011].

Secondly, in the scope of the POLENET project, P-wave receiver functions [*Ammon,* 1991, *Wilson et al.,* 2005] were applied to a large network of seismic stations deployed throughout West Antarctica to constrain crustal structure to better under understand the behavior of the West Antarctic Ice Sheet (WAIS) and the underlying West Antarctic Rift System (WARS). P-wave receiver functions suffer from a great increase in complexity if stations are located on a kilometers-thick ice sheet, such as covers most of West Antarctica, and so an approach for dealing with this issue was developed to constrain both ice thickness and crustal properties.

Figure 1 of this introductory section demonstrates the entirety of the studied area in this dissertation, with annotated features that will be referred to throughout all four chapters.

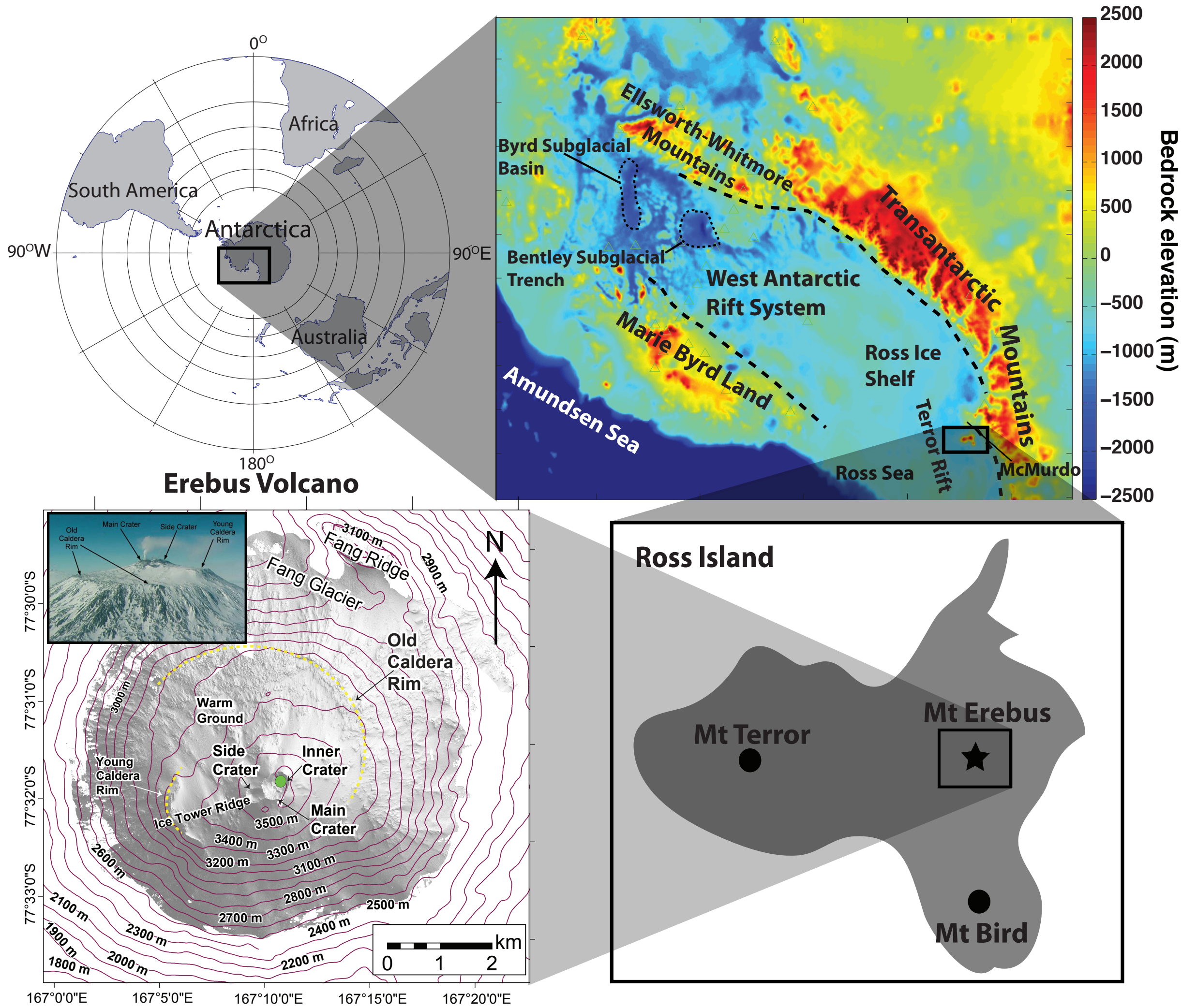

Figure 1: Map of the studied area. Mt Erebus is located on Ross Island, which lies in the Southern portion of the West Antarctic Rift System. Ross Island is thought to be a surface expression of plume activity underlying the Terror Rift, which is the current region of extension of the West Antarctic Rift System, which in turn underlies most of West Antarctica. Note that the Victoria Land Basin, which lies south of the Terror Rift in panel 2 and will be referred to, is not indicated on this map.

Erebus volcano: Background and previous works

Erebus volcano (77.32°S, 167.10°E), is a 3794 m stratovolcano situated on Ross Island, Antarctica [*Oppenheimer and Kyle*, 2008]. The volcano features a summit crater hosting one of Earth's few persistent lava lakes. The uppermost portion of the volcano (above 3000 m), approximately 70 ka in age, is composed of heterogeneous layered lava flows, bomb accumulations, and pyroclastic deposits [*Panter and Winter*, 2008], and some near-surface permafrost layers, firn, and small glaciers. The volcano is currently active, and has produced small (VEI 0) Strombolian eruptions, with highly variable frequency of occurrence and average intensity, for at least four decades [*Giggenbach*, 1973, *Rowe et al.*, 1998, *Aster et al.*, 2003, *Jones et al.*, 2008, *Aster et al.*, 2008] from several vents within the 80-m radius inner crater. Strombolian eruptions on Erebus are overwhelmingly generated via explosive decompression of large sequestered gas slugs rising through the conduit system [*Gerst et al.*, 2008], although ash-vent eruptions and potential rare volcanic tremor have also been observed. The persistent crater morphology, eruptive activity, growth of large anorthoclase phenocrysts and long-lived lava lake are indicators of a substantial quasi-stable near-summit magmatic system with a lifetime of at least many decades. Studies of very-long-period seismic signals associated with eruptive gas slug ascent and lava lake recovery [*Knox*, 2012, *Rowe et al.*, 1998, *Aster et al.*, 2003] further suggest a near-summit magmatic conduit system with significant geometrical complexity in the uppermost few hundreds meters below the lava lake. The volcano has been monitored by a multidecadal network of short period and broadband seismic stations [*Aster et al.*, 2004], abetted by denser focused seasonal deployments [*Rowe et al.*, 1998, *Aster et al.*, 2003, *Zandomeneghi et al.*, 2012].

The tectonic and volcanic evolution of Mt Erebus is closely related to the evolution of the Ross Sea and Ross Ice Shelf. The Ross Sea itself is formed by at least 3 major rift basins, which were formed during two periods of extension, the youngest of the which being the Terror rift, subject to current extension. Alongside the extension in the Ross Sea, volcanism in the area begun with volcanic activity at the base of Mt Morning (12.4 to 18.7 Ma), then moving to Minna Bluff and towards Mt Discovery (4.4 Ma to 11 Ma). Ross Island then subsequently formed, with associated volcanism propagating from Mt Bird, to Mt Terror, to Hut Point Peninsula and finally to Mt Erebus where it currently resides [*Kyle,* 1990]. The thinned crust near the TAM and the low velocity anomaly as shown by [*Wiens,* 2006, *Bannister et al.,* 2003] are supportive of hotspot volcanism as a model for Erebus.

Mt Erebus has undergone 3 major stages of eruptive activity. The first, as inferred by geochronological studies [*Esser et al.,* 2004, *Kyle,* 1990] presents the transition from sub-aqueous to sub-aerial volcanism at around 1.3 Ma, and displays 300,000 years of basanitic to phonotephritic volcanism, which built a broad shield dome. At $\sim$1 Ma, volcanism on Erebus was characterized by eruptions on Fang Ridge, which then migrated to the present day vent at $\sim$243,000 years, marking the initiation of current Erebus activity, which is composed largely of anorthoclase tephriphonolite flows. Several trachytic flows were observed around 160,000 years, generated by a pulse of effusive activity with crustal contamination. [*Kyle et al.,* 2008] suggests that a simple mantle plume model for Erebus may be insufficient, given the widespread presence of an unusual HIMU (radiogenic Pb isotope) signature in Antarctic volcanism in general, and [*Panter et al.,* 2006] propose instead a model in which the HIMU signature is a property of a thick lithospheric mantle without asthenospheric upwell.

Prior to the recent dense deployments of 2007-2009 and the installation of the current Mount Erebus Volcanic Observatory (MEVO) permanent network, several sparse seismic studies including refraction, tomography, and teleseismic measurements were performed on Erebus [*Dibble et al.*, 1982, *Dibble et al.*, 1994, *Shibuya et al.*, 1983] with a goal to determine bulk structure and an approximate velocity model for the edifice and surrounding area. From these general results, a P-wave velocity of $\sim$ 1.2-1.4 km/s for the summit region of Erebus (e.g. top 300 meters) was inferred, as well as P-wave velocities between 2-4.5 km/s for the rest of the volcano and immediately surrounding areas. Further studies by [*Dibble*, 1994] featuring more involved refraction lines, eruptions, and teleseisms, produced a better estimate of Erebus' bulk velocity structure, which averaged 4.1-4.3 km/s under an inferred $\sim$360 m thick permafrost layer with a velocity of 1-2 km/s. [*Dibble*, 1994] however also estimated the velocity of the magma column underlying the lake by sampling lava bombs and producing bubble-growth models to fit Erebus specific conditions. As such, a P-wave velocity of 2 km/s was estimated for the deeper magma column.

With the advent of more permanent broadband deployments through MEVO [*Aster et al.*, 2004], consisting of 6 broadband seismometers supplemented by an array of short period sensors and infrasound emplacements, cataloging of Strombolian eruptions and other local seismic signals (e.g. icequakes, iceberg tremor [*Knox*, 2012, *Ruiz*, 2003]) became possible, and along with recorded bubble burst signals (SP), a Very Long Period (VLP) signal associated with post-eruptive reload and re-stabilization was identified [*Rowe et al.*, 1998, *Aster et al.*, 2003]. VLP moment tensor inversion studies using a database of well-recorded eruptions were performed, suggesting a VLP source significantly offset to the west by northwest from the lava lake by $\sim$450 m and residing at a depth of $\sim$500 m, thus presenting the first concrete evidence that the conduit system of Erebus volcano is highly asymmetric, and that the upper conduit system may be particularly complex. Furthermore, geochemical studies of gas populations at the main lava lake and a secondary lake (Werner's lake) [*Oppenheimer and Kyle*, 2008] revealed notably different contents, suggesting that these two vents, separated by $\sim$50 meters are fed by two distinct shallow conduits, further supporting the idea of a highly complex magmatic system. Furthermore, the assembly of a large database of eruptions through the use of a multi-station matched filter encompassing the MEVO array and infrasound sensors allowed for meticulous computations of the timing lags between the VLP and the SP signals. Systematic changes, both abrupt and long period, were noted in the lags, and it is hypothesized that these changes reflect some degree of structural alteration in the slug generating conduit system [*Knox*, 2012].

The objectives of this portion of the project are exploratory in nature. The results of two first author peer reviewed (or to be reviewed shortly) publications are presented, along with preliminary results for a third publication, all as distinct Chapters for Erebus studies. The first Chapter presents in-progress studies of Erebus coda and scattering characteristics, and more importantly, the association between coda structure and the theoretical recovery of the impulse response of the volcano. The second Chapter details a novel approach featuring the recovery of specular scattering information at a large network of broadband and short period stations deployed during the 2007-2009 filed seasons. A robust internal scattering model for Erebus volcano is recovered, and along with it, detailed interpretations of the inner workings of the magmatic system. The third Chapter denotes an extension to this approach at the MEVO permanent network, with a goal of studying the temporal variability of the impulse responses (Green's functions) during peak eruptive periods from 2005-2011. We find suggestion of correlation between variations in distinct arrivals in the Green's functions and the previously mentioned VLP-SP timing differences. Given the nature of this pseudo-reflection approach, we are furthermore able to back propagate discrete arrivals in 3D so as to better localize and understand structures that were most affected over time.

West Antarctica: Background and previous works

The West Antarctic Rift System (WARS) is one of the world's distinct areas of continental extension, and compares in size to other major continental rift systems such as the Basin and Range, and the East African Rift System (EARS). Accurate plate reconstruction has proven difficult, given Antarctica's complex history, and the exact relations between volcanism, rifting, and the final breakup of West Antarctica with Gondwana are only partially understood [*Wilch and McIntosh*, 2000]. The continental breakup between Australia and Antarctica commenced at roughly 95 Ma, creating in its wake several microplate systems such as New Zealand, Marie Byrd Land and Tasmania, among others. The Ross Sea Basin is a resulting expression of this area of former microplates, and consists of sediment filled horst and graben structures. Most of the present day extension, though very small, is thought to be concentrated within the Terror

Rift, in the Ross Sea [*Salvini et al.,* 1997, *Lemasurier and Landis,* 1996]. The southern expression of the WARS abuts the Transantarctic Mountains (TAM), displaying prominent rift-shoulder uplift generated through episodic rifting of the WARS which begun at roughly 60 Ma. Fission track studies [*Behrendt and Cooper,* 1991, *Fitzgerald et al.,* 1992] have suggested that most of the TAM uplift was concentrated in bursts since mid-Pliocene times, with rates of up to 1 km/Ma, but this hypothesis has since been disputed [*Wilch et al.,* 1993], and rates are likely lower. The extent of the rifting is also thought to extend from the Ross Sea to beneath the West Antarctic Ice Sheet (WAIS) [*Behrendt and Cooper,* 1991], possibly even encompassing most of Marie Byrd Land. Most of the extension in the rift system is thought to be early to mid-Cenozoic following a prominent period of extension occurring during the breakup with New Zealand (100-83 Ma) [*Lemasurier and Landis,* 1996], although the geological dating of individual extension locals is obscured by the WAIS.

In terms of extensional rates, current rifting in the WARS, limited to the Terror Rift region, is estimated at $\sim$2 mm/year, which is generally slower than other intracontinental rifts such as the Rio Grande Rift, the Baikal Rift and the East African Rift, which come in at 0.5-5 mm/year, 4.5-6.5 mm/year and 3.7-6 mm/year respectively [*Brink and Taylor,* 2002, *McClusky,* 2010, *Sheehan et al.,* 1991]. Further comparison with other intracontinental rifts reveals an important distinction pertaining to crustal and mantle properties. Notably, the rift floor of the WARS is substantially lower (1-2 km) than other rift systems, with the Basin and Range and the EARS both displaying uplift instead of subsidence [*Cooper et al.,* 1987]. Another notable feature of the WARS is the presence of 4 impressively deep (multi-km) ice troughs, which, when isostatically corrected and compared with rift trough elevations in the East African rift would suggest a stable and cool interior of the WARS, [*LeMasurier,* 2008] as hot buoyant mantle should have caused substantially more uplift. Also resulting from trough studies is the observation that the Byrd Subglacial Basin and the Bentley Subglacial Trench (see Figure 0.1) have very little sediment deposits (i.e. $\sim$0.5 km) as compared to the Victoria Land Basin, despite their impressive depths [*Winberry,* 2004, *LeMasurier,* 2008]. This has lead to the inference of late Cenozoic (Neogene) extension located in these subglacial troughs, as any rifting episodes predating the onset of modern permanent glaciation, estimated at $\sim$25 Ma [*Hayes et al.,* 1975], would have rapidly accumulated large quantities of sediments, as observed for example at Lake Baikal, which hosts roughly 7 km of sediments [*LeMasurier,* 2008] despite late Cenozoic onset to rifting. This is however contradicted by magnetotelluric soundings in the Byrd Subglacial Basin, which propose the absence of melt in the upper 100 km, thus suggesting a cool mantle [*Wannamaker et al.,* 1996], and a dormant rift. Further supporting the idea of a largely dormant rifting system, surface wave tomography efforts [*Sieminski et al.,* 2003, *Ritzwoller et al.,* 2001] have noted that the upper mantle beneath the WAIS is faster than under the MBL and the Ross Sea, despite the very low resolution of the studies.

As a point of contention, aeromagnetic surveys [*Behrendt,* 1999] have reported finding large circular and linear magnetic anomalies throughout the WARS explained by the presence of volcanic edifices and large deposits of volcanic rocks, which, when combined with active source reflection studies [*Cooper et al.,* 1995] that offer possible evidence of volcanic intrusions into the youngest sedimentary layers filling the Victoria Land Basin, suggest young, widespread, possibly subglacial volcanism in the WARS. These studies note however that the extent of the hypothesized volcanism cannot be explained by Cenozoic extension, and thus assume a mantle plume or asthenospheric upwelling mechanism for instrusions.

Despite the hypothesized widespread subglacial volcanism and the curious lack of sediment in the subglacial troughs, the vast majority of evidence points to a relatively cool, largely dormant rift system, as evidenced by the currently estimated slow extension rate, the low elevation of the rift floor, the relatively normal upper mantle velocities, the evidence for a lack of melt in the upper 100 km under the WAIS, and the anomalously low seismicity recorded throughout West Antarctica [*Behrendt and Cooper,* 1991].

Crustal studies of the WARS have been sparse thus far, as geological studies have been largely hindered by the thick WAIS overlying most of the area. The ANUBIS and TAMSEIS projects are thus far the only major seismic initiatives that have produced estimates of crustal characteristics of West Antarctica. ANUBIS, (Antarctic Network of Unattended Broadband Seismometers) consisting of a scattered deployment of seismometers across the WAIS, was used to perform teleseismic receiver function analysis to gather estimates of crustal thicknesses across the WAIS and the southern flank of MBL [*Winberry,* 2004, *Anandakrishnan and Winberry,* 2004]. The results showed that the WAIS has crustal thicknesses decreasing from $\sim$34 km for the TAM, down to 25 km for the MBL flank, with localized thinning as low as $\sim$21 km under the Byrd Subglacial Basin [*Anandakrishnan and Winberry,* 2004]. It is notable that this initial look at a thin MBL crust contradicts most views of a much thicker crust compensated MBL [*Luyendyk et al.,* 2003]. The crustal thickness of the WARS is therefore comparable to the EARS with crustal thicknesses ranging from 20-34 km, but much thinner than other rifts, such as the Basin and Range, Baikal, and the Rio Grande Rift, all having average crustal thicknesses well above 30 km [*Wilson et al.*, 2005, *Brink and Taylor*, 2002, *McClusky*, 2010, *Sheehan et al.*, 1991].

The more recent TAMSEIS experiment, aimed at constraining crust and mantle characteristics beneath the WARS, TAM, and East Antarctic Craton (EAC) along a transect near Ross Island, showed that the low velocity anomaly beneath Ross Island extends 50-100 km inland into the EAC [*Wiens*, 2006]. Receiver function analysis of TAMSEIS [*Lawrence et al.*, 2006] data, alongside gravity and phase velocity studies, yielded crustal thicknesses of 40 km beneath the TAM (with a small $\sim$2 km crustal root), $\sim$20 km crustal thickness beneath Ross Island, and roughly 35 km thickness (stable) for the EAC. These results are corroborated by [*Bannister et al.*, 2003], who estimated a $\sim$20 km crustal thickness for the WARS near the TAM, moving up to $\sim$38 km in the TAM. Further efforts [*Bannister et al.*, 2000] also produced sparse shear wave velocity analysis of the Terror Rift area, and noted a low velocity anomaly of $\sim$6 percent with respect to the PREM model (Preliminary Reference Earth Model). Overall, crustal and mantle structure can thus far can be summarized as follows. Thick, stable crust under the EAC; thicker, but predominantly mantle compensated crust in the TAM; thin crust and low velocity mantle under Ross Island and near the WARS edge of the TAM; thin crust with normal mantle under the WAIS; somewhat thicker crust with abnormally hot buoyant mantle under the MBL.

One major component of the debate related to the evolution of the WARS is the history of the Marie Byrd Land volcanic province (MBL). The MBL currently consists of an uplifted and faulted basement of alkaline basaltic rocks, topped with 18 above-ice trachytic shield volcanoes. By tracking volcanism patterns, an uplift starting at 25-29 Ma has been suggested, continuing through to present time [*LeMasurier and Rex,* 1989], and the whole of MBL dome can perhaps be compared with Ethiopian domes in the East African rift. A mantle plume model for MBL is widely proposed, as basalts found there are similar to oceanic island basalts produced from other proposed mantle plumes [*LeMasurier and Rex,* 1989].

Currently, [*LeMasurier,* 2008, *Lemasurier and Landis,* 1996] have suggested that the evolution of the MBL can be explained through the tracking of a West Antarctic Erosion Surface, which manifests itself through exposed low relief basement nunataks with elevations ranging from 400-600 m on the coast to the 2700 m apex at Mt. Petras. Through noting that the volcanic ranges in the MBL are arranged NS-EW, and decrease in age away from the center of the dome, this model suggests that the migration of volcanism can be attributed to the extension of NS-EW faults through progressive dome uplift, accompanied by the release of magma through the resulting fractures. By tracking the low relief Cenozoic erosion surface, the MBL may be modeled as cycles of subsequent uplift/fracture/volcanism during extension. This model is simplistic however, and notable objections can be cited [*Wilch and McIntosh,* 2000]. An analysis of rocks at Mt Petras revealed that a previously noted low relief surface [*Lemasurier and Landis,* 1996] had in fact much more relief than previously thought, and therefore contradicted the idea of a simple flat Cenozoic pre-volcanic erosion surface. Moreover, this model support ample post-volcanic erosion during Cenozoic times. Detailed seismic studies of the MBL are required to better constrain the supposed mantle plume and other mantle structures.

The objective of this section was to develop a functional approach to deal with P-wave receiver functions (PRFs) in an Antarctic setting in the context of the POLENET project, and estimate crust and mantle properties for a widely distributed array of stations deployed over potentially complicated media. As the better part of the POLENET broadband stations are deployed over thick ice sheets, we are generally faced with extremely complex receiver functions where ice sheet multiples obscure conventionally interpreted conversions. This Chapter is largely based on a peer reviewed (or soon to be) first author publication focusing on the recovery of crustal parameters in West Antarctica.

Author Contributions

This body of work contains contributions from several people. Comparative tomographic images for the pseudo-reflection results in Chapter 2 were generated by Daria Zandomeneghi. Hunter Knox helped design the matched filter, which was used to pick the eruption database. Hunter Knox also assembled the Antelope database for the 2007-2009 dense deployment that was used to generate both the pseudo-reflection and tomography studies. Assembly of the Erebus Small Array data deployed during the 2011-2012 season, used in Chapter 1 to calculate eruption coda characteristics, was performed by IRIS PASSCAL employees and by NMT student Paige Czoski, who were as always instrumental in their field support and logistical handling of our data. Richard Aster wrote portions of the code associated with jointly inverting receiver function and surface wave crustal estimates in Chapter 4. The remaining research and coding were conducted by the author.

CHAPTER 1

CHARACTERISTICS OF CODA, AND EREBUS SMALL ARRAY

1.1 Introduction

The seismic coda is the long decaying tail of a seismogram which reaches noise levels after a given time length. Coda decay is controlled locally to regionally, and depends on the nature of the medium (i.e. scattering mean free path, composition, etc) and by the frequency of the wavefield, but not, within limits, by the distance from the source, or by the nature of the source and any of its source-time or radiation pattern characteristics [*Aki and Chouet,* 1975]. Early computational models had a certain degree of success explaining coda through a combination of single scattering and dissipation effects, though with the advent of more powerful computers, multiple scattering models seem more in line with signals generated in real media [*Margerin et al.,* 2000].

Naturally, given the density of information pertaining to Green's functions of the medium contained in the coda, there has recently been a great deal of interest in the possibility of extracting Green's functions and scattering information [*Snieder,* 2004, *Wapenaar,* 2006, *Campillo,* 2003] from an otherwise chaotic signal. In particular the recently developed theory of seismic interferometry (see Chapter 2 for derivation and implications) relies heavily on wavefield equipartition properties that are theoretically satisfied by multiply scattered coda under some sets of conditions. Modal equipartition, a condition under which the energy partitioning of seismic wavefields may be adequately described by a diffusion approximation [*Campillo*, 2003, *Hennino et al.*, 2001], has been the subject of much exploration, both theoretical and practical, and is thought by many to be the key to next-generation seismological methods.

Given the complexity of natural media, conventional methodologies tend to dismiss seismic coda as largely unusable for a number of structural studies, and focus on the deterministically modeled arrivals, or the first few converted or reflected arrivals that lend themselves well to simple interpretation. Seismological studies performed in highly scattering media have to deal with a very complex coda that simply cannot be interpreted via conventional approaches. In particular, volcanoes are perhaps the most ambitious of media to explore seismically in light of localized abrupt variations in physical parameters, extreme topography, the presence of large bodies of magma, and other fluids.

In this Chapter, an overview of the theoretical and practical components governing multiply scattered wavefields are discussed, and the characteristics of coda wavefields recorded on Erebus volcano are explored, in part to verify theoretically whether or not pseudo-reflection methods conducted through seismic interferometry may be applied, and in part to extract medium information and scattering parameters.

1.2 Radiative transfer, diffusion, and equipartition

Multiply scattered wavefields present a combination of regimes. The earliest part of the coda can be modeled through the Radiative Transfer Equation (RTE) where single scattering approximations are thought to be dominant. At longer time lapses the wavefield in a sufficiently scattering medium eventually settles into a diffusion regime, in which a stabilization of the P/S energy ratios may be observed via array radiometric measurements [*Margerin and Campillo*, 2009].

With few exceptions, there exist no analytical solutions to the RTE, so numerical simulations must be performed. [*Margerin et al.*, 2000] describes a Monte Carlo approach through which estimations of the P and S energy ratios for an arbitrarily scattering medium may be determined. There are currently works in progress to adapt this methodology for Erebus, but they are not sufficiently mature to be presented here. A brief overview of the Monte Carlo method is, however, described here along with results from previous studies on the matter (see [*Margerin et al.*, 2000] for full description). Figure 1.1 presents a conceptual description of the Monte Carlo approach to modeling the RTE for elastic waves.

For a given wave particle (i.e. a particle having P or S wave properties) and a chosen density of scatterers, the Monte Carlo algorithm chooses via random walk, for every scattering event, a scattering path length, a scattering direction in 3D space defined by the angles ϕ and $\cos\Theta$, and a scattered wave type defined as M_{sc}, based on probability statements defined by:

$$P(M_{inc}|M_{sc}, \cos\Theta, \Phi) = \frac{\frac{d\sigma}{d\Omega}(M_{inc}|M_{sc}, \cos\Theta, \Phi)}{\sum_{M_{inc}} \int_{4\pi}(M_{inc}|M_{sc}, \cos\Theta, \Phi) d\cos\Theta d\Phi} \tag{1.1}$$

where $d\Omega$ describes integration over a unit of solid angle, and $\frac{d\sigma}{d\Omega}$ represents the scattering cross-section, defined below. Correctly modeling this distribution necessitates reformulation as a set of conditional probabilities, as the core parameters

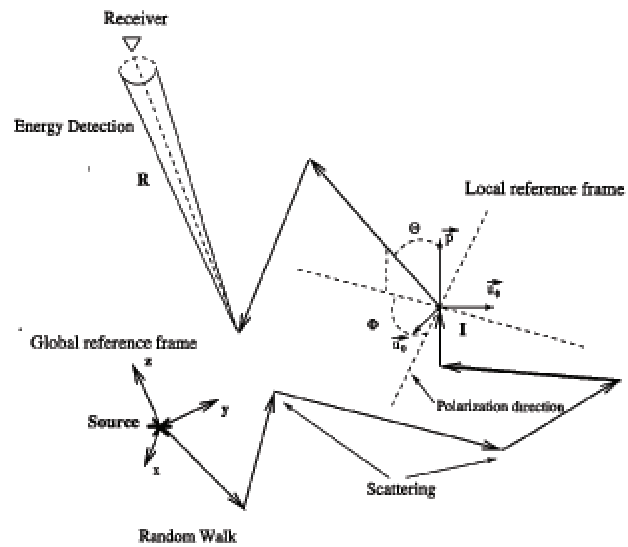

Figure 1.1: Conceptual depiction of a Monte Carlo solution to the RTE for elastic waves. A given wave particle of a given mode is propagated with parameters determined via random walk, until it scatters, gaining a new polarization, direction, and mode. At every scattering event, a local coordinate system is assigned according to the propagation direction and polarization of the particle, and the energy contribution is calculated at a receiver arbitrarily placed in the medium. The average over many propagated particles yields a numerical approximation to the RTE, allowing for estimates of equipartition stabilization times, and scattering characteristics of the medium. From [*Margerin et al.*, 2000]

ϕ, $\cos\Theta$ and M_{sc} are not independent. The partition in $P(M_{inc}|M_{sc}, \cos\Theta, \Phi)$ denotes a parameterization by the incident polarization, M_{inc}. The scattering path length probability distribution is much simpler to model, and is described as:

$$L = \frac{1}{l_{P,S}} \exp \frac{-L}{l_{P,S}} \tag{1.2}$$

where $l_{P,S}$ denotes the mean free scatter length based on the density of scatterers in the model. For the case of an infinite and statistically uniform scattering medium, a Stokes vector may be defined for a given wave particle traveling in it as

$$S = (I_p, I_{sv}, I_{sh}, U, V) \tag{1.3}$$

where I_p, I_{sv}, I_{sh} dictate intensities for compressional and shear waves, and U and V denote the cross-correlation relation between the shear components of the waves, and account for ellipticity and polarization plane, as defined in optics. Every scattering event as shown in Figure 1.1 redefines the Stokes vector , which accounts for the direction, polarization, and wave type of the newly scattered wave. Furthermore, at every scattering event, the energy contribution at an arbitrarily placed receiver in the medium is calculated for both P and S modes:

$$E_{M_{sc}} = \frac{P(M_{inc}|M_{sc}, \cos Theta, \Phi) exp(\frac{-R_{sd}}{l_{M_{sc}}})}{R^2 v_{M_{sc}} dt} \tag{1.4}$$

where R_{sd} is the scatter-receiver distance and $v_{M_{sc}}$ is the velocity of the energy contributing mode M_{sc}. All energy contributions are stored in a vector, and a model space of many random walks is created to estimate total energy ratios of the system in time. The nature of the scattering is however an area that presents some exploration possibilities. Typically, the scattering kernel is approximated by assuming scattering from spherical inclusions [*Sato et al.*, 1997], and we define the scattering cross sections from equation 1.1 as :

$$\frac{d\sigma_{PP}}{d\Omega} = \frac{k_P^4}{16\pi^2}\gamma_1^2(\Theta) f_{PP}^2(\Theta) \tag{1.5}$$
$$\frac{d\sigma_{PS}}{d\Omega} = \frac{k_S^4\beta}{16\pi^2\alpha}\gamma_2^2(\Theta) f_{PS}^2(\Theta) \tag{1.6}$$
$$\frac{d\sigma_{SP}}{d\Omega} = \frac{k_S^4\alpha}{16\pi^2\beta}\gamma_3^2(\Theta) f_{SP}^2(\Theta)\cos^2\Phi \tag{1.7}$$
$$\frac{d\sigma_{SS}}{d\Omega} = \frac{k_S^4}{16\pi^2}\gamma_4^2(\Theta)(f_{SS_l}^2(\Theta)\cos^2\Phi + f_{SS_r}^2(\Theta)\sin^2\Phi) \tag{1.8}$$

Here, the γ_x correspond to additional mode specific scattering terms that may be found in [*Margerin et al.*, 2000]. Intuitively, the scattering cross-sections contain all the information about the angular dependance of the scattered flux, and are described as the ratio of the energy scattered in the space direction Φ, Θ per unit time and per unit solid angle by the spherical inclusion, to the energy per unit area and unit time of the incident wave. Most importantly, the size of the spherical inclusion with respect to the central wavelength of the incident wave plays an important role in dictating the dominant directions (i.e. forward to backscattered) of scattered energy. A simple case often used in optics and electromagnetics assumes that the size of the dimensions of the scatterers are much smaller than the wavelength of the incident waves. This is known as Rayleigh scattering, and leads to greatly simplified descriptions of the scattering cross-sections, where $\gamma_x = 1$. Practically, and particularly in volcanic settings where bodies of magma on the order of hundreds of meters to several kilometers may exist, this assumption is likely invalid. As such, it is necessary to adopt a scattering kernel representative of spherical scattering from inclusions roughly of the same scale as the wavelength, so-called Rayleigh-Gans scattering. In such a case, each spherical inclusion becomes an integrated set of point scatterers distributed over a given volume. For further information on spherical scattering, refer to [*Aki and Chouet,* 1975]. Figure 1.2, taken from [*Margerin et al.,* 2000], displays a series of Monte Carlo simulations depicting the eventual stabilization of P and S energy ratios in time, where the wavefield is thought to present a diffusive character, and to reflect modal equipartition [*Campillo,* 2003].

From diffusion, the seismic equipartition ratio for any medium can be expressed as:

$$\lim_{t \to \infty} \frac{\langle E_S \rangle}{\langle E_P \rangle} = \frac{2\alpha^3}{\beta^2} \tag{1.9}$$

where α and β denote P and S wave velocities, and the brackets denote an average over the configuration of scatterers. Note that the ratio at which equipartition is observed is independent of the nature of the scatterers, and will only be sensitive to the Poisson's ratio of the medium (according to a diffusion approximation). The theoretical equipartition ratio $\frac{E_S}{E_P}$ as predicted by both diffusion and RTE for a Poisson solid is $\sim$7.2, for a bounded homogenous half-space with a uniform scatterer distribution. Should the medium display comparatively low S-wave velocities, as caused by the presence of molten rock, then in theory this ratio should increase. The interest of modeling the multiply scattered wavefield in this manner lies in the potential comparisons that can be made with the time scale relating to the stabilization of the E_S/E_P energy ratio, as well as the value of the ratio itself, which may yield information about the nature of the medium. Works by [*Hennino et al.,* 2001] have highlighted the importance of developing an

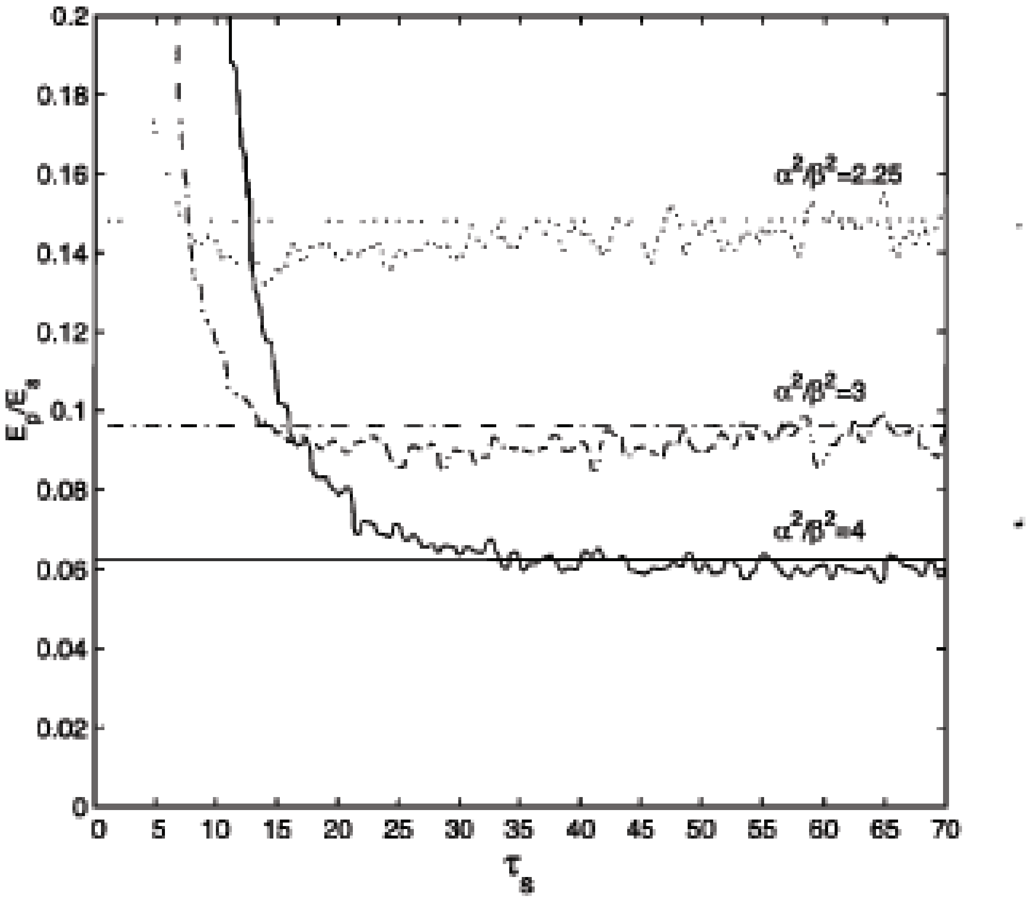

Figure 1.2: Examples of Monte Carlo solutions to the RTE for various ratios of V_p^2/V_s^2 for purely Rayleigh scattering, depicting E_P/E_S ratios in time for a source-station distance of two P mean free paths. The horizontal lines denote the theoretical equipartition ratio as computed via diffusion, and τ_s represents the mean free scatter time. Several factors may affect convergence time to equipartition, such as distance from the source, Poisson's ratio of the medium, and scatterer density. From [*Margerin et al.,* 2000]

approach to estimate equipartition in real media. For a given wavefield, the total elastic wave energy density can be described as [*Hennino et al.,* 2001]:

$$W = \frac{\rho}{2}(\partial_t \mathbf{u})^2 + (\frac{\lambda}{2} + \mu)(\nabla \cdot \mathbf{u})^2 + \frac{\mu}{2}(\nabla \times \mathbf{u})^2 + I \tag{1.10}$$

The terms in the above equation represent kinetic (K), compressional (P), and shear (S) energy densities, while the last term (I) involves cross-terms with vanishing averages except at boundaries. Practically, it is fairly simple to deploy a small array capable of estimating the horizontal derivatives of a given medium. The vertical derivatives may further be calculated by imposing the stress-free condition at the surface:

$$\lambda(\nabla \cdot \mathbf{u})\delta_{iz} + \mu(\partial_i u_z + \partial_z u_i) = 0, \tag{1.11}$$

where $i = x, y, z$. Several studies have been performed using extremely dense arrays of stations to estimate equipartition ratios in real situations. The first study of this kind [*Hennino et al.,* 2001] consisted of a small square array in Mexico, and an equipartition ratio very close to the diffusion derived ratio for a Poisson half-space was observed in the coda of a series of local earthquakes. However, subsequent studies [*Margerin and Campillo,* 2009] at the Pinon Flat observatory have noted, for local earthquakes, a consistent equipartition ratio of $\sim$2.5, a factor of almost 3 smaller than predicted by diffusion, though the frequency range of the data used was extremely limited. Consequently, it has been proposed that other effects rather than variations in the Poisson's ratio may affect the inferred equipartition ratio. Most importantly, the study at Pinon Flat was able to determine that stability ratios can vary drastically with frequency as a consequence of the local medium, and that effects such as resonance in individual layers may play a large role in the ultimately resolved ratios. A theory of equipartition for layered media and unlocked modes (i.e. transitions from body, Love, and Rayleigh modes is permitted) was developed, and the multiply scattered wavefield was modeled via finite difference. Figure 1.3, taken from [*Margerin and Campillo,* 2009] demonstrates the results of a simple 2-layer model as compared with the frequency dependent equipartition ratios for the Pinon Flat observatory area.

Of particular interest is the relation between the variations in the ratios and the parameters of the layers in the medium. As studies by [*Yamamoto,* 2010] on Asama volcano, Japan, have also noted deviations from simple diffusion derived equipartition ratios, such a theoretical framework could help constrain the scale of resonant features in more complicated media as well.

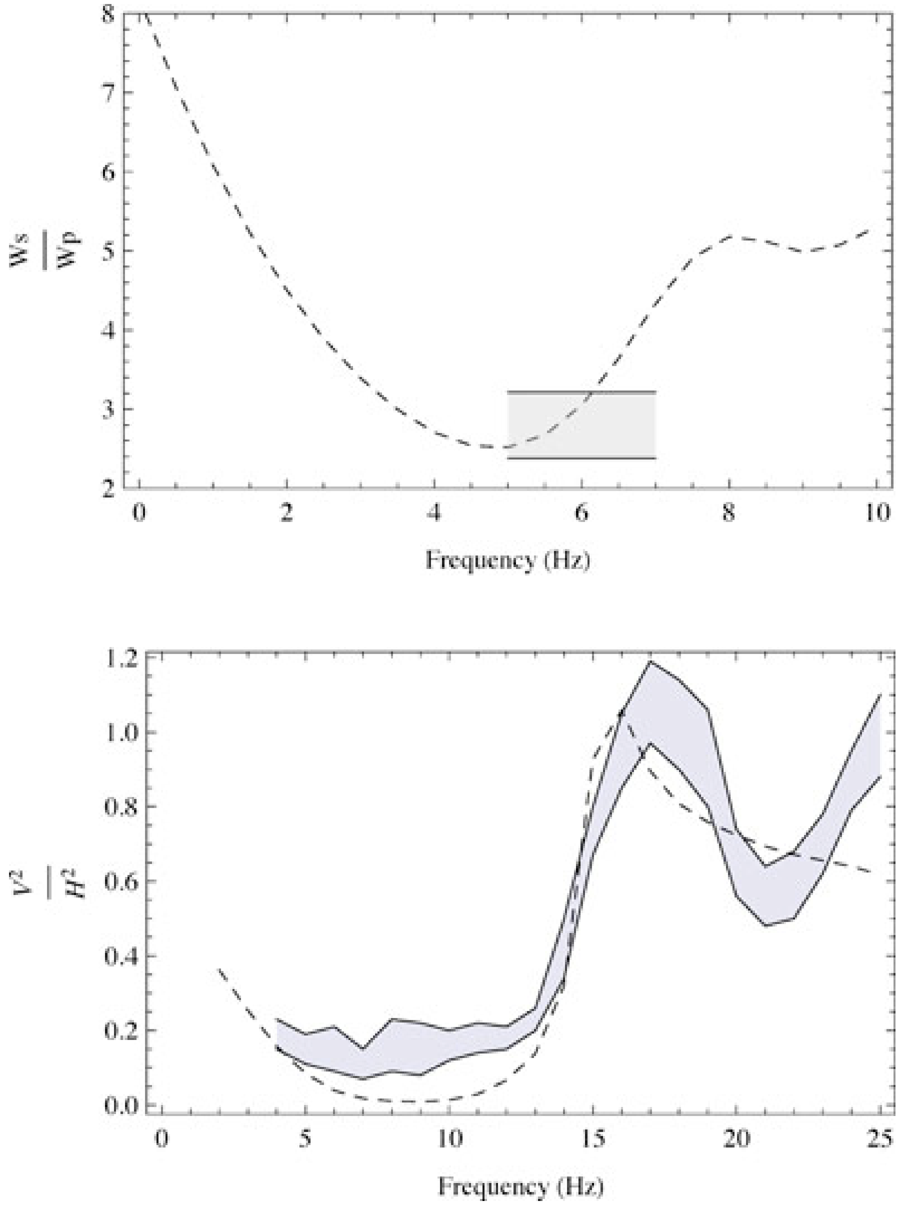

Figure 1.3: S/P and V^2/H^2 (vertical energy over horizontal energy) ratios for a simple 2 layer model, as compared with data from the Pinon Flat Observatory. Resonance effects in the shallow weathered granite layers cause substantial frequency dependence of the equipartition ratio as well as vertical to horizontal energies, which is not predicted by homogeneous half space scattering models based on RTE or diffusion. Note that only a very small frequency range of equipartition ratios was observed (top panel, grey box) due to data and instrument limitations. The entire shape of the frequency dependence in terms of equipartition remains, to a degree, speculative. From [*Margerin and Campillo,* 2009].

1.3 Transient equipartition at Erebus volcano: Erebus Small Array

As mentioned previously, the equipartition ratio as defined by diffusion does not theoretically depend on the nature of the scatterers for simple models, but resonance effects can occur causing frequency dependence of the ratio. The time scale necessary for modal stability to occur, however, will be highly influenced by the mean free scattering length, and thus the density of scatterers. Works by [*Yamamoto,* 2010, *Sato et al.,* 1997, *Margerin et al.,* 2000] have noted, via finite-difference and Monte Carlo simulations, that equipartition may occur in as little as a few scattering time constants. As such, the more highly scattering the medium, the faster modal equilibrium should be reached. It has therefore been suggested that pseudo-reflection methodologies based on seismic interferometry (see Chapter 2) may be particularly applicable in volcanic media, which tend to be extremely scattering [*Yamamoto,* 2010] has estimated the mean free path at Asama volcano to be under 1 km, in contrast with the roughly 20-40 km free path of continental crust at a frequency of $\sim$1 Hz [*Hennino et al.,* 2001]. Volcanoes may also feature a variety of usable local high frequency sources from eruptions or volcano-tectonic events.

The Erebus Small Array (ESA) consisted of a very dense array of 5 Guralp CMG 40T seismometers set in a square with a fifth station positioned centrally, and was deployed during the 2011-2012 Antarctic field season for a period of 5 weeks. The goal of this small-scale study was to record local transient seismic signals, of eruptive or glacial nature, to assess the character of the multiply scattered wavefield for Erebus volcano. Figure 1.4a displays a map of ESA, deployed near MEVO station LEH on an unusually well consolidated lava flow, thus guaranteeing ideal station coupling and limiting errors in the subsequent spatial derivatives. Erebus volcano has produced a variety of relatively young lava flows on its upper plateau with ages ranging from 9-80 ka [*Kelly et al.,* 2008]. ESA is located squarely on an exposed portion of a spatially extensive $\sim$11 ka lava flow spanning a broad region encompassing MEVO station LEH. The local thickness of this lava flow is unknown, but given its relatively small size, it likely ranges from a few meters to a few tens of meters at most. The lengths of the ESA square are $\sim$ 50.6 and 49.8 m for the ESA1-4 and ESA3-4 sides respectively, with total elevation discrepancies limited to $\sim$7 meters. The stations were deployed for $\sim$2 months, though two stations eventually developed problems, resulting in 3 weeks of usable data. The presence of a relatively thin discrete layer in the form of a lava flow directly underlying the array further presents an interesting opportunity to confirm hypothesized observations at Pinon Flat [*Margerin and Campillo,* 2009]. As shown in Figure 1.3, studies at Pinon Flat were unable to fully sample the spectrum of equipartition due to instrument and data limitations, and therefore the theoretical frequency dependence of equipartition ratios described in their experiments, where shallow structural layering could impact ratios substantially, remained for the most part untested. The peak frequency range of Erebus volcano transients, of eruptive or icequake nature, is typically 1-8 Hz, thus allowing us to extend the theoretical base developed by [*Margerin and Campillo,* 2009] to a testable scenario spanning that range.

Figure 1.4b shows an example of a 55 hour seismic record at station ESA1 showing a variety of transients, mostly icequake related. The largest 20 events were manually picked from the 5 week period, and the analysis detailed by equations 1.10-1.11 was performed. As the primary short period frequency content for both

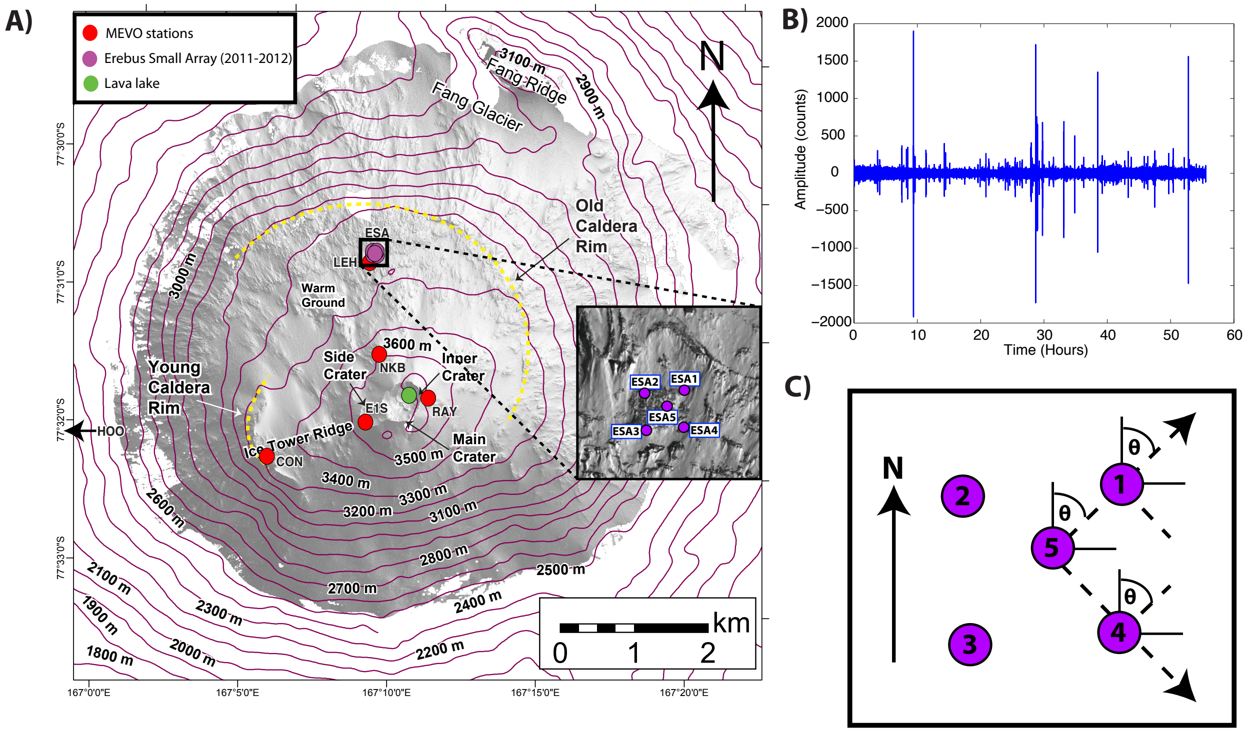

Figure 1.4: Erebus small array. A) Map of the upper edifice of Erebus volcano with detailed geological features and locations of the ESA array (inset) and the permanent MEVO array for reference. B) ∼55 hours of continuously recorded data on station ESA1, featuring several transient short period signals, mostly icequake related. C) Illustration of coordinate rotation for individual station sets. All station were oriented due North, so for every set of stations presenting a spatial set of perpendicular axes, we rotated the station coordinate systems so that N and E directions were parallel with inter-station azimuths. θ represents the rotation angle.

icequakes and eruptions falls between 1-8 Hz [*Knox*, 2012], we filtered the data accordingly to isolate the short period signature.

Figure 1.5 presents the results of energy density ratios calculated for a small lava lake Strombolian eruption recorded at ESA. To estimate horizontal spatial derivatives, a high degree of inter-station coherency must be observed. [*Margerin and Campillo*, 2009] showed that for Pinon Flat, interstation derivatives typically stabilize between 50-150 m distances, though Erebus is likely far more scattering a medium.

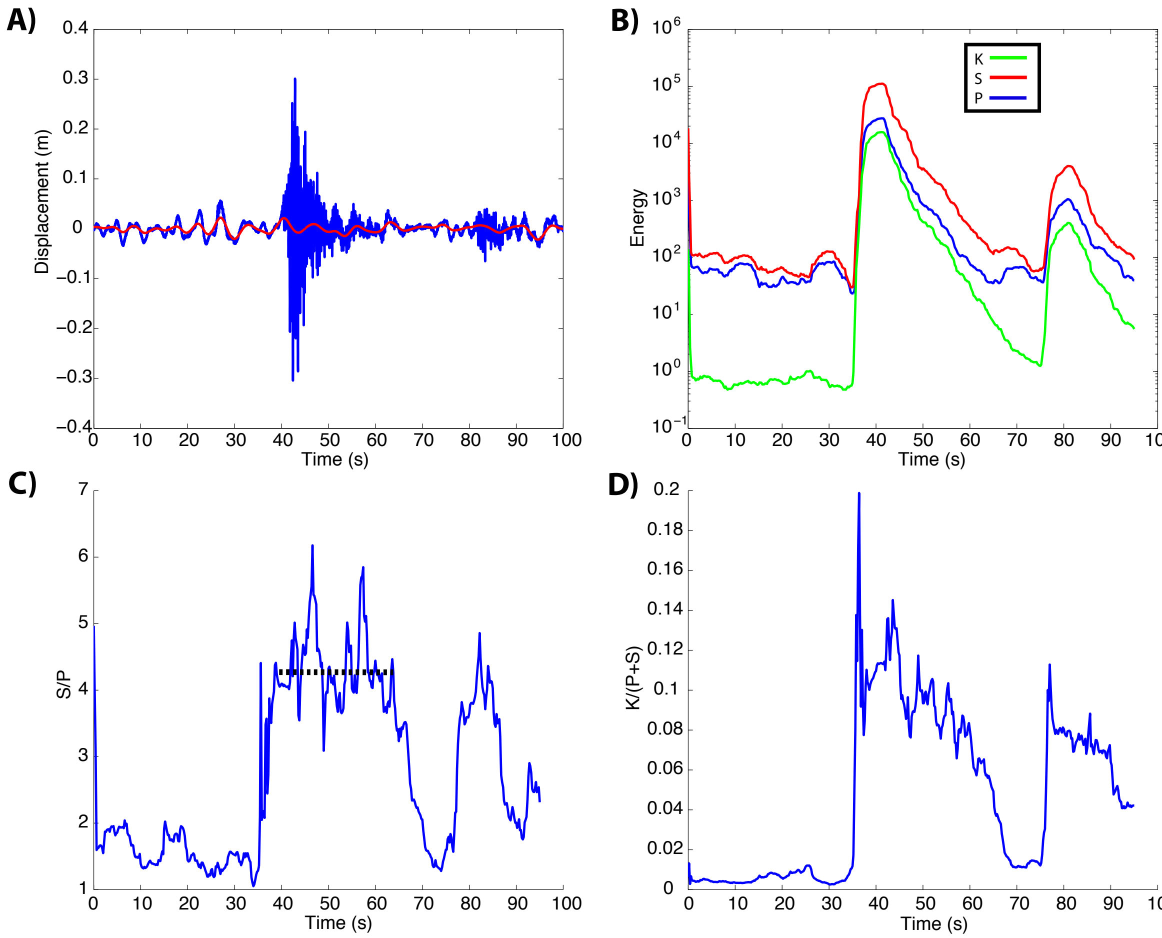

Figure 1.5: Equipartition calculations for Erebus volcano. A) Small double eruption of the lava lake as recorded on ESA1. B) P, S, K calculations plotting on a logarithmic scale for the event depicted in panel A, smoothed by a 5 second moving window. C) Average ratio S/P for the frequency band 1.5-6 Hz. The stability ratio is denoted by a dashed black line. This ratio is frequency dependent, though only an average is given here. D) $K/(P+S)$ ratio. This ratio has been suggested as a more stable proxy for measuring equipartition, though it is perhaps less intuitive. Here, P, S, K refer to the quantities defined in equation 1.10.

For each combination of independent axes at ESA (for example, ESA1, ESA5, ESA4, see Figure 1.4c), the coordinate systems at each station were rotated into to a local system (figure 1.4c) so as to permit derivatives along the X and Y directions. Figure 1.5a depicts a small double eruption [*Rowe et al.*, 1998] recorded at ESA1. Figure 1.5b shows the variations in K, P, and S energies for a period covering the pre-eruptive noise to the complete decay of the coda. Figure 1.5c shows the results of S/P ratios over time, showing a clear stabilization ratio of the shear and compressional energies, indicative of modal equipartition. Theoretically [*Hennino et al.*, 2001, *Margerin and Campillo*, 2009], there should also be a stabilization of the horizontal versus vertical energies, which can be calculated easily at single stations. The ratio $K/(P+S)$ has also been identified as worthwhile in the identification of modal equipartition [*Hennino et al.*, 2001]. Figure 1.5c-d depicts these two ratios for this event on Erebus. Figure 1.6 shows the frequency dependance of equipartition ratios for a multitude of events, all showing very similar frequency dependent stabilization ratios, which could point to potential resonance effects as identified by [*Margerin and Campillo*, 2009].

Thus far, theoretical equipartition relations were only derived for horizontally stratified media, and not for arbitrary structures. Directly relating the variations in equipartition ratios to complex structure could be computationally expensive, and has not yet been attempted. Ratios at Erebus, for the 1-4 Hz region, are however much lower than those observed in Poisson half space, suggesting that significant structural resonance may be occurring on scales from several tens to several hundreds of meters. It has been noted also that the equipartition ratio is highly sensitive to the parameters of the first layer [*Margerin and Campillo*, 2009], even when this layer has a thickness of as little as tens of meters. For Erebus, such a layer, composed of lava flows, is very probable, and thus offers a hypothetical explanation for the ratios observed at ESA.

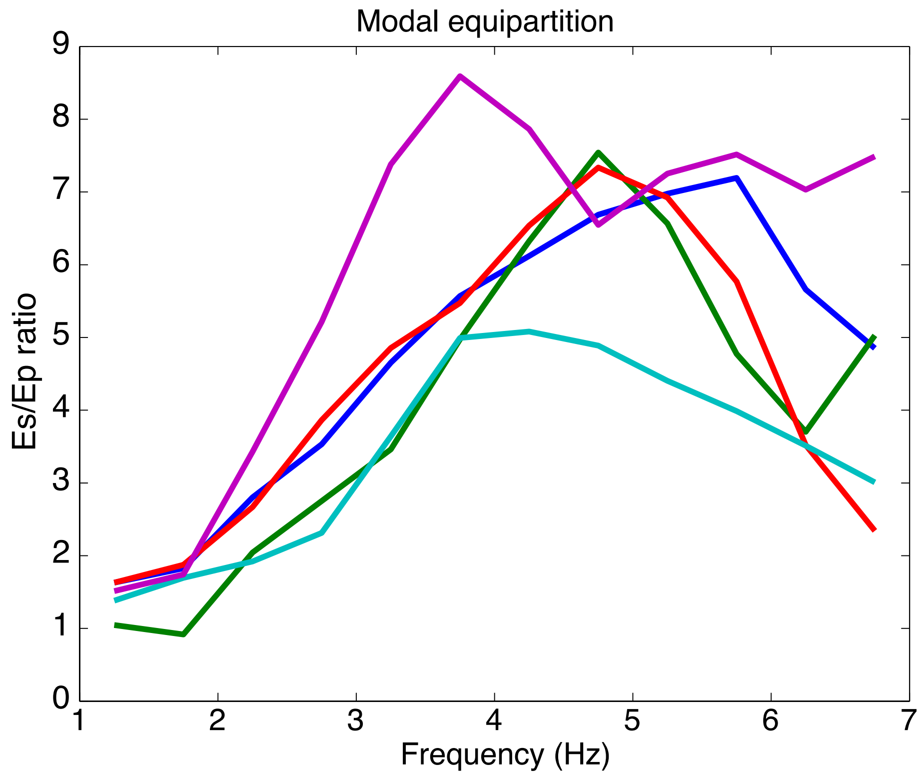

Figure 1.6: Frequency dependent equipartition ratio for 5 events recorded on ESA. The substantial dip in the ratio away from the diffusion predicted ratio is likely due to resonance effect from shallow structures on the order of several tens to hundreds of meters.

1.4 Conclusions

Future steps in this research will be to perform Monte Carlo simulations as described above, to estimate the scattering mean free path for Erebus, with an eventual goal of generating finite-difference based estimates of coda signatures for Erebus volcano. Given the complexity of the Erebus volcanic edifice however, a finite difference model capable of producing the type of coda observed for Strombolian eruptions may require significant computational resources. Furthermore, V^2/H^2 ratios, which can be computed at single stations, may yield additional information pertaining to the structural composition of the Erebus upper plateau. ESA has served the purpose of yielding a positive proof of wavefield equipartition for local transient seismic signatures at Erebus, which satisfies the theoretical requirements for applications of seismic interferometry.

For future updates on this study, refer to the manuscript: ”Wavefield equipartition at Erebus volcano: Implications for pseudo-reflection imaging”.

CHAPTER 2

3D PSEUDO-REFLECTION OF MT EREBUS VIA BODY WAVE SEISMIC INTERFEROMETRY OF STROMBOLIAN ERUPTION CODA

2.1 Introduction

Accurate recovery of a medium's Green's function, or impulse response, is typically viewed as the holy grail of seismology as it yields information concerning the location of discrete structural transitions as well as the composition of said structures. Conventionally, recovery of the impulse response of a medium for a given source-station geometry is conducted directly, by setting off a nearly impulsive anthropogenic source and interpreting the reflected arrivals. Though informative, this approach does not lend itself easily to experiments outside tightly controlled industrial ventures, as deploying large reflection seismology experiments can be prohibitively expensive, as well as highly limited in terms of the recovery of temporal information. Furthermore, in highly heterogeneous media such volcanoes, large scale reflection experiments often fail, as complex shallow layering with a high degree of lateral variability contaminate interpretable arrivals. Passive recovery of a medium's Green's function where impulsive sources are not available remains therefore a subject of great interest. As mentioned briefly in the previous Chapter, one of the most interesting consequences of modal equipartition is the possibility it presents concerning the recovery of a medium's impulse response. There has been a great deal of recent interest concerning the extraction of meaningful information from otherwise chaotic, noisy signals, and with the recent advent of seismic interferometry, recovering the Green's function passively in a wide variety of media is becoming far more approachable.

2.2 Theoretical background

The theory of seismic interferometry fundamentally states that the Green's function of a medium between two seismic stations can theoretically be approximately recovered if the medium of interest is surrounded by dense, irregularly, spaced sources of either impulsive or continuous character, or if the wavefield demonstrates modal equipartition. Demonstration of the proportionality of the Green's function with the correlation of noise signals has been made evident through a variety of approaches. [*Weaver and Lobkis,* 2004] demonstrated the proportionality between Green's function and correlation for acoustic waves using a modal approach based on a discrete source distribution. This result was later generalized to include the case where a medium is illuminated by a diffuse equipartitioned wavefield generated by a single source in a scattering medium [*Van Tiggelen,* 2003, *Weaver and Lobkis,* 2004, *Wapenaar et al.,* 2004] derives this relation using representation theorems, and does not assume equipartition, but rather a continuous distribution of uncorrelated white noise sources surrounding the medium of interest. They also go on to point out that for this particular scenario, that erroneous contributions from scatterers outside the source distribution may be cancelled if the source distribution is sufficiently spatially incoherent. The recovery of the medium's Green's function this way is demonstrated by [*Van Manen et al.,* 2006] through numerical experiments. [*Snieder,* 2004] further notes that for a discrete source distribution, the spatially integrated cross-correlation of individual source responses between the surface stations will yield the Green's function, though the only retained contributions will be from stationary areas of the spatially averaging integrand. Furthermore, they concluded that equipartition was not a prohibitively necessary condition for the recovery of the Green's function. Here, we present an simple 2D scalar argument taken from derivations by [*Sanchez-Sesma and Campillo*, 2006], which demonstrate the recovery of the Green's function if the wavefield is diffuse. Assuming we have only SH waves propagating in a homogeneous elastic medium, where propagation occurs only in the $1-3$ plane, the displacements in the antiplane satisfy the wave equation:

$$\frac{\partial^2 v}{\partial x_1^2} + \frac{\partial^2 v}{\partial x_3^2} = \frac{1}{\beta^2}\frac{\partial^2 v}{\partial t^2} \tag{2.1}$$

where β is the shear velocity. Solving this equation yields the expression for a plane wave:

$$v(\mathbf{x}, \omega, t) = F(\omega, \psi) exp(-\imath k x_j n_j) exp(\imath \omega t) \tag{2.2}$$

where $k = \frac{\omega}{\beta}$ is the SH wavenumber, ω the angular frequency, and n_j are propagation direction cosines, where$n_1 = \cos\psi, n_3 = \sin\psi$. We may now consider the correlation of equation 2.2 at location x and y, where we assume y is at the origin for simplicity. As such, $n_j x_j = r n_j \gamma_j = r\cos[\psi - \theta]$. Also for the sake of conciseness, we omit the time factor $exp(\imath\omega t)$ from future expressions. We therefore have:

$$v(\mathbf{y}, \omega) v^*(\mathbf{x}, \omega) = F(\omega, \psi) F^*(\omega, \psi) exp(\imath k r \cos[\psi - \theta]) \tag{2.3}$$

Here we make an important assumption. If the wavefield is isotropic with waves propagating in directions given by ψ, and that the average spectral density of the field is roughly independent of ψ, then we define the average spectral density as $F(\omega, \psi)F^*(\omega, \psi) = |F(\omega)|^2$. As such, and azimuthal average of the correlation over ψ yields:

$$\langle v(\mathbf{y}, \omega) v^*(\mathbf{x}, \omega) \rangle = |F(\omega)|^2 \frac{1}{2\pi} \int_0^{2\pi} \exp(\imath kr \cos[\psi - \theta]]) d\psi = |F(\omega)|^2 J_0(kr) \tag{2.4}$$

where $J_0(kr)$ is the zeroth order Bessel function of the first kind. Equation 2.4 was first derived by [*Aki*, 1957] in a study on microtremors. We now consider the theoretical description of the Green's function in the frequency domain for our scenario, where $G_{ij} = 0$ everywhere except $i = j = 2$.

$$G_{22}(\mathbf{x}, \mathbf{y}, \omega) = \frac{1}{4} \imath \mu [J_0(kr) - \imath Y_0(kr)] \tag{2.5}$$

where $Y_0(kr)$ is the Neumann function of zeroth order and μ the shear modulus. By comparing equations 4 and 5, we may note that the correlation is proportional to the imaginary part of the Green's function. By setting $E_{SH} = \rho\omega^2 |F(\omega)|^2 /2$, the energy density for SH waves:

$$\langle v(\mathbf{y}, \omega) v^*(\mathbf{x}, \omega) \rangle = \frac{2}{\rho\omega^2} E_{SH} J_0(kr) = \frac{-8E_{SH}}{k^2} Im[G_{22}(\mathbf{x}, \mathbf{y}, \omega)] \tag{2.6}$$

Here Im is the imaginary part. It is important to note that $J_0(kr)$ contains all the information about the Green's function. See [*Aki and Richards*, 1980] for a description of Green's function properties. to recover the causal portion of the Green's function in the time domain, we merely need to perform an inverse Fourier transform of this result. This result may also be generalized for the 3D elastodynamic case, where P, SV and SH polarizations are permitted in the medium. However, in the generalization, unlike the exclusive SH case, a broader assumption on the averaged properties of the wavefield must be made to recover the true Green's function. When defining the spectral densities in the correlation function (e.g. $P^2 = |P(\omega)|^2, S_V^2 = |S_V(\omega)|^2, S_H^2 = |S_H(\omega)|^2$) as not having dependence on the propagation angles (in 3D now), it is also necessary for $P^2\alpha^3 = S_H^2\beta^3 = S_V^2\beta^3$ to hold if the true Green's function is to be recovered. In this case:

$$\langle v(\mathbf{y},\omega)v^*(\mathbf{x},\omega)\rangle = -2\pi\frac{\rho\omega^2(S_V^2+S_H^2)}{k^3} Im[G_{ij}(\mathbf{x},\mathbf{y},\omega)] \tag{2.7}$$

Applying the inverse Fourier transform to this result yields a simple, practically applicable result stating that the Green's function between any two points $(\mathbf{x},\mathbf{y})$ in a medium permeated by an equipartitioned wavefield may be recovered by cross-correlating the wavefield at those two points. For a simply applicable form, we use the form derived by [*Wapenaar et al.*, 2004] in the time domain:

$$2\Re[G_{p,q}^{\nu,f}(\mathbf{x},\mathbf{y},\omega)] \approx \frac{2}{\rho c_p}\left\langle v_p^{obs^*}(\mathbf{x},\omega)v_q^{obs}(\mathbf{y},\omega)\right\rangle \tag{2.8}$$

where $\Re$ denotes the real part, $G_{p,q}^{\nu,f}(\mathbf{x},\mathbf{y},\omega)$ denotes the Green's function between surface points $\mathbf{x}$ and $\mathbf{x}$, (ν, f) are the characteristics of the observed and source quantities (velocity and force), (p,q) are the components of the observed and source quantities, n_i is the vector normal to the integration surface ∂V, ρ is the density, $v_{p,q}^{obs}$ represents velocity seismograms of component p, or q at locations $\mathbf{x}$ or $\mathbf{y}$, and c_p is the P wave velocity.

Practical demonstrations of this concept, particularly concerning the recovery of surface waves via cross-correlation of ambient noise [*Campillo,* 2003], have garnered much success over the last decade in both continental scale imaging [*Shapiro et al.,* 2005, *Zheng et al.,* 2008] and on much smaller local scales. Volcanoes in particular have been testing grounds for pushing the limits of ambient noise tomography methods [*Brenguier et al.,* 2007, *Haney et al.,* 2011, *Shuler et al.,* 2008], given the small spatial scale but potential large amplitude of velocity anomalies of interest. Useful demonstrations of body wave applications remain few outside multiple laboratory experiments [*Tonegawa et al.,* 2009, *Tonegawa,* 2010, *Roux et al.,* 2005, *Chaput et al.,* 2012, *Draganov,* 2009], mainly due to the difficulty of identifying passive, persistent high-frequency body wave sources within the vicinity of a dense array overlying a sufficiently scattering medium.

2.3 Pseudo-reflection imaging of Erebus' magmatic system

Erebus volcano consists of a perfect natural laboratory for conducting a pseudo-reflection based on the recovery of body waves from seismic interferometry, given the persistent eruptive activity, the dense deployment of 2007-2009, and the inherent extreme scattering of the volcanic edifice. As noted in Chapter 1, the impulsive nature of the seismic source coupled with the extreme scattering of the Erebus volcanic edifice rapidly generates an equipartitioned coda which may be cross-correlated to recover the Green's functions between station. Given the difficulty in interpreting inter-station body wave reflections on highly complex non-horizontally layered media, we choose here to compute single station Green's function estimates, which lend themselves better to structural interpretation, as will be described below.

Here, we utilize optimally rotated six (three auto-component and three cross-component) correlations of Strombolian eruption coda at individual seismic stations to image strong seismic impedance (density time velocity) contrasts, such as will exist between magma and host rock, or between buried lava flows or intrusions and lower seismic velocity bomb, ash, or clast deposits. Features presenting a quasi-specular face to a given station, thus generating a high energy bidirectional raypath set with stationary phase, will be especially well-imaged with this technique. The following sections will be expansions of [*Chaput et al.,* 2012].

2.3.1 Eruptive character and pseudo-reflection model of Erebus edifice

Here we briefly describe the character of Strombolian eruptions on Erebus volcano, and give a practical description of the methodology used to recover the scattering image of Erebus. Strombolian eruptions on Erebus have the distinction of featuring both Short Period (SP) and Very Long Period (VLP) signals, as mentioned in the introduction. Figure 2.1 shows a typical Strombolian recorded at 5 permanent MEVO stations.

We may note distinct peaks in the VLP signal, and a swath of energy between 1-8 Hz, typical of the short period signal. A large database of eruptions was automatically built through the use of a correlation-based multi-station matched filter, which systematically searches through archived data for signals corresponding to a specific moveout template. Eruptions are typically easy to identify in this manner due to bubble burst being constrained to the lake. Figure 2.2 shows a histogram of event detection with matched filter up time.

Note that this eruption history estimate is compromised by seasonal outages because the predominantly solar-powered MEVO stations commonly lose

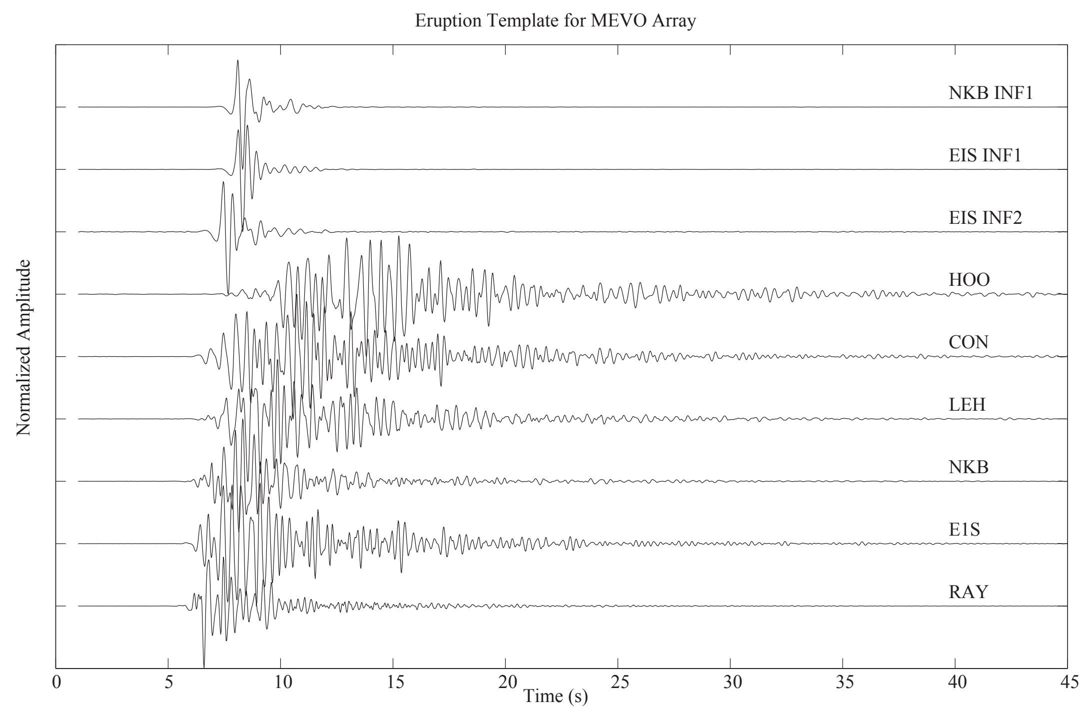

Figure 2.1: Eruption template recorded on the MEVO permanent broadband and infrasound array. This template was used to implement a matched filter eruption picking algorithm.

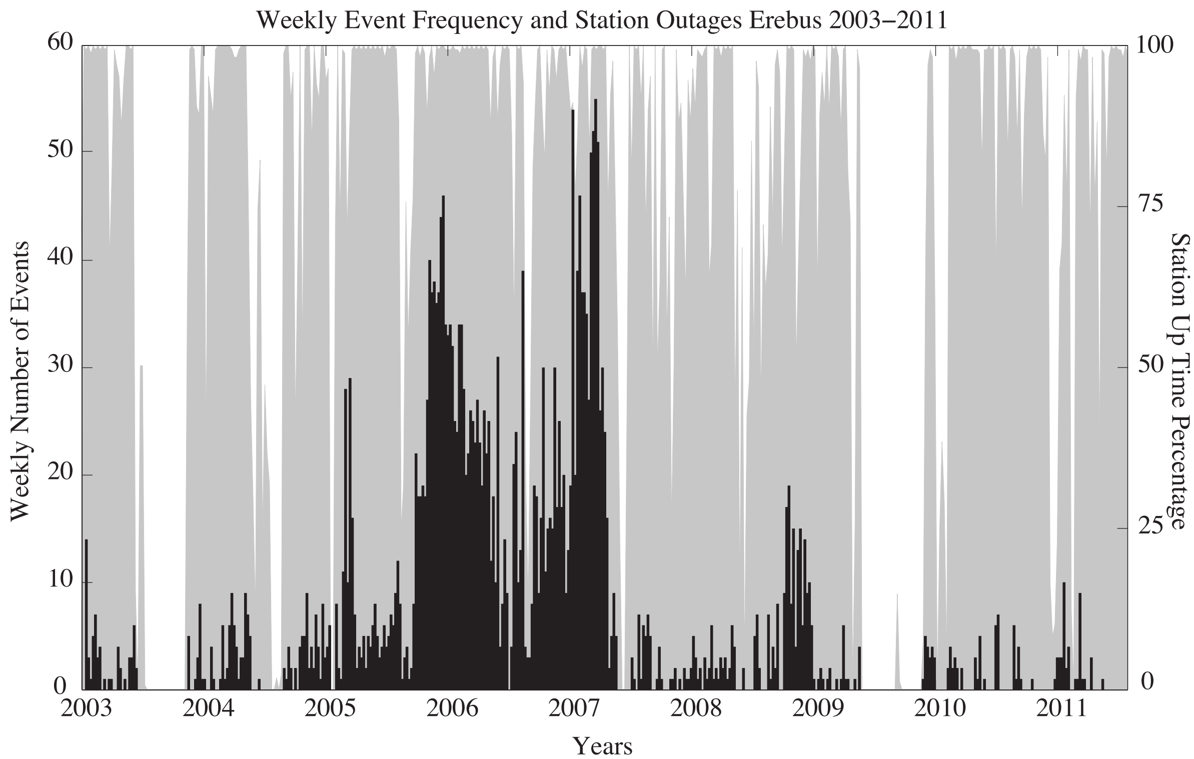

Figure 2.2: Left axis: Histogram of eruption frequency as detected by the matched filter. Right axis: Matched filter up time. The detection process requires a minimum of 3 stations, and stations typically lose power over the course of the dark austral winter. From [*Knox*, 2012].

power for a time during the dark Antarctic winter. Over 2400 eruptions spanning 2003-2008 were automatically identified using a multi-station matched filter and a characteristic eruption lag template for the Mount Erebus Volcano Observatory (MEVO) network. For a complete description of SP, VLP, database building efforts, and icequake documentation, please refer to [*Knox,* 2012].

Figure 2.3 shows a digital elevation model of Ross Island and the locations of the 92 three-component seismic stations used in this study. The persistent lava lake lies approximately 250 m below the crater rim summit. For the dense deployment of 2007-2009, the number of events recorded at each station varied from 50-100 for the broadband stations deployed in 2007-2008, to as few as 5-25 for the short period stations subsequently deployed in 2008-2009. Stations recording fewer than 5 events were not included in the pseudo-reflection image.

All seismograms were detrended and filtered between 1-8 Hz to isolate the short period signal (and remove microseism and VLP signals. We rejected low signal-to-noise seismograms and other outliers (e.g., infrequent multiple bubble eruptions [*Rowe et al.*, 2000]) via a quality control algorithm based on standard deviation and correlation with respect to the net event stack. Thirty seconds of seismogram coda, starting 7 s after the onset of the eruption were then correlated for all component combinations and amplitude normalized by the standard deviation of the ZZ component of the correlation tensor, yielding six unique Green's functions for each station (i.e., ZZ, RR, TT, ZR, ZT, RT, where Z, R, and T are vertical, radial, and transverse components, respectively, with the radial being set up as North). Note that Green's tensor is defined as:

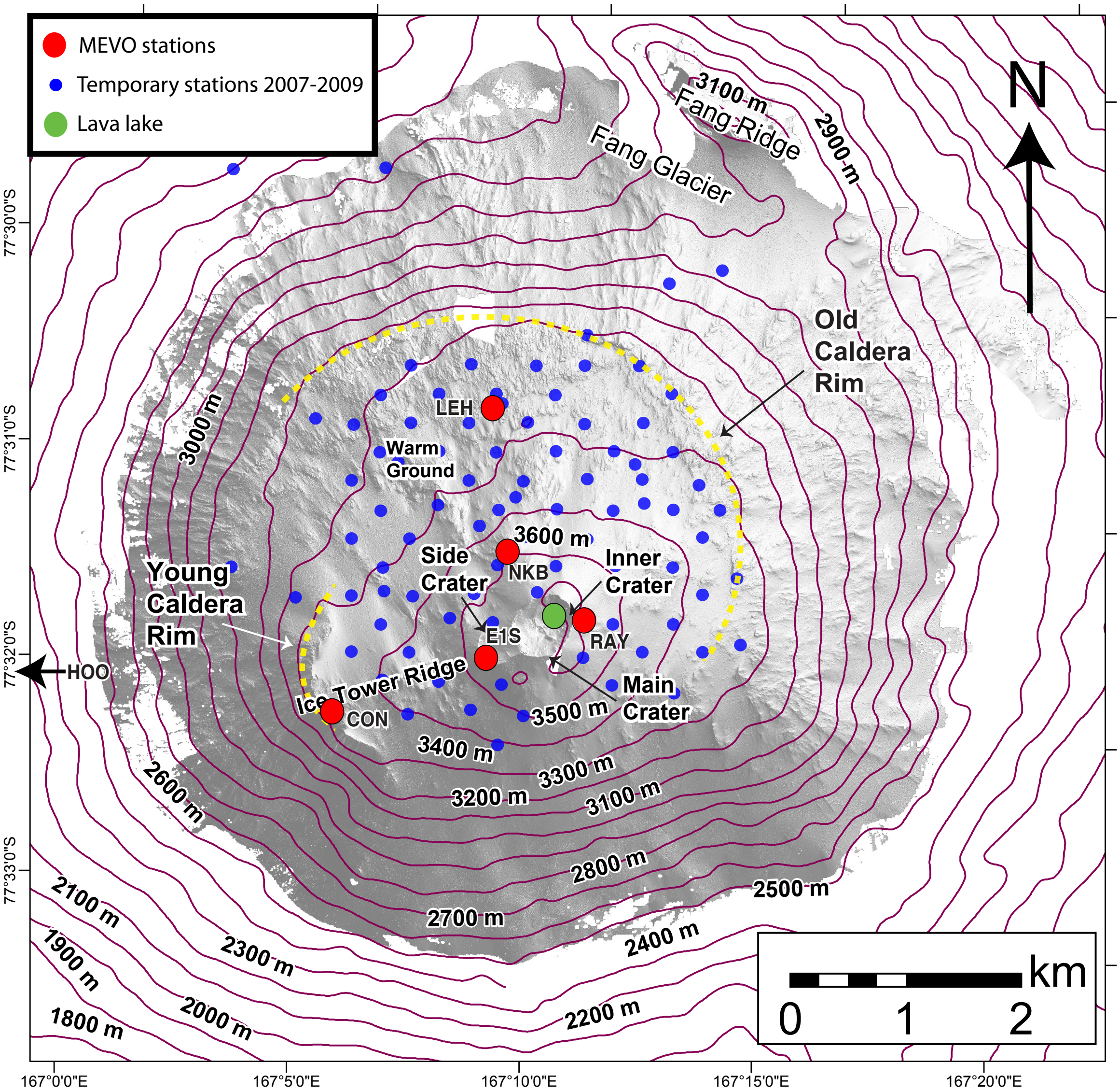

Figure 2.3: Map of Erebus volcano with associated surface geological features, and the deployments used in this study.

$$G_{ij} = \begin{bmatrix} G_{RR} & G_{RT} & G_{RZ} \\ G_{TR} & G_{TT} & G_{TZ} \\ G_{ZR} & G_{ZT} & G_{ZZ} \end{bmatrix} \tag{2.9}$$

For a single station correlation $G_{ZR} = G_{RZ}$, and so on, leaving only 6 independent Green's function components. Intuitively, each recovered Green's function can be interpreted as a reflection experiment with a single collocated source and station (Figure 2.4).

To permit back-propagation, we assume that arrivals in the Green's function are generated via Born scattering, i.e., a single scatter approximation. This assumption has several implications, notably that the Green's functions cannot contain P-S or S-P conversions (as for a collocated source and station, single scattering is generated from surfaces perpendicular to the ray path, thus negating the potential for wave type conversions). Furthermore, this approximation loses accuracy at later times in the Green's function due to the increased likelihood of multipathing, though shallow arrivals are likely well represented. Figure 2.5 shows an example of the 6 component of the Green's function gather at station CON.

We may further extract raypath information by projecting the estimated Green's functions onto a series of unit vectors over all space, and keeping only the maximum value at every time sample to avoid the computationally expensive step of first rotating the raw data and then recalculating the Green's tensor at every step, we adopt a "post correlation" approach as follows. The seismogram projected onto the unit vector may be formulated as

$$\mathbf{A} = a_x \cdot \mathbf{X}(t) + a_y \cdot \mathbf{Y}(t) + a_z \cdot \mathbf{Z}(t) \tag{2.10}$$

Where $a_x = \cos\theta_1 \sin\phi_1$, $a_y = \sin\theta_1 \sin\phi_1$, $a_z = \cos\phi_1$, with angles obeying spherical coordinate conventions, and a_x, a_y, and a_z represent the radial, transverse,

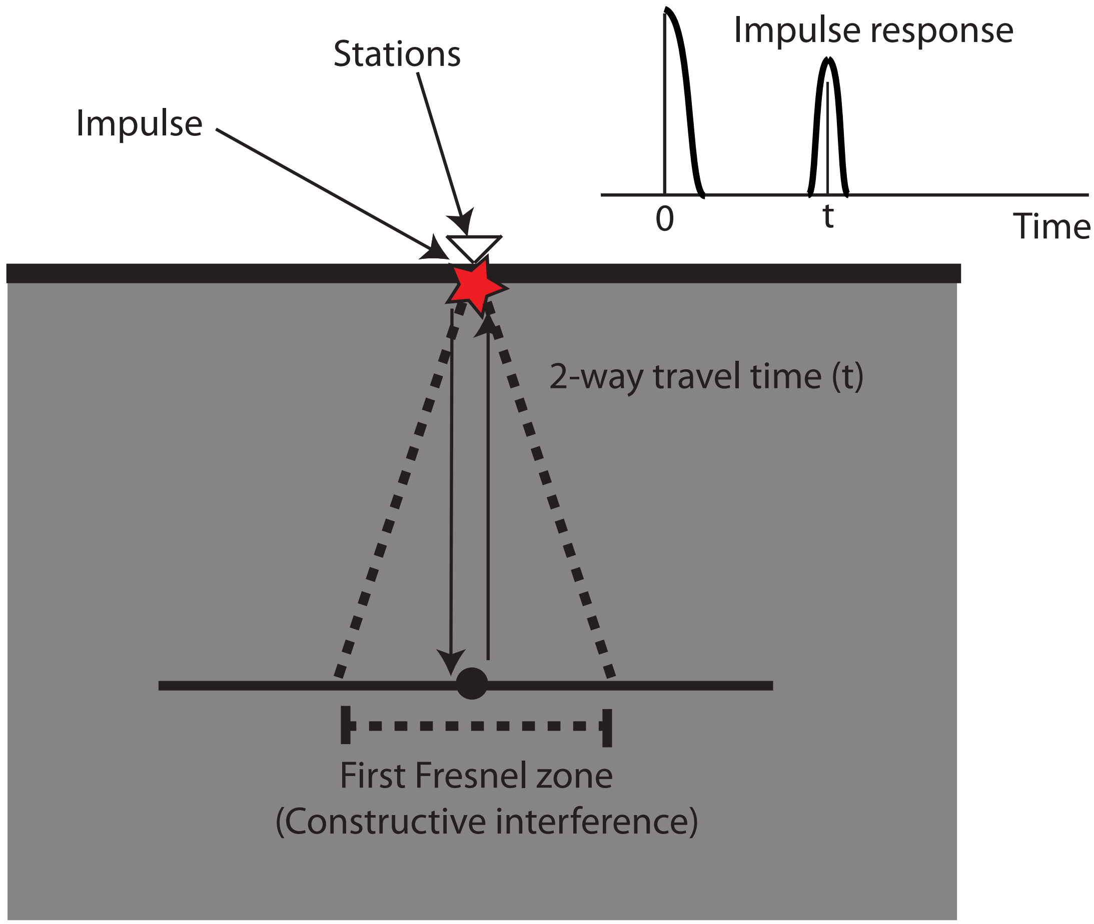

Figure 2.4: Simple toy example of a reflection experiment featuring a collocated impulsive source and station, with a single scatterer embedded in an otherwise homogenous medium. The impulse response, without multiples, can be described as a peak at zero time (from the impulse being generated at the station), and a delayed arrival representing the single scattered arrival. Note that for a given reflector, arrivals within the first Fresnel zone of the wavelength will stack coherently in the Green's function, creating a tradeoff between resolution and feature amplitude.

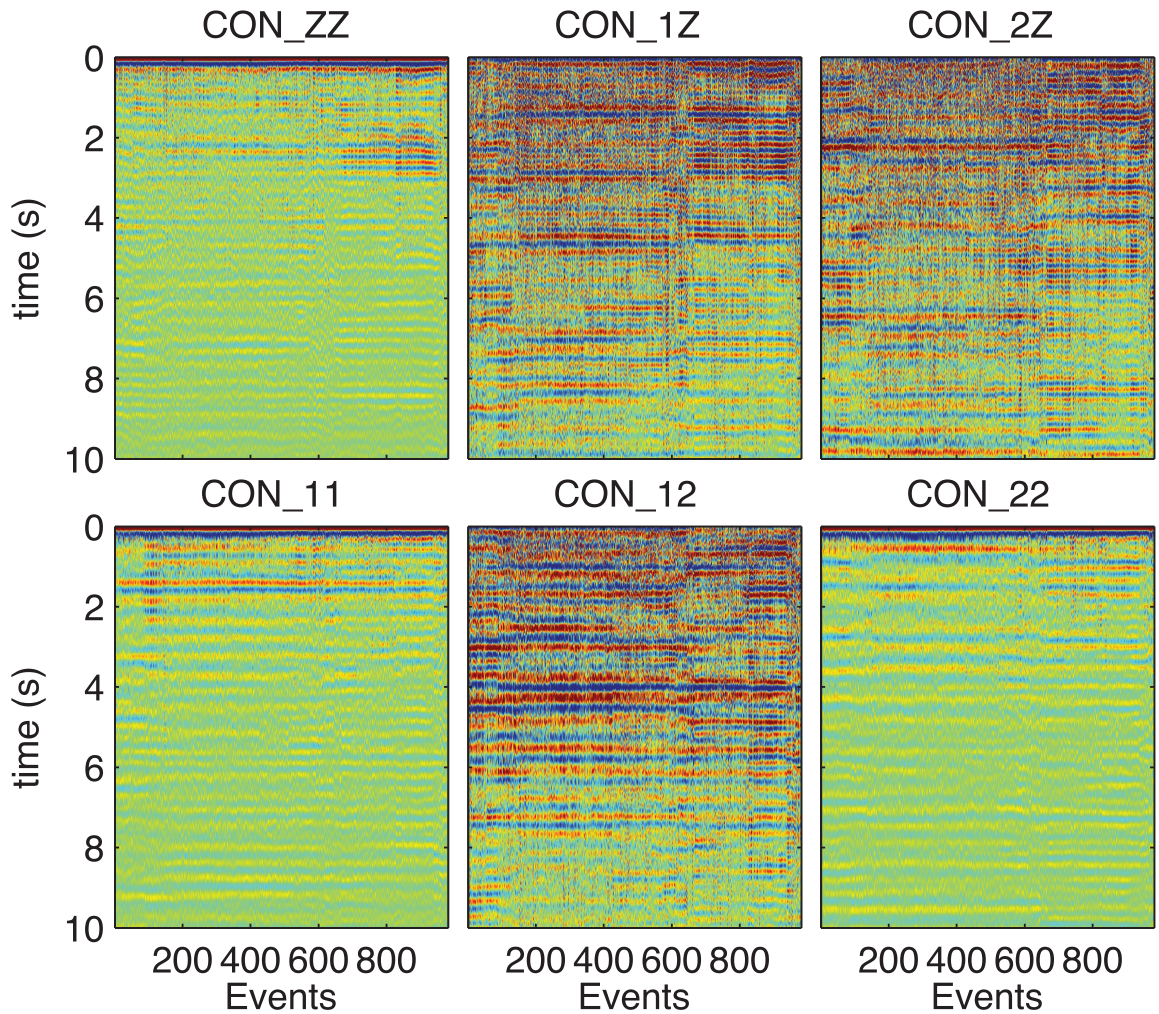

Figure 2.5: 6 components of the estimated Green's tensor at station CON, for 1000+ events.

and vertical seismograms. Subsequently, the rotated autocorrelation Green's tensor estimate may be formulated as:

$$\begin{aligned}
&\mathbf{A} \star \mathbf{B} = \\
&\qquad (\mathbf{X} \star \mathbf{X}){a_x}^2 + (\mathbf{Y} \star \mathbf{Y}){a_y}^2 + (\mathbf{Z} \star \mathbf{Z}){a_z}^2 \\
&\qquad + 2(\mathbf{X} \star \mathbf{Y})a_x a_y + 2(\mathbf{X} \star \mathbf{Z})a_x a_z + 2(\mathbf{Y} \star \mathbf{Z})a_y a_z \; .
\end{aligned} \tag{2.11}$$

We apply this to a full swath of angles covering the unit sphere, and keep only the maximum amplitude values at every sample of the autocorrelation in an updating manner, so that the end result is a vector containing only the absolute maximum values of the Green's tensor with associated values of θ and ϕ for every sample. Note that this is equivalent to finding the eigenvector associated with the largest eigenvalue for every time sample of the Greens tensor estimate via principal axes decomposition. In practice, a faster algorithm may be built this way, and we also recover information on particle motion ellipticity. For a given Green's tensor G, the eigendecomposition of G may be expressed as:

$$G = Q\Lambda Q^{-1} \tag{2.12}$$

The columns of Q are the eigenvectors of G, and Λ is a diagonal matrix containing the eigenvalues of G. Intuitively, the eigenvectors are the 3 orthogonal axes of maximal particle motion of G, and the eigenvalues are the amplitude weights of each eigenvector. Future uses of this method should use the eigendecomposition formulation, though it is inherently equivalent to manual rotation. Figure 2.6 presents a conceptual depiction of the method described above.

Consequently, we then pick the largest maximums in the amplitude vector and migrate them back into the volcano through an arbitrary velocity model (here,

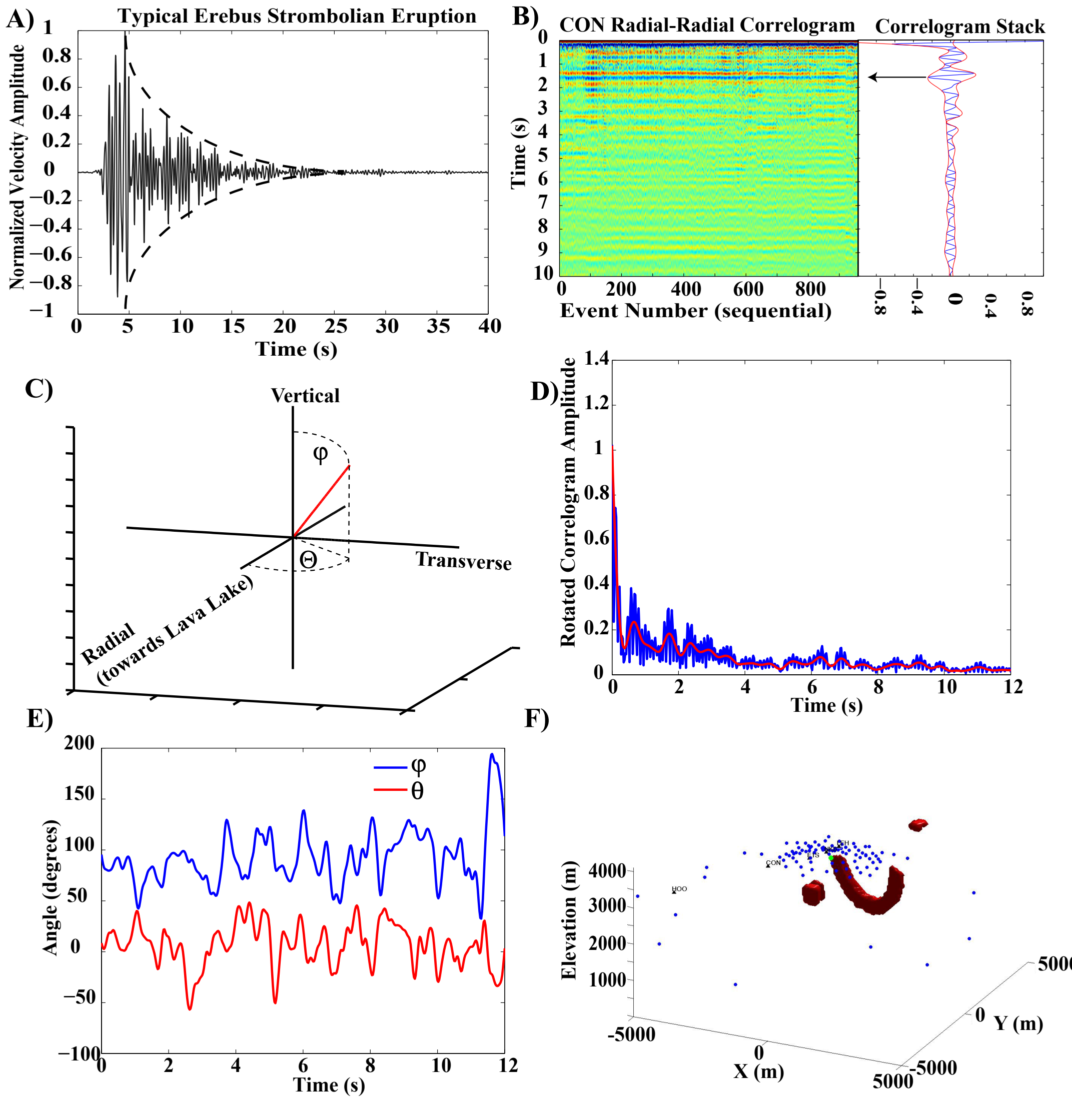

Figure 2.6: **A**) Representative band-pass filtered (1-8 Hz) short-period vertical-component velocity seismogram from a lava lake Strombolian eruption recorded at station CON, located approximately 2 km from the lava lake. The coda shows an emergent onset, a pronounced exponential decay, and distinct sub events from the highly scattering media. **B)** Example stacked radial-radial correlogram [from over 900 individual similar lava lake eruptions] for station CON displaying strong and consistent scattering features. Six such correlograms for each three-component station are evaluated to construct a time-dependent symmetric 3 by 3 elastodynamic Green's tensor. **C)** Unit vector polar coordinate system used for Green's tensor rotation to optimize scatterer detection. **D)** Example of an optimally rotated Green's function vector (station ETS50) with corresponding ϕ and θ unit vector solutions as a function of correlogram time in **(E)**. **F)** Example sensitivity kernel for a synthetic arrival in the amplitude vector, showing an arc-shaped S-wave kernel and a dual point-like forward and backward P-wave kernel. From [*Chaput et al.*, 2012].

V_p = 2.3 km/s, V_s = 1.27 km/s) as both P and S wave solutions defined by the particle motion angle solutions (see Figure 2.6e-f). Had we chosen to also consider cross-station correlations, we would have had to include the additional P-S and S-P sensitivity kernels in the back projection, which would have added a greater degree of noise to the model. Furthermore, cross-station correlation would likely only yield useful information for stations near one another since the volcanic edifice is extremely complex (e.g., consider the difficulty of interpreting a single station reflection experiment with a source on one side of the volcano, and the receiver on the other.) Furthermore, we may choose to apply a wave type "probability filter", to reduce noise generated by random stacking of unlikely raypaths (Figure 2.7). This is accomplished by defining station-specific geometrical penalty functions which evaluate the likelihood of an arrival being P-P or S-S based on where the strongest scatterers would generally reside, i.e., for a volcano, centrally.

Following correlogram normalization by their standard deviation, the largest scattered arrivals typically have an amplitude of 4-5 before wave type weighting is applied, which reduces the amplitudes on average by a factor of $\sim$3. As body wave scattered energy from point scatterers will suffer a theoretical amplitude loss of $1/r^4$ with source-scatterer distance, a corresponding distance correction is applied to the amplitude stack.

Figure 2.8 shows a series of depth slices of scattering intensity within a roughly 5 by 5 km grid extending down to sea level with a map view origin at the position of the lava lake. Active-source travel times recorded by the dense near-summit seismographic deployment shown in Figure 2.3 have recently been used to tomographically image strong shallow P wave velocity anomalies [*Zandomeneghi et al.*, 2012]. The amplitudes of the low velocities imaged (corresponding to absolute velocities below 2 km/s) in the regularized tomographic

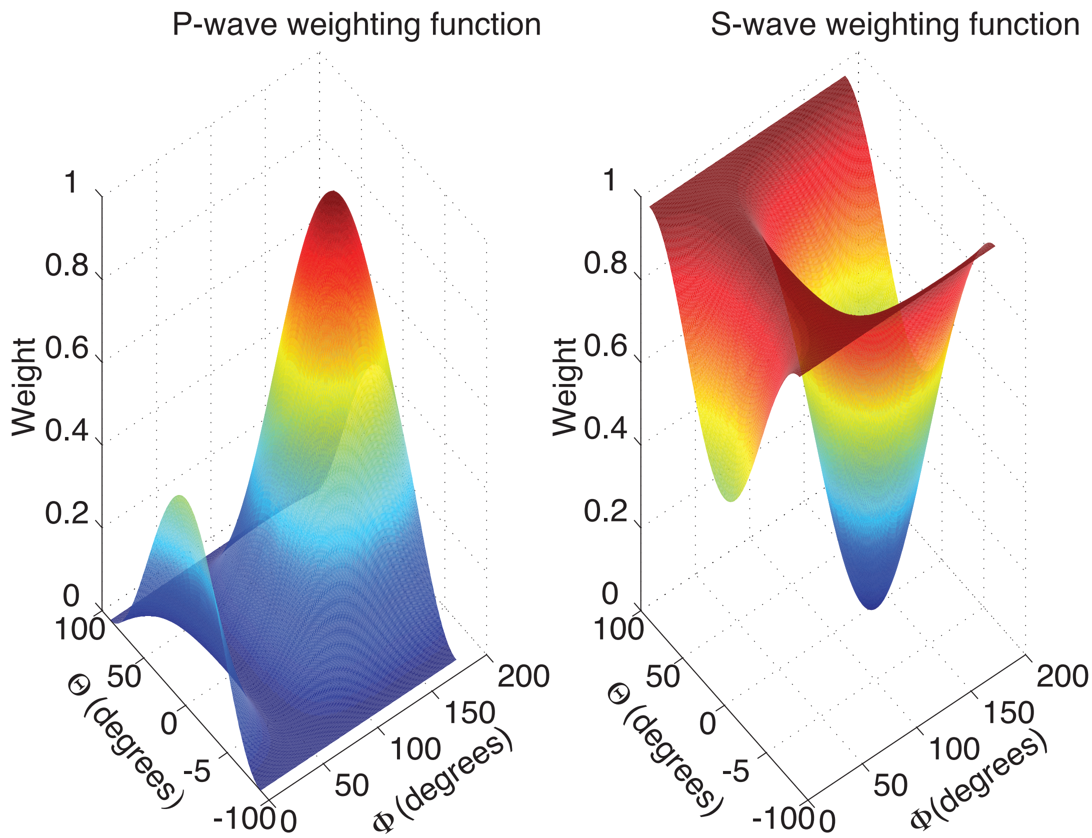

Figure 2.7: Example of a weighting function designed for a station on Erebus. For each maximum picked in the amplitude functions (Figure 2.6d), corresponding particle motion solutions (Figure 2.6e) are used to migrate arrivals into the volcano. For a station set on a 45 degree slope and with main scattering bodies estimated to reside centrally and, for this example, 45 degrees down from the horizontal, ϕ = 135 degrees and θ = 0 degrees, would correspond most likely to a P-P reflection, while an S-S reflection would be most likely for $\phi = 45^\circ$ and any value of θ. Note that these weighting functions are applied to reduce noise, but are not absolutely necessary, as models generated without them retain the same features described in the main text. From [*Chaput et al.*, 2012].

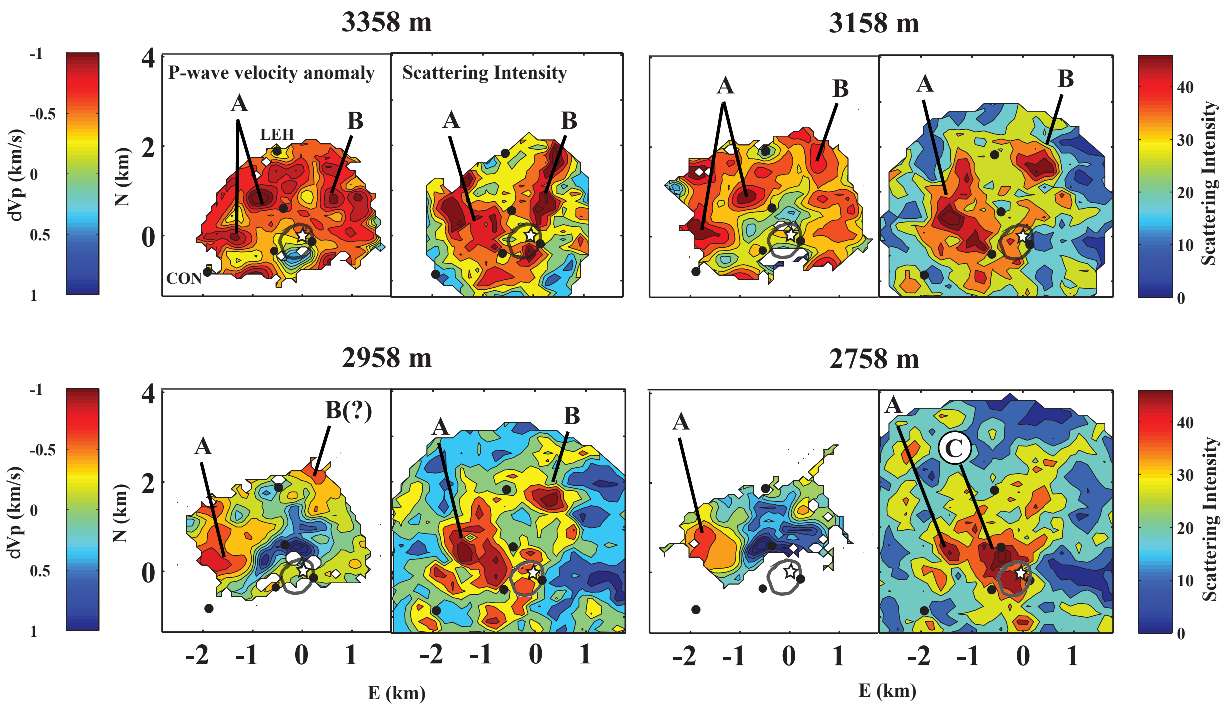

Figure 2.8: Scattering intensity depth slices for Erebus Volcano (right panels) and active-source tomography P velocity anomalies (left panels) at specific elevations (the volcano summit and lava lake surface are at elevations of 3794 m and 3490-3520 m, respectively). Low velocity P-wave anomaly regions are likely to harbor magmatic system elements, while areas of strong scattering intensity indicate strong seismic impedance contrasts (such as those expected at the boundaries of the magmatic system at or other strong discontinuities in elastic properties). The scattering amplitude scale is capped at a scattering intensity value of 46, which corresponds to between 20 and 50 stacked consistent migrated arrivals, although amplitudes as high as 75 are detected in these images. Anomalies labeled A, B and C correspond to especially strong scattering regions that are associated with low seismic velocities. The strongest scattering anomaly, C, resides approximately 1 km below the volcano summit and 0.75 km below the lava lake. The white stars denote the location of the lava lake, and the black circles denote the permanent MEVO stations (Figure 2.3). From [*Chaput et al.*, 2012].

inversion are consistent with near-summit magma or partial melt, and are displayed in the left panels of Figure 2.8.

Most of the eruptive energy falls between 1-8 Hz, thus setting theoretical constraints on the spatial resolution of the method (see Figure 2.4). The strongest scattering and low velocity anomalies occur along two prominent trends (A and

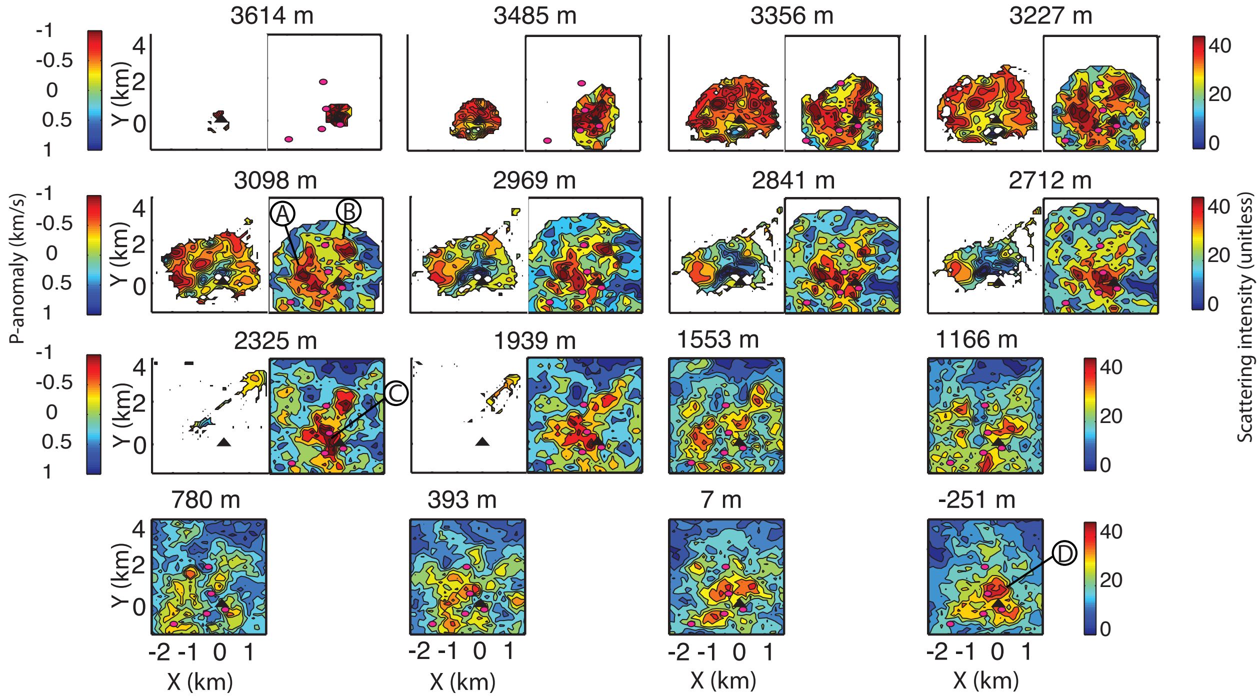

Figure 2.9: Expansive slice set for the scattering image compared with the tomography generated model. Note the persistent set of features to the West-Northwest and Northeast that occur in both models, though the raypath density of the tomography rapidly falls off after an elevation of ∼2700 m, shortly before the strongest scattering feature emerges. Note also the emergence of a deeper scattering at ∼0 m elevation, as also noted in Figure 3 of this Supplement. Strong features are noted by A, B (elevation 3098 m), C (elevation 2325 m), and D (elevation -251 m).

B of Figure 2.8), that extend to the west-northwest and north-northeast of the lava lake, respectively, and that merge into a very strong (the strongest scattering feature overall), centrally located structure (anomaly C of Figure 2.8) by approximately 1 km below the summit, or 750 m below the surface of the lava lake. The conduit and other features necessarily become increasingly difficult to image with increasing depth because of geometrical spreading, seismic attenuation and increased likelihood of higher-order multipathing. Figure 2.9 shows a denser set of slices as compared with tomography, shower the additional emergence of the feature at a ∼4 km depth.

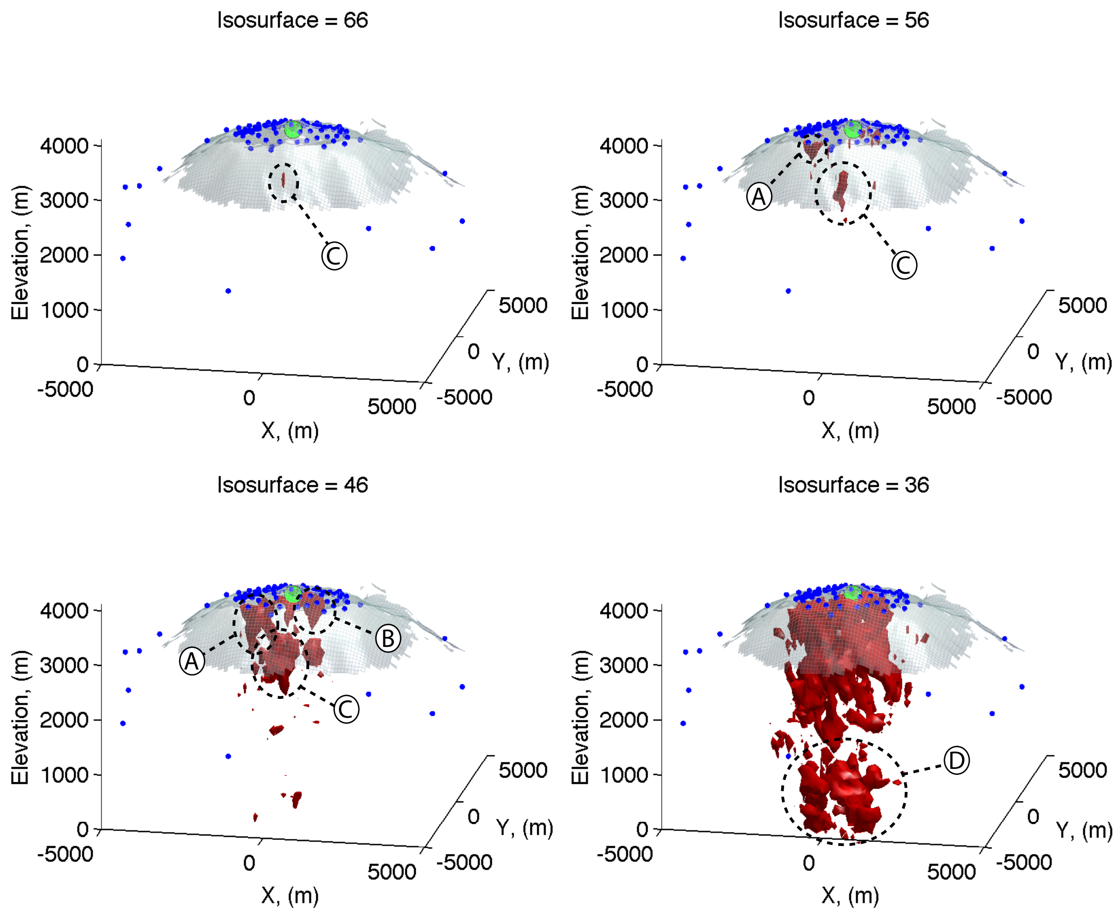

Figure 2.10: Isosurface plots of scattering intensity for various scattering values. Lower-amplitude isosurfaces expand/contract the scatterer image. Note that the strongly scattering near surface feature hypothesized to represent a sub-conduit feeding the lava lake bifurcates sharply towards the west and northwest, and then centralizes in a shallow magma chamber near ∼2700 m elevation. Features also emerge as deeply as ∼4 km, though there is increasing uncertainty as to the location of such features given the Born approximation used here. From [*Chaput et al.*, 2012].

The combined scattering and tomography images indicate a complex and narrow near-surface conduit system with significant off-axis and highly inclined elements that simplifies centrally at depth obviating simple models of a central conduit extending straightforwardly to the vent at this volcano. Figure 2.10 displays a 3D isosurface mapping of the slices represented in Figure 2.8.

A common conceptual model for the generation of large gas slugs in Strombolian systems requires a constricted and/or inclined conduit geometry that provides locales where exsolved gas can coalesce until a critical slug size is achieved that can ascend buoyantly to eruption. The complexities of the shallow structure recovered here are consistent with such a view, with the occurrence and gas state of multiple vents in the crater, and with dispersed recent lava flows on the Erebus summit plateau that may have arisen from off-axis vents [*Harpel et al.,* 2004]. Additional corroborating evidence for a geometrically complicated conduit system [*Aster et al.,* 2008] is presented by the generation of near summit VLP signals during final slug ascent and subsequent lava lake refill. The centroid location of these signals, which are believed to be excited by flow through a prominent upper magmatic system constriction is also off axis, west to north-west of the lava lake, and at a depth of approximately $\sim$400 m below the lava lake [*Aster et al.,* 2008], or $\sim$3200 m elevation. This places the VLP centroid along the azimuth of the most prominent shallow high scattering and low velocity anomaly (feature A in Figure 2.8).

As mentioned before, comparative studies of gas compositions from the main lake with a secondary lake (Werner's fumarole) have shown substantial variations, suggesting the presence of two distinct shallow intrusions feeding vents separated by $\sim$100 meters. The two anomalies noted in Figure 2.8 both "connect", in terms of scattering amplitude, to the inner crater, but their paths are distinctly W-NW for anomaly A, and N-NE for anomaly B. These paths are delineated in Figure 2.10 as well, and though there is no concrete evidence linking one or the other vent with either anomaly, it is nonetheless an interesting structural feature that is also mirrored in the tomography as low velocity anomalies. Given the simplistic nature of the back projection process (i.e., straight rays, constant velocity model), a few notable improvements, such as migration through a tomographically inferred velocity model, could vastly improve the accuracy of this approach, thus highlighting the advantage of multiple seismic data sets applied to the same system.

2.3.2 Additional tests

Following reviewer suggestions for the submission of [*Chaput et al.,* 2012], we create additional tests to verify the reliability of the results presented here. Typically, 3D volume imaging is performed via tomography, where there exist standard methods, such as checkerboard tests, to determine the inversion's ability to recover details given a known true model. Given that the approach detailed here has no precedent, and that resolution does not in fact depend on raypath density as there is no inversion step whatsoever, such tests are not applicable. Instead, we conduct a few steps tailored to this scattering experiment to determine both the relevance of amplitude and particle motion, and the level of robustness of the recovered image.

We choose to perform a test aimed at evaluating the coherency of angle solutions as compared to a randomized set of angle solutions. We take the estimated maximum amplitude Green's function vectors, as calculated from the method described above, assign a randomized set of angle solutions, and migrate them into the volcano. Figure 2.11 depicts the maximum scattering intensity with depth, and we may note that the random angles show a very rapid exponential fall off with little feature resolution, whereas the solution angles maintain higher scattering amplitudes throughout the model, with intensity resurgence corresponding to the prominent features identified in this paper. However, the shallowest maximal amplitude is similar in both cases, and this is an effect of the block size used to bin scattered arrivals. The earlier the timing, the shorter the propagation path, and therefore the lesser the influence of the propagation direction in terms of what blocks are affected by a given arrival. The results in this case clearly indicated that the addition of angular path information drastically increases the coherence of the image.

We also perform a station reduction test, where we aim to see how well the primary features identified in this paper can be resolved using a smaller random subset of stations. Figure 2.12 depicts 8 examples of images with decreasing random subsets of stations. We repeat this text many times, and note that the general features identified in the full scattering image of Figure 2.10 converge consistently when over $\sim$25 stations are used, though surprisingly good models may occasionally be recovered from as few as 10 stations before the artifacts contaminate the volume (note Figure 2.12, panel 8, 4 stations).

Figure 2.13 displays the 3-dimensional cross-correlation index of 500 different iterations of subsets with respect to the best resolved image (i.e. 94 stations). Note that the variation in correlation index also increases for smaller subset numbers, and falls to noise levels for subsets containing fewer than 10 stations. Beyond these tests, it is difficult to infer the exact spatial resolution for this sort of study in terms of the smallest identifiable feature.

In a conventional reflection survey, the spatial resolution is determined by the Fresnel zone of the wavefield frequency (e.g., Lindsey, J.P, The Fresnel zone and its interpretive significance, Geophysics: Leading Edge, 1989), assuming a flat layered medium, whereas resolution of a point scatterer is perfect and frequency

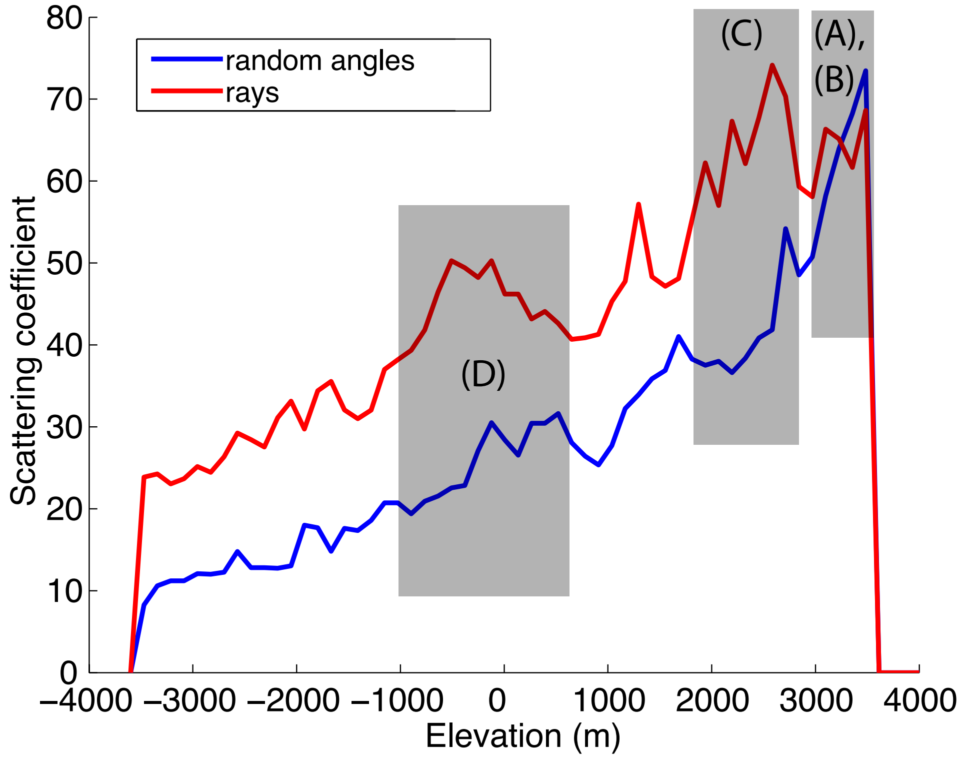

Figure 2.11: Application of randomized ϕ and θ solutions to the calculated Green's function maximum amplitude vectors, to evaluate any change in scattering intensity with depth. We would expect scattering intensities to remain high at the shallowest layers, as we are still using the calculated amplitude functions, but the maximum scattering amplitude falls off exponentially with little feature resolution as shown by the smoothness of the decay. The calculated particle motion solutions however yield several notable features, labeled A, B, C, and D to correspond to (Figures 2.8, 2.9), and demonstrate a much more gradual loss in scattering amplitude. From [*Chaput et al.*, 2012].

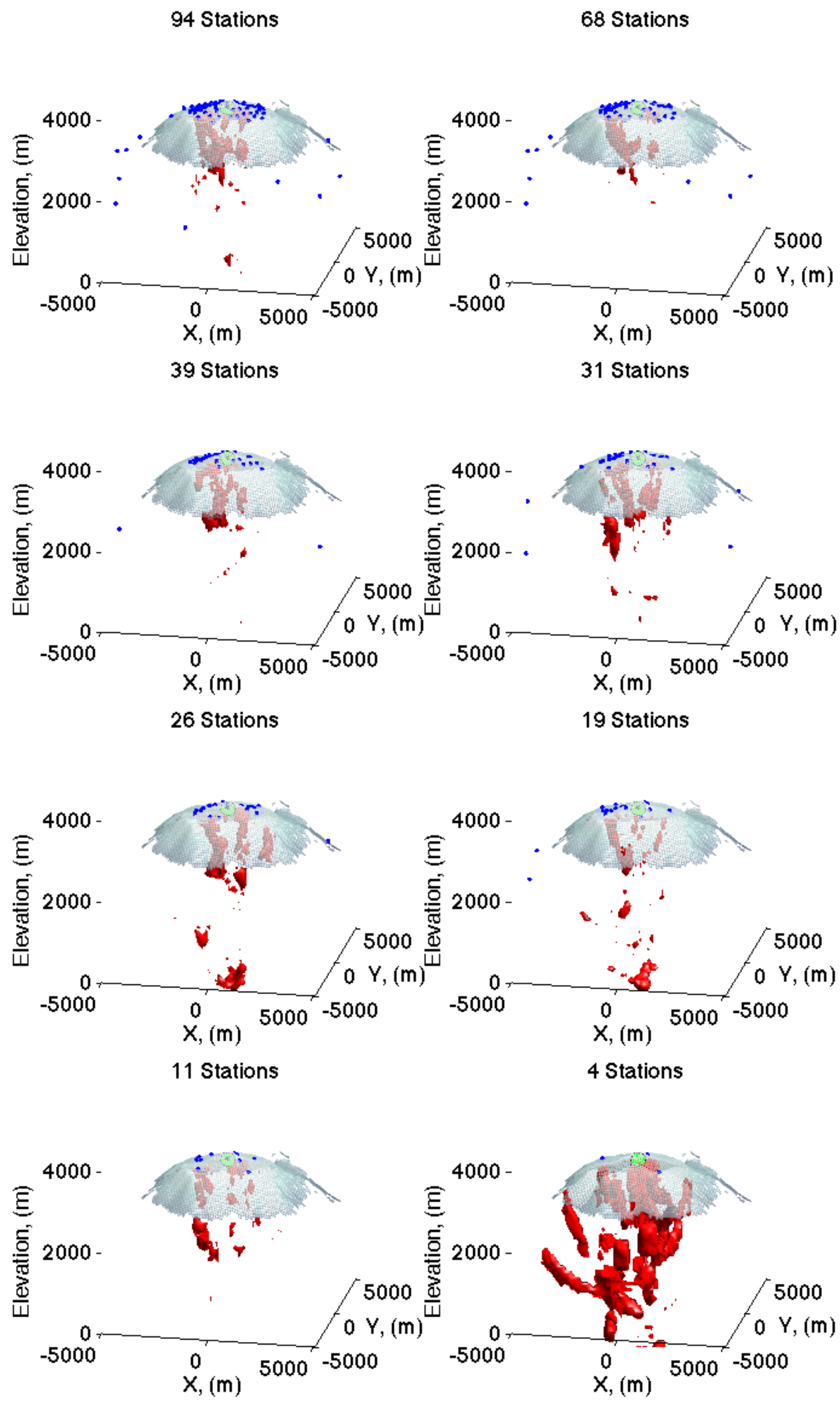

Figure 2.12: Example station reduction test showing effects of randomly decreasing station coverage. Prominent features A, B and C may reliably be resolved for subset numbers down to 30, but good models may still be obtained from as few as 10 stations. From [*Chaput et al.*, 2012].

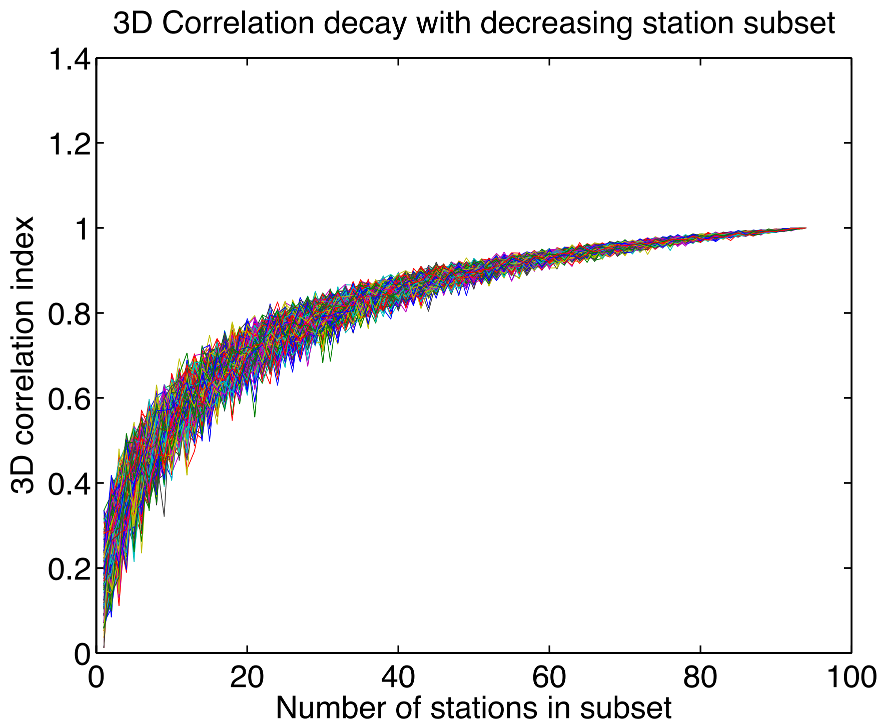

Figure 2.13: 3D correlation index of 500 iterations of subsets with respect to the best model. Note that the variability in correlation index increases substantially with decreasing station numbers, and falls into noise levels below ∼10 stations. From [*Chaput et al.*, 2012].

independent. Given the apparent geometrical complexity of Erebus' edifice, spatial resolution likely lies somewhere in between several tens of meters and several hundred meters, and there exists a tradeoff between feature spatial resolution and the amplitude of the feature in Green's function due to Fresnel stacking (see Figure 2.4).

2.3.3 Conclusions

We present a novel body wave seismic interferometry seismic imaging method and apply it to the highly scattering medium of an active volcano that is illuminated by repeating impulsive Strombolian eruptions. Using 92 short-period and broadband stations deployed during the 2007-2008 field seasons, and seismograms from $\sim$50 near-repeating Strombolian eruptions, we calculated single-station cross- and auto-component Green's function estimates and rotated them into absolute maximal vectors with associated angle solutions. We back-projected each optimally rotated Green's function determination into the volcano, using the time-varying angle solutions to define the raypath sensitivity kernels of each arrival, to reveal a map of scattering potential for the volcanic edifice. Results show a complex near-surface conduit system which bifurcates from the west to the northwest in the first 500 m below the lava lake, and strongly centralizes beneath the lava lake near 1 km below the summit. The low dip of the shallow conduit beneath the lava lake, as little as 15°, indicates a terminal structure that might control variable gas slug sequestration and thus Strombolian eruptive frequency, and link to the centroid VLP source excited by eruptions and subsequent magmatic flow during lava lake refill [*Aster et al.,* 2003, *Aster et al.,* 2008, *Knox,* 2012]. This view of a complex uppermost magmatic plumbing system is additionally consistent with modeling [*Lahaie and Grasso,* 1998, *Shaw et al.,* 1991] of volcanic systems that suggests that the substantial variation in scales of observable phenomena are best modeled by a system of connected micro-chambers exhibiting nonlinear interactive behavior.

These results further suggest new opportunities for active volcano monitoring and for the general imaging of strong subsurface seismic impedance contrasts. Given a sufficiently dense network of seismic stations and a suitably broadband natural or artificial noise source or collection of sources, such as internal natural seismicity, scattering images of an active volcano would facilitate 4-d monitoring of internal structure and time-lapse changes, especially when complemented with ancillary geophysical and geochemical data, such as provided by seismic tomography, GPS geodesy, thermal and gas emissions, and internal seismicity. Realization of this vision would require development of low-cost, robust (and perhaps expendable), telemetered sensor networks that could be readily deployed at high densities on active volcanoes.

CHAPTER 3

STRUCTURAL TEMPORAL VARIABILITY TRACKING AT EREBUS VOLCANO; TOWARDS 4D PSEUDO-REFLECTION SEISMOLOGY

3.1 Introduction

Monitoring temporal changes within the Earth (4-d seismology) using both natural and artificial sources is a topic of longstanding interest. In principle, with reflection or tomography studies, this simply requires impulsive sources of repeating seismic illumination and a fixed set of seismic stations. Although laboratory experiments suggest a number of interesting observables and processes may be detectable [*Crampin et al.,* 1984], implementation outside of tightly-controlled industry imaging has frequently been complicated due to the challenges of generating, synthesizing, or selecting suitably repeating sources, and commonly small degrees of temporal variation in Earth properties. Volcanoes are especially attractive targets for such study, given that large shallow stress and other changes accompany eruptive cycle, and abrupt and progressive evolution of magmatic and hydrothermal systems are a natural consequence of volcanic processes. A few examples of reported detections of volcano or volcano-regional temporal changes include velocity changes at Merapi Volcano from seismic multiplet analysis [*Poupinet et al.,* 1996, *Bianco et al.,* 2006, *Patane et al.,* 2006], who described changes associated eruptions of Mount Etna, [*Gret,* 2004, *Snieder,* 2006, *Snieder and Haggerty,* 2004] who studied phase changes in coda signatures as a proxy for source or structural changes within media, and [*Brenguier et al.*, 2008, *Sens-Schonfelder and Wegler,* 2006] who used ambient noise derived velocity models to correlate changes in eruptive behavior with velocity variations at Piton de la Fournaise volcano. The study by [*Brenguier et al.,* 2008] presented a particularly interesting prospect, where long duration correlations of ambient noise at Piton de la Fournaise volcano were used to correlate changes in Rayleigh wave velocities with eruptive episodes. As these particular changes in velocity occurred consistently anywhere from to a few days to a month before the transition from quiescence to explosive eruptive behavior, the velocity changes have been interpreted as magma injection episodes into a frozen dyke system previously identified by ambient noise tomography models [*Brenguier et al.,* 2007]. As such, at least for Piton de la Fournaise volcano, where periods of mild eruptive activity tend to be cyclic, seismic interferometry applied to ambient noise seems to have yielded a methodology for predicting eruptive activity. Note however that although this study was able to discern a general location of the magma injection events, the order of this location was at best several kilometers, therefore lacking in any constraints of how the magma chamber deformed during the episodes. Therefore, though ambient noise studies are robust and offer year round data coverage ideal for temporal variability studies, any information recovered will tend to lack spatial resolution. Whereas Rayleigh waves typically do not scatter on a scale of several kilometers, body waves generated by local events, typically containing spectral energy exceeding 1-5 Hz, will tend to contain information on near surface structure.

Here, we make use of the pseudo-reflection imaging approach as described by [*Chaput et al.,* 2012] based on body wave seismic interferometry [*Wapenaar,* 2006, *Snieder*, 2004, *Campillo*, 2003, *Shapiro*, 2004, *Claerbout*, 1968, *Roux et al.*, 2005] to estimate Green's functions from Strombolian eruption coda at a small number of long running stations (MEVO) on Erebus volcano, Antarctica. We map several distinct temporally varying features in Green's functions to a previously determined tomography/scattering model [*Chaput et al.*, 2012, *Zandomeneghi et al.*, 2012], and we further show that these changes are strongly correlated with variations in eruptive character, in particular, with timing differences between the onset of the short period bubble burst from Erebus' lava lake, and the consequent Very Long Period (VLP) signal associated with conduit system re-stabilization [*Knox*, 2012, *Aster et al.*, 2003, *Rowe et al.*, 1998]. The motivation here lies in the idea that bubble coalescence could be strongly affected by minute changes in conduit geometry, which would in turn affect the character of the high frequency Green's function. As shown in the previous Chapter, seismic interferometry fundamentally states that the auto- or cross-component Green's function between two seismic stations, or for a single station, can be recovered if the medium of interest is illuminated by dense and irregularly spaced broadband sources of either impulsive or uncorrelated continuous character. In such cases, the Green's function can be recovered by stacking the cross-correlated contributions from all discrete sources in the medium, or by simply correlating the equipartitioned coda between any two points in the medium. Furthermore, Chapter 1 has demonstrated fairly convincingly that short period coda, from eruptions or large icequakes, will tend to demonstrate equipartition at consistently similar frequency dependent ratios, thus satisfying the theoretical requirements for Green's function recovery. The results described below are from of a manuscript entitled "Temporally Varying Magmatic Structure at Erebus Volcano revealed by Correlations of Repeating Strombolian Eruption Coda Seismograms".

3.2 Green's functions on MEVO and passive 4D reflectivity

The MEVO network of permanent broadband stations, installed during the 2003-2004 field season, replaced a network of robust short period and infrasound stations, and has ultimately permitted the construction of a large data archive spanning almost a decade, encompassing everything from Strombolian lava lake eruptions [*Aster et al.*, 2003], to ice quakes, iceberg tremor, teleseisms, microseismic records, and infrequent signals such as ash vent eruptions and potential volcanic tremor to isolate the Strombolian eruptions from the extremely prevalent ice quake activity on the flanks of Erebus, which often carries the whole MEVO network and contains a very similar frequency spectrum as a typical eruption, we constructed a multi-station matched filter designed to identify signals with specific arrival moveouts. In essence, a template of manually picked eruptions recorded on MEVO broadband and infrasound stations is run through the raw archive like a comb in search for correlation peaks corresponding to eruptive signatures. A database of 2974 eruptions was thus constructed, with an estimated efficiency of over 90 percent. For more information on database construction and characterization, please refer to [*Knox*, 2012]. Figure 3.1 denotes the MEVO array, as well as many of the previously identified features of Erebus volcano's upper edifice.

We first generate single station Green's function estimates for the eruption database, and filter them between 1-8 Hz to isolate the short period signature. We then perform an eigenvector decomposition to retrieve 3D particle motions for each estimated Green's function, thus retrieving the Maximum Rotated Green's Function (MRGF) as well as particle motion eigenvalue/eigenvector pairs (for more information, see Chapter 2). The MRGF is intuitively obtained by calculating the radial-radial component of the Green's function when the original data is

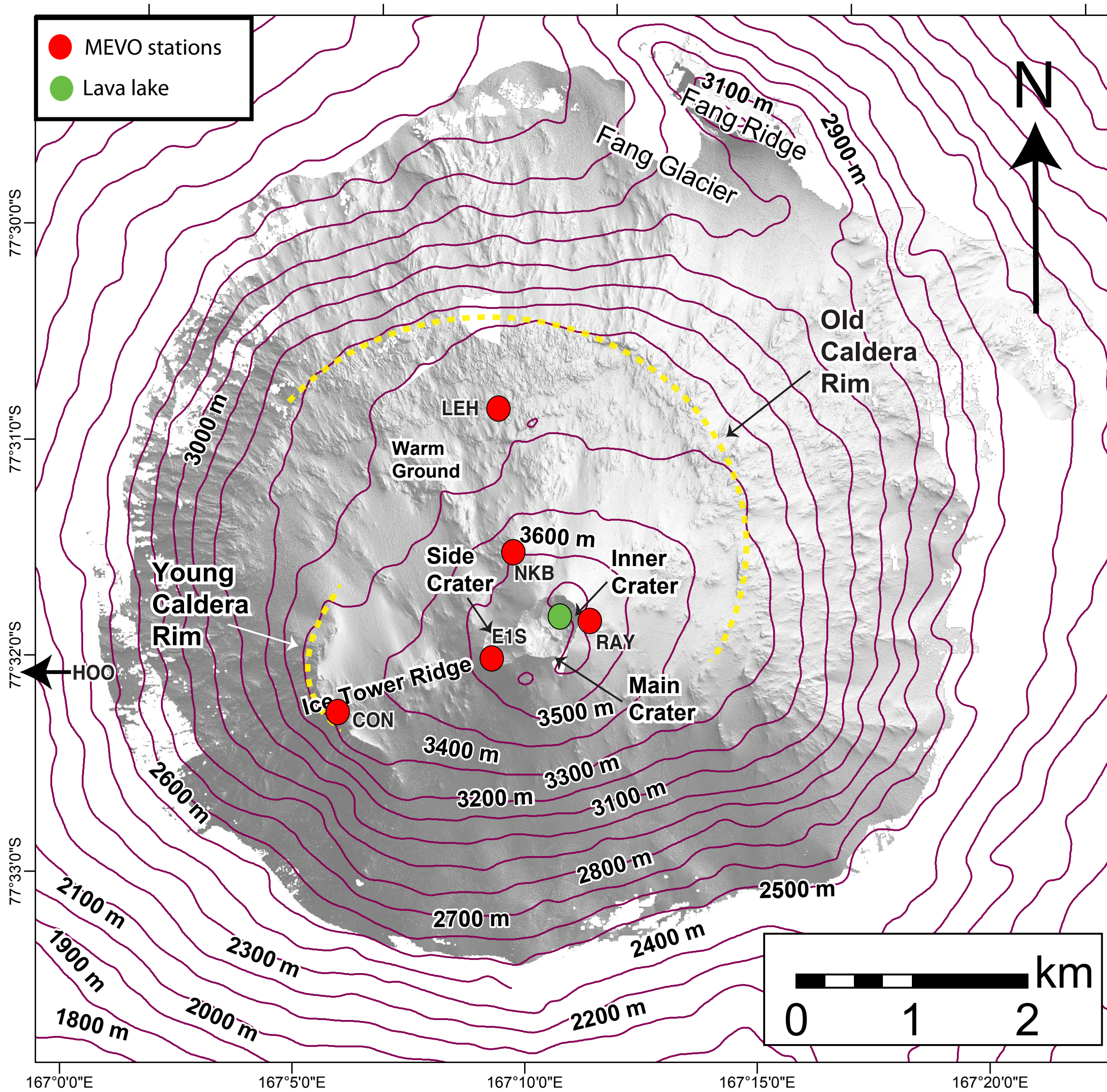

Figure 3.1: Map of Erebus volcano with associated surface geological features, and the location of the MEVO array used in this study. MEVO stations are denoted by red circles, and the lava lake a green circle.

rotated radially into the direction of maximum particle motion for every time sample. Recall, from Chapter 2:

$$G = Q\Lambda Q^{-1}, \tag{3.1}$$

where the columns of Q are the eigenvectors of G, and Λ is a diagonal matrix containing the eigenvalues of G. By weighing the MRGF by a ratio of eigenvalues defined as $(\lambda_1 - \lambda_2)/(\lambda_1 + \lambda_2 + \lambda_3)$, where λ_1 is the largest eigenvalue, arrivals featuring highly polarized particle motions are accentuated in the Green's function, whereas arrivals featuring high degrees of ellipticity are attenuated [*Aster et al.,* 1990]. This is to prevent arrivals constructed from the interference of multiple raypaths from being incorrectly back-propagated into the volcanic edifice. For more information on the back-propagation approach, see Chapter 2, and [*Chaput et al.,* 2012]. Figure 3.2 shows examples of computed smoothed eigenvalue-weighted MRGF estimates for 5 MEVO stations used in this study. Several arrivals of interest are denoted for further use as located features. Recall from Chapter 2 that every time sample in the MRGF has an associated value of ϕ and θ, as well as a ratio of eigenvalues describing the ellipticity of the particle motion solutions. Some quick observations may be made, such as areas of stability in the MRGF estimations as well as periods of rapid change. to deterministically identify such periods of change, we compute the absolute trace by trace differences for the first 5 seconds of the MRGF and plot them with respect to event-time.

Strombolian eruptions at Erebus also produce Very Long Period (VLP) signals associated with magma conduit reload and re-stabilization following the bubble burst that generates the short period signal. The signature of this VLP is very stable [*Rowe et al.,* 1998], though systematic temporal offsets between the

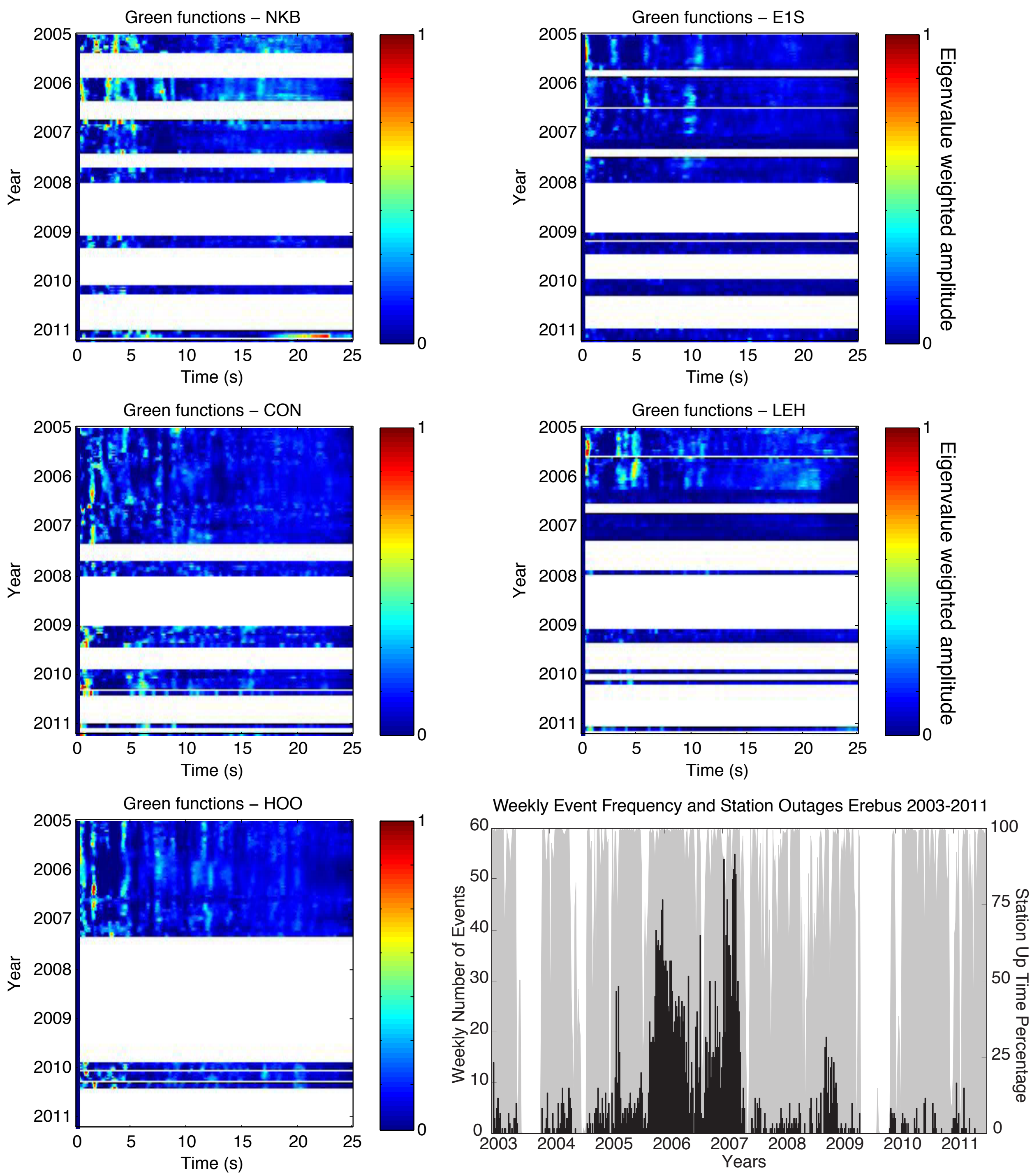

Figure 3.2: Eigenvalue weighted MRGFs for MEVO stations, along with the eruptive frequency histogram from Chapter 2. The weighted MRGFs show areas of significant temporal variability.

short period signal and the VLP onsets have been observed [*Knox,* 2012], pointing to structural changes in the conduit system as responsible for variations in re-stabilization rates for the conduit system post-eruption. As such, we present a comparative platform on which to study abrupt changes in both Green's function signatures and VLP-SP timing lags. Using the complete pseudo-reflection model generated with the dense deployment of 2008-2009, we also back-propagate several features at station CON displaying particularly obvious changes concurrent with VLP-SP lag variations. Figure 3.3 shows the Green's function variability plotted between $\sim$2005-2008 at station CON, which features the lowest noise levels and longest up times, compared with VLP-SP lags and the summed trace to trace differences computed for stations CON, LEH and HOO. These differences are computed by taking the trace by trace differences for each event bin, normalizing by standard deviation, removing the mean, and setting all negative values to zero. The results are them summed for CON, LEH and HOO. We may immediately note that VLP-SP events denoted 2-5 correlate well with large excursions observed at these stations, supporting the idea that rapid structural change can result in delays in the initiation of conduit reload. The first VLP-SP excursion is poorly sampled by events, and thus not easily identified in the Green's functions. Stations E1S and NKB are generally very noisy, perhaps on account of near field effects of the source with respect to equipartition, and excluded from this analysis.

Mechanisms involving the propagation of Stoneley waves through the conduit system as a way to initiate the start of the reloading process have been proposed [*Knox,* 2012], and given the seemingly systemic nature of the structural variations observed in the Green's functions rather than little to no structural shifts, this proposed mechanism is attractive. We focus here on two VLP-SP events, 1 and 4-5, to estimate the locations to which our sparse array is most sensitive. Figure 3.4

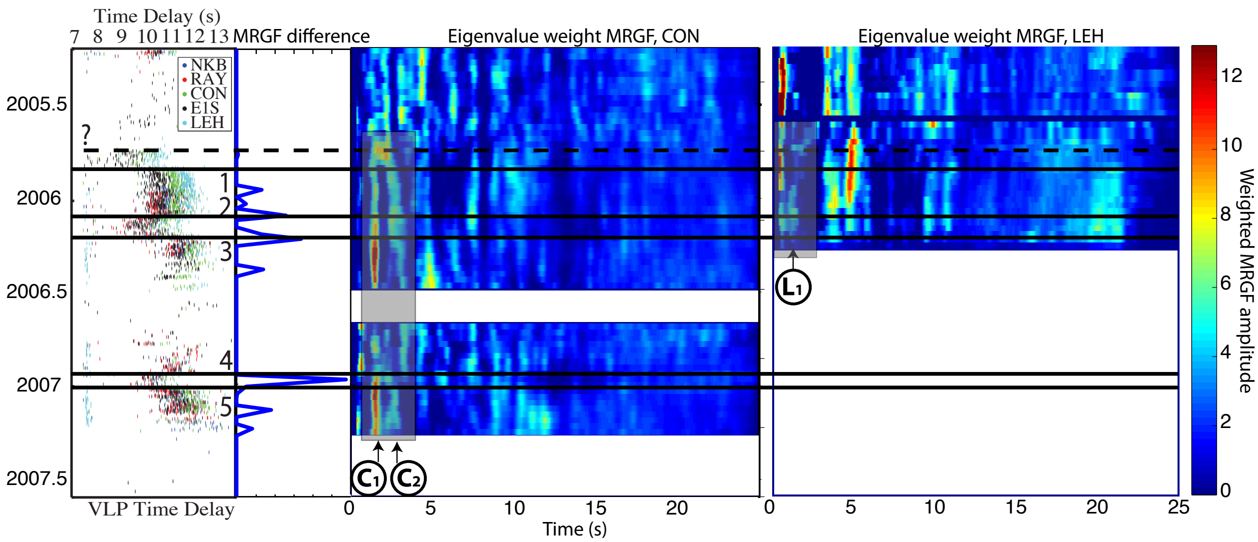

Figure 3.3: Eigenvalue weighted MRGF at stations CON and LEH compared to trace to trace differences in the MRGF and the variation of VLP-SP timing lags. Areas of rapid VLP-SP changes are denoted 1-5 (left panel) with a question mark denoting an additional potential rapid change. The MRGF differences are computed from the sum of stations CON, LEH and HOO, normalized by standard deviation, de-meaned, and with values below zero set to zero. The MRGF differences are not displayed for event/bins smaller than 5 events. Three particular features denoted C_1, C_2 and L_1 are noted for their variability during dense event sampling, their early arrival times, and their high probability of being P-P reflections rather than S-S based on particle motions.

shows examples of back propagated arrivals into the scattering model developed in Chapter 2, for event 1, for LEH, and 4-5 for CON.

Given the the ability to precisely locate individual arrivals of interest in 3D presented by this approach, we may therefore pinpoint areas of the volcano where significant change occurs in the MRGFs. We focus on the first 5 seconds of the Green's function gathers, as later arrivals are subject to an increasing likelihood of multipathing, thus resulting in erroneous back-propagations with Born scattering. Given that in Chapter 2, we determined that the full scattering model converges consistently for station numbers larger than ∼30, fully back-propagating all the MEVO arrivals into the volume would contain too much noise to be meaningful.

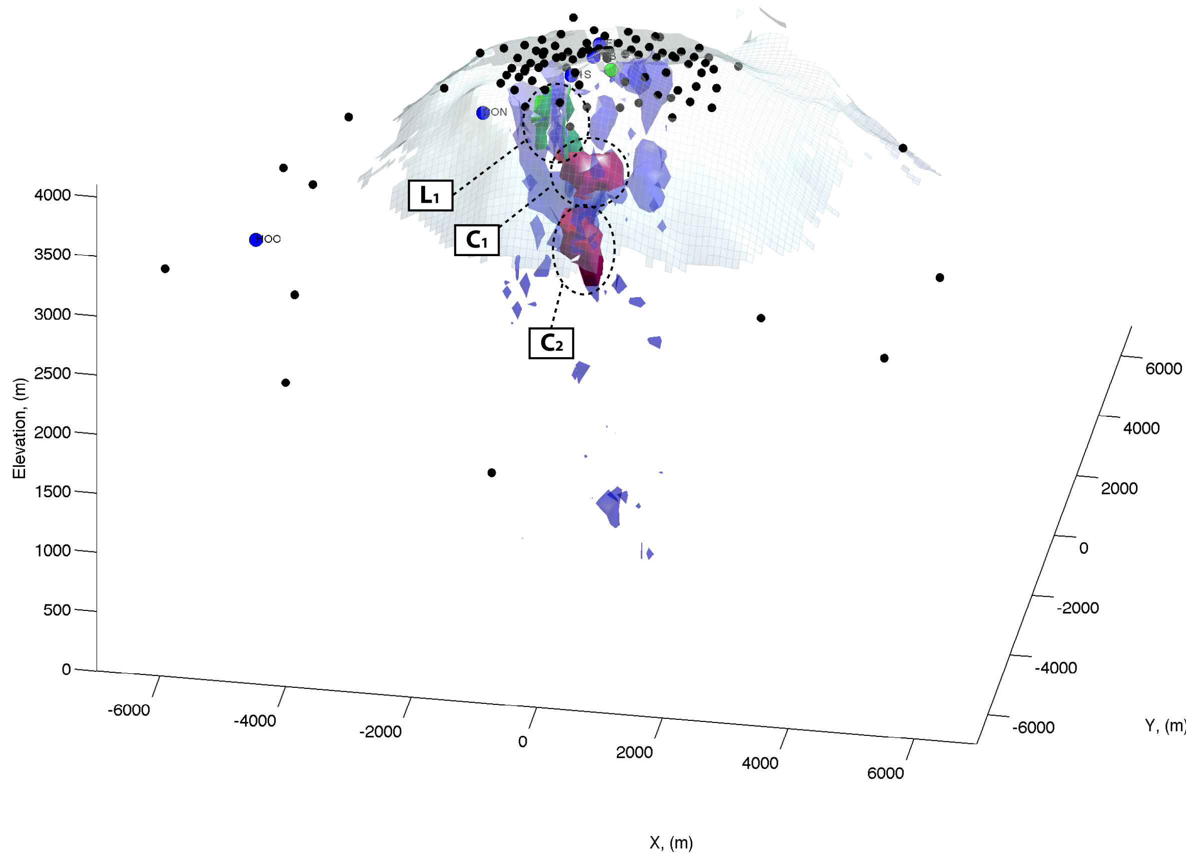

Figure 3.4: Pseudo-reflection back-propagation of features C_1, C_2 and L_1. All three features intersect well with the previously determined scattering model in Chapter 2, strongly supporting a W-NW oriented shallow magma system with a more centralized body at depth. The sudden increase/decrease in scattering intensity for these features reflects systemic changes in the volcanic system rather than highly localized conduit constriction/change.

We therefore choose several notable arrivals with high signal-to-noise ratios and large eigenvalue ratios that are likely to be P-P reflections, because of that mode's tighter raypath constraint, to demonstrate examples of temporally varying located features.

We back-propagate as a P-P reflection the arrival (noted as L_1, in figures 3.3, 3.4) at LEH, due to its sudden appearance following VLP-SP event 1. The area of the previous scattering model imaged by arrival L_1 at LEH corresponds to a large W-NW feature identified by both tomography and the full pseudo-reflection model [*Chaput et al.,* 2012] as feature A in Chapter 2, and very likely represents the location of a large shallow body of magma feeding the lava lake. Furthermore, the sudden visibility of this feature to station LEH suggests that there was deformation to the boundaries of this features during VLP-SP event 1, which enabled a specular reflection raypath from LEH to occur. Station CON features a persistent arrival at $\sim$1.5 seconds, denoted C_1 which locates in the same general area, but does not appear or disappear though the amplitude does fluctuate somewhat. CON does however present an intermittent feature, denoted C_2, which is most strongly affected by changes in VLP-SP timing, appearing after VLP-SP event 1, disappearing after event 3, and re-appearing after event 4. We also back-propagate this arrival, which points to a deeper, centralized feature identified in Chapter 2 as feature C, which is the most strongly scattering body in the volcano in the full model, and likely corresponds to a secondary body of magma. Given the lack of a singular location affected by temporal change, it would appear as though structural changes causing variations in the VLP-SP timing have a systemic character, rather than a single small variation in conduit geometry. Figure 3.5 displays several mechanisms by which small changes in

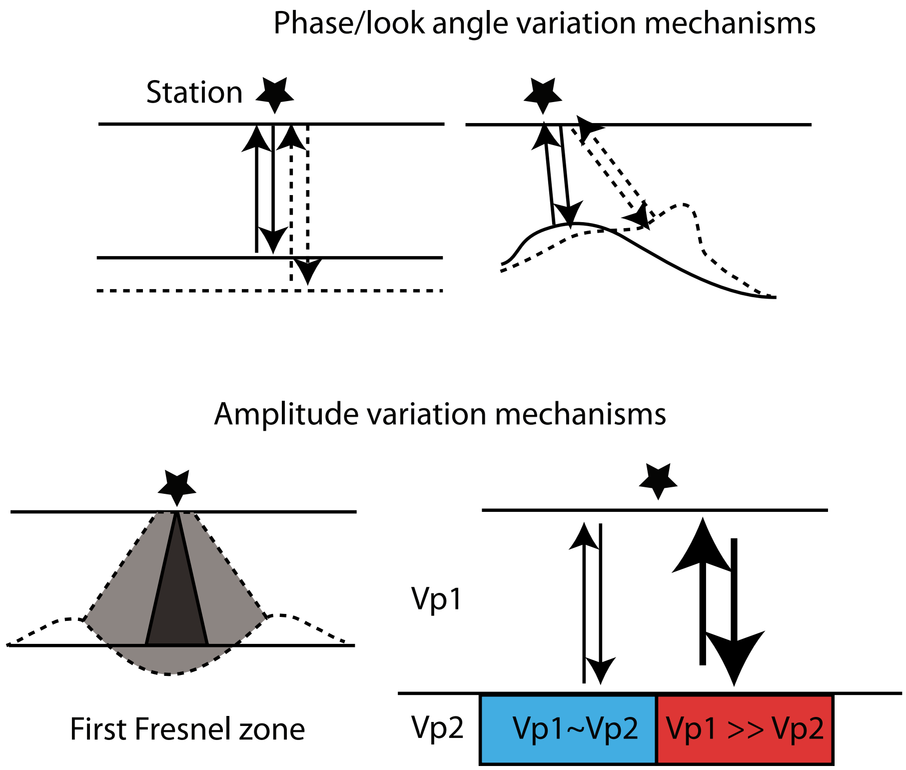

Figure 3.5: Mechanisms for Green's function variation. A small change in the curvature of the specular reflector may not necessarily change the phase, but can change the amplitude due to a modification of the first Fresnel zone (shaded areas). A similar change in amplitude can also be generated by simply modifying the velocity contrast between both sides of the reflector. On the other hand, phase changes can be more complex than a simple moving boundary, as we must also keep track of the particle motions to ensure that the look angle of the ray is not also substantially changing.

structural geometry or boundary contrast may drastically affect a given specular reflection. A very dense permanent deployment would not only allow for the location of structural change, but also the mechanism, as small spatial changes in the station locations would have a large effect on the phase and amplitude of a given arrival.

It is impossible to give an estimate on the spatial limits of structural change using MEVO, as the scattering coverage for so few stations is insufficient, but this important proof of concept may be applied for future larger scale deployments over active media. Conceivably, once a full scattering model is determined by using a temporary dense deployment, a much smaller permanent deployment may be used to locate areas of structural change within a predetermined model.

3.3 Conclusions

We have expanded the methodology developed in Chapter 2 to include the long running MEVO permanent array in an effort to document potential structural changes at Erebus volcano. Large excursions in the Green's function estimates are shown to be corroborated by similar changes in the VLP-SP timing lags, thus pointing to periods of rapid structural evolution as a mechanism for changes in eruptive character. The evidence pointing to the fading and re-emergence of the deeper scattering feature C_2 (feature C in Chapter 2) with respect to station CON, as well as the emergence of the L_1 at LEH, suggest that changes in eruptive character may occasionally reflect a wider range of structural shifts in the volcanic edifice rather than a localized small variation in upper conduit tilt affecting post eruption reload [*Knox*, 2012, *Rowe et al.*, 1998]. For Erebus volcano, the scattering image has been shown to converge fairly rapidly (i.e. within 20 stations used) towards the full dense network resolved image. Consequently, the use of a handful of stations is insufficient to resolve a fully temporally varying volume, but we are able to nonetheless identify structural variations originating from two of the major features identified in the scattering and tomography models of Erebus. The advantage of this methodology lies therefore in its ability to pinpoint in 3D with high resolution locations undergoing structural change, and presents an opportunity for passive 4D pseudo-reflection monitoring of actively deforming systems, should there exist an abundance of local natural sources or persistently generated anthropogenic ones. The advantage of pseudo-reflection over tomography-based ambient noise imaging techniques resides in the much higher resolution in the spatial location of features displaying temporal variability, and the fact that this resolution is purely dependent on the frequency content of the coda. For local signals exhibiting peak frequencies in the 1-5 Hz range, feature resolution is on the order of tens to hundreds of meters, whereas ambient noise tomography typically yields feature resolution on the order of kilometers. The proposed expansion of the MEVO network will feature up to 20 permanent broadband stations that may be used to test this idea over the coming years, and could provide much insight into the real-time ”structural breathing” of the volcano as well as present the scientific community with a powerful, flexible tool for studying highly active media.

CHAPTER 4

CRUSTAL THICKNESS IN WEST ANTARCTICA AND IMPLICATIONS FOR TECTONIC AND CRYOSPHERIC PROCESSES

4.1 Introduction

Efforts aiming to identify, characterize, and understand the details of cryospheric, tectonic, and geophyscial processes in Antartica have expanded and advanced tremendously during the past decade as the continent's central importance to Earth's climate system and the dynamic aspects of that system have become increasingly apparent. Many key constraints are derived from seismological data and interpretations. Surface wave studies have broadly revealed that East Antarctica presents fast upper mantle velocities and a thick crust ranging from 35-45 km [*Bentley,* 1973, *Studinger et al.,* 2006, *Lawrence et al.,* 2006], on par with other cratons globally. The Transantarctic Mountain range (TAM) has been identified as broadly delineating one of Earth's most significant intracontinental tectonic transitions, being generally located between the fast upper mantle and thick crust within the EAC and the slower upper mantle and thin crust of the West Antarctic Rift System (WARS) [*Sieminski et al.,* 2003, *Danesi and Morelli,* 2001, *Ritzwoller et al.,* 2001, *Morelli and Danesi,* 2004].

In association with gravity studies of the TAM, prior seismic studies have revealed crustal thickness of as low as 20±2 km for the WARS [*Bannister et al.,* 2000].

The TAMSEIS experiment [*Watson et al.,* 2006] was a pioneering effort to install a relatively dense and large coordinated network of broadband seismographs across part of the Antarctica continent. It crossed the TAM boundary into the EAC to characterize the extent of the WARS/EAC transition, revealing low lithospheric and upper mantle velocity structure beneath Ross Island and extending 50-100 km beneath the TAM, although the experiment did not have the lateral extension necessary to study the variation of this anomaly along the strike of this transition. Joint receiver function, phase velocity and gravity analysis using TAMSEIS data [*Lawrence et al.,* 2006] have yielded crustal estimates of 20 km below Ross Island to a maximum of 40 km below the crest of the TAM, with EAC crustal thicknesses averaging $\sim$35 km. Also identified in this study was the presence of a $\sim$5 km thick buoyant crustal root to the TAM, which is insufficient to explain present TAM uplift, thus indicating that TAM topography in this region is supported by deeper mantle.

The evolution of the West Antarctic Ice Sheet (WAIS), and its role in and response to, global climate change are of considerable importance to the global climate system and sea level. Several studies to date have mapped out sections of the WAIS crustal and upper mantle structures [*Lawrence et al.,* 2006, *Winberry,* 2004, *Anandakrishnan and Winberry,* 2004, *Ritzwoller et al.,* 2001] but these have focused on geographically limited targets such as the TAM, necessitating a larger effort to produce a more synoptic view. The extensional zone corresponding to the WARS is associated with low sub-ice elevations, thinned crust, likely lowered viscosity, and high heat flow, all of which affect WAIS dynamics. To better understand these issues, the POLENET project, funded as part of the International Polar Year (IPY) deployed a seismographic network of unprecedented extent for source, tomographic, and receiver function studies, (e.g., [*Wilson et al.*, 2005, *Langston*, 1979]) in West Antarctica.

P-receiver function (PRF) and S-receiver function (SRF) studies have been performed for limited portions of the East Antarctic craton and the TAM through TAMSEIS [*Lawrence et al.*, 2006, *Hansen et al.*, 2009] and the Gamburtsev-region AGAP projects [*Hansen et al.*, 2011]. However, receiver functions acquired over complex low velocity shallow structures, such as ice sheets and sedimentary basins, can be very difficult to interpret via traditional means (i.e. migration and CCP stacking) due to the prevalence of strong P-wave multiples that mask P-S Moho and other key seismic phase conversions. Specifically, the presence of a thick ice sheet may generate P-multiples that mask deeper P-S conversions, confusing efforts to recover crust and mantle features. There have been some efforts related to deconvolving the ice sheet response from the PRF signal [*Cho*, 2011], but stability issues limit the capability of recovering Moho conversion phases. We present a solution to this problem where PRFs are concerned, via implemeting iteratively forward PRF modeling and using the result as prior information for a Bayesian inversion. This method was partially inspired by a purely forward modeling approach applied to the ANUBIS array [*Winberry*, 2004], where PRFs in West Antarctica revealed relatively thin crust under the WAIS and the hint of thinner than expected crust under the Marie Byrd Land volcanic province. Here, we present PRF results for the entire POLENET array in West Antarctica, and combine them with concurrent efforts in continent-scale ambient noise surface wave tomography to generate a new crustal map of West Antarctica.

The following results and implications are largely taken from the manuscript entitled: "Crustal Thickness in West Antarctica and Implications for Tectonic and Cryospheric Processes".

4.2 Receiver function approach

Fundamentally, P-wave Receiver Functions (PRF) are time series computed from 3 component seismograms that aim to isolate P-S converted arrivals from the remainder of the scattered waveform. More specifically, it assumes that any S-wave arrivals after the onset of the direct P-wave from a distant event, but before the arrival of the direct S-wave, are generated by P-S conversions from velocity discontinuities at depth. This is accomplished by first picking a given teleseismic event, and rotating the data into the source-station backazimuth direction. to isolate the converted S wave arrivals from the P-wave multiples, we then deconvolve the vertical component, which contains mainly P-wave energy, from the radial component of the seismogram. We may do this largely thanks to the earth's largely linear behavior in the propagation of seismic waves. In the ideal case, the deconvolution may be expressed in the frequency domain as:

$$P_r(\omega) = \frac{D_r(\omega)}{D_v(\omega)} \tag{4.1}$$

Where P_r is the radial receiver function, and D_r and D_v are the radial and vertical components of the seismogram after rotation. The assumption here, is that very near vertically incoming P-waves from teleseismic events behave as impulsive wavefronts convolved with the medium's impulse response. Typically, however, the deconvolution can not be described as a simple spectral division due to the presence of holes in the vertical component's frequency spectrum which get amplified in the division. As such, methods of regularization are typically used to ”fill the holes” in the case water level regularization, or by other methods of estimating spectrum. Typically, the level of regularization must be chosen by trial and error. In this study we use a multi-taper spectral estimation technique to facilitate a stable deconvolution without having to compute regularization parameters. The use of Slepian sequence tapers in spectral analysis is well documented, and has recently been extended to receiver function applications with attractive prospects [*Park and Levin*, 2000] due to the low amount of spectral leaking. As such, the radial receiver function can be described as:

$$P_r(\omega) = \frac{\sum_{k=1}^{K}(Y_Z^k(\omega))^* Y_R^k(k)}{S_0(\omega) + \sum_{k=1}^{K}(Y_Z^k(\omega))^* Y_Z^k(k)} \tag{4.2}$$

Here, the $Y_{R,Z}^k(\omega)$ are the k-th Slepian-tapered Fourier transforms of D_r and D_v, $S_0(\omega)$ is the pre-signal noise estimate estimated from D_v, and $*$ represents conjugation. The original algorithm presented a flaw through which later temporal information was lost in the deconvolution. An extended time fix for this problem was suggested by [*Helffrich*, 2006], and consists of computing a series of overlapping time windows, with each window containing its own multitaper estimate, and the results are then summed in the final PRF estimate.

4.3 Estimation of inversion priors

We compute P-receiver functions for the complete POLENET data set, encompassing the backbone station deployment (2008-2012) and the temporary transect deployment (2010-2012). Figure 4.1 shows a map of the studied area

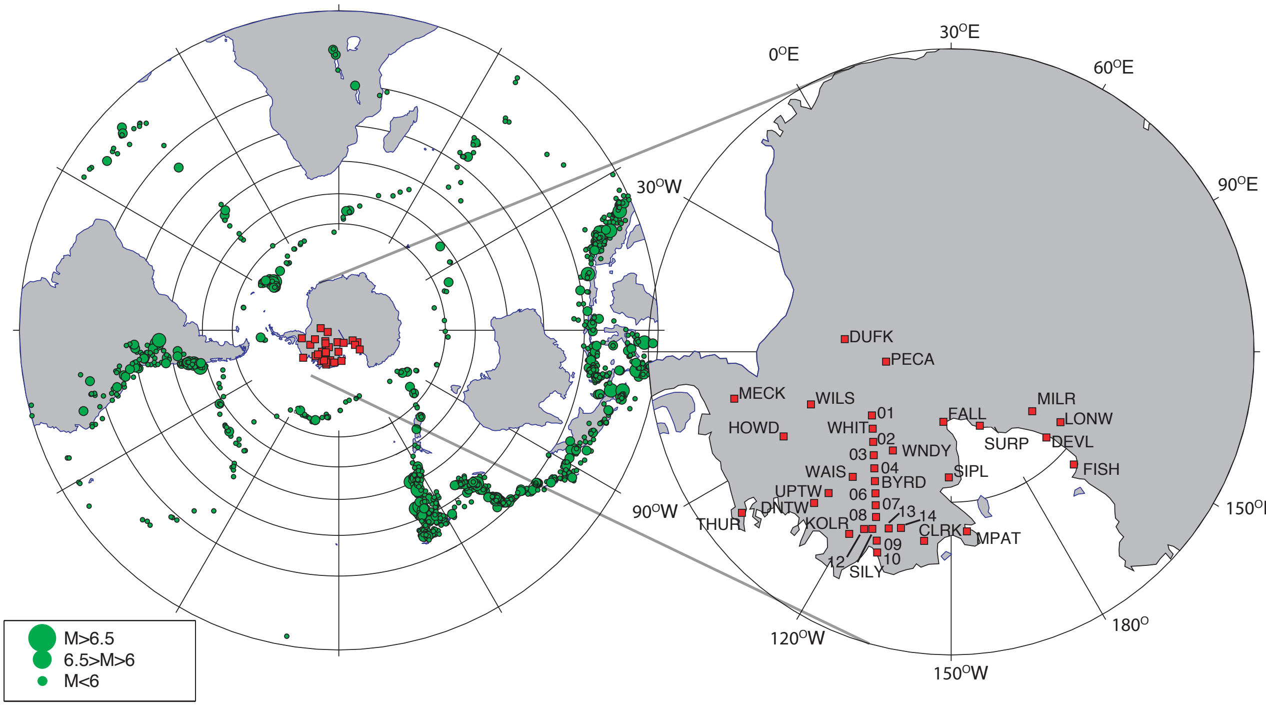

Figure 4.1: POLENET seismographic deployment and teleseismic source distribution, 11/2008-1/2012. The POLENET transect (ST01-ST14), was deployed for 2 years, and was embedded among a network of longer-term backbone stations. There is a notable azimuthal preference of teleseisms driven by source clusters in South America and the southwestern Pacific.

showing all POLENET stations and the event azimuth distribution used in the PRF calculations.

Roughly 1300 events from 30 to 90 degrees were used in the PRF study, although transect stations recorded roughly half that number due to the shorter deployment period. We compute PRFs by applying an Extended Time Multi-Taper deconvolution approach (ETMT) [*Helffrich*, 2006, *Park and Levin*, 2000], and subsequently apply $f-k$ domain filtering [*Wilson and Aster*, 2005] to reduce noise in the PRF gathers (e.g. Figure 4.2) corresponding to higher moveout curves than are predicted by the 660 km P-S mantle discontinuity.

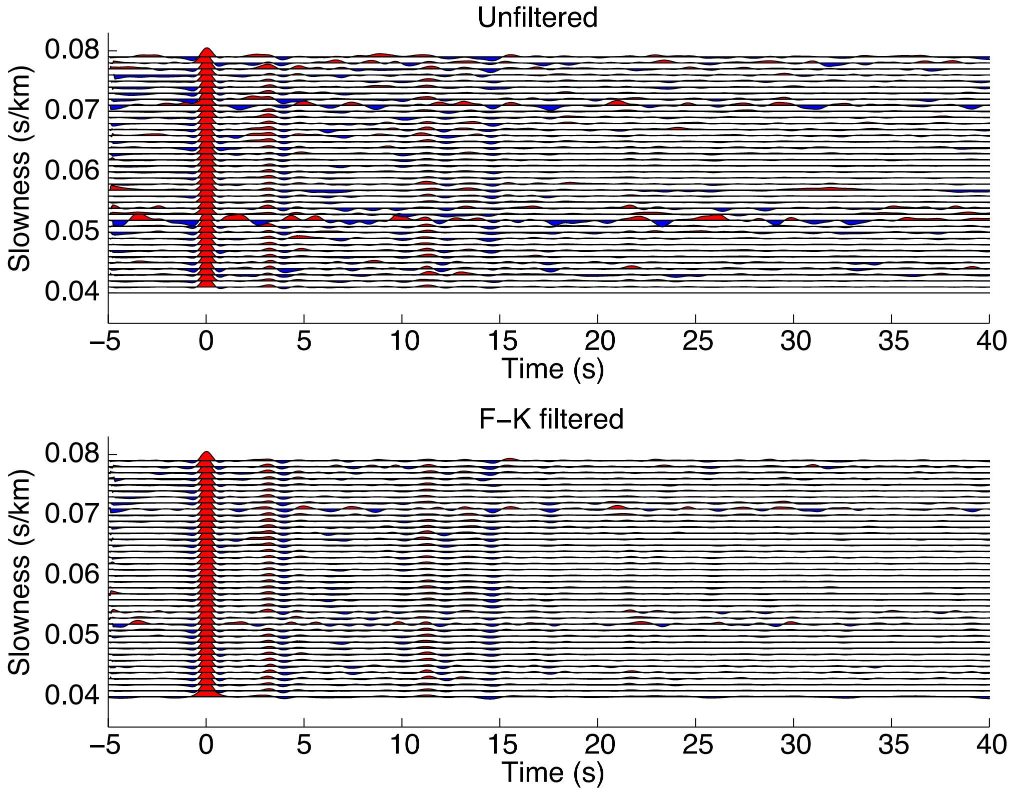

Figure 4.2: Representative PRF gather from station MPAT arranged with slowness, showing the effect of $f - k$ domain filtering [*Wilson and Aster*, 2005]. These gathers have been slowness corrected for an PPPS conversion from a Moho at 30 km.

Because P-wave multiples generated by the ice sheet dramatically distort or obscure P-S conversions from structure of interest all the way to the upper mantle, conventional crustal migration avenues are not useful. Figure 4.3 shows examples of forward modeled PRFs for media featuring ice sheets and shallow sedimentary basins, as are inferred to exist under much of West Antarctica [*Winberry*, 2004, *Karner et al.*, 2005, *Bell et al.*, 1998]. Where ice thickness estimates are accurate, the mismatch between the early portion of the synthetic and real PRFs are potentially explained by the presence of low velocity sediments underlying the ice sheet, though there are other possible causes, as described below.

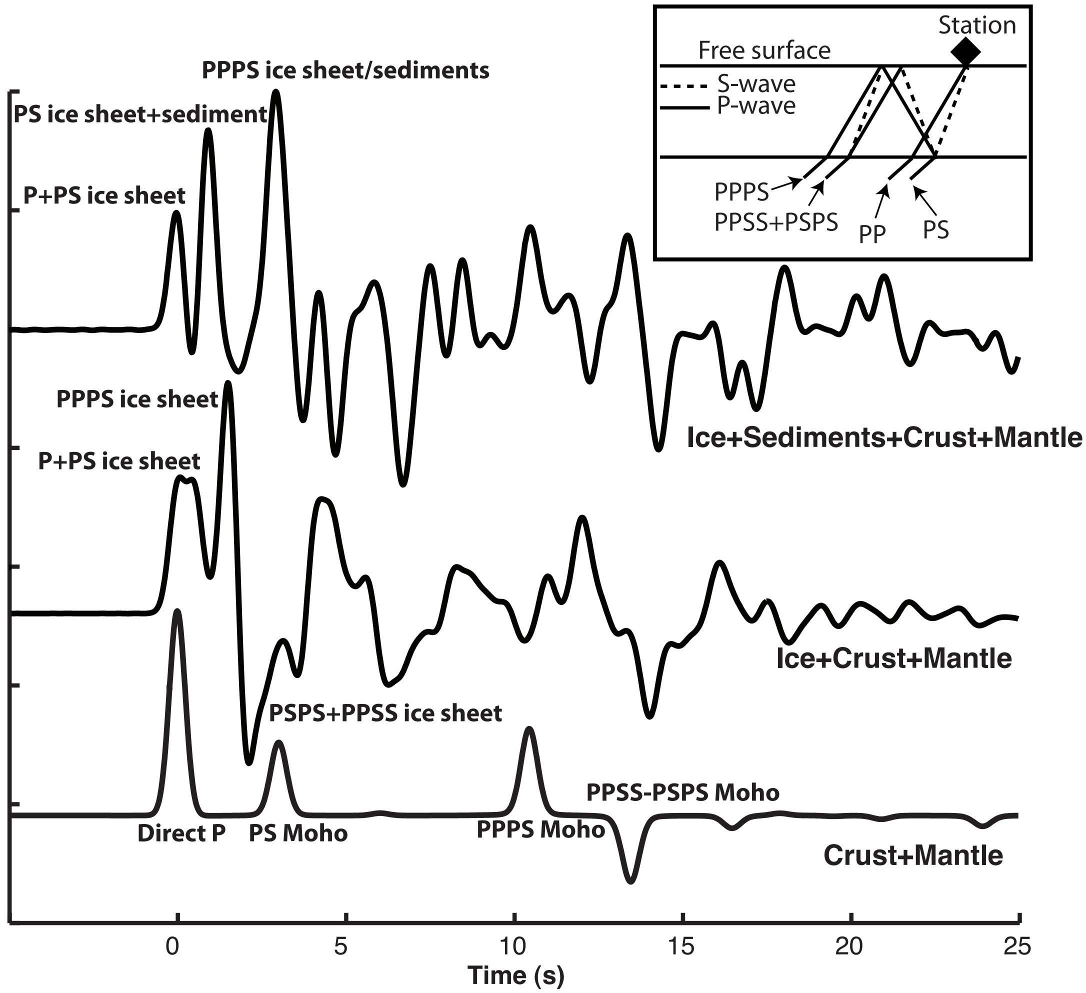

Figure 4.3: Synthetic forward modeled PRF waveforms showing characteristic ice sheet and sedimentary basin features. Due to the large seismic impedance contrast between the ice sheet and underlying crustal structure, and to low ice sheet attenuation, ice sheet reverberations can completely obscure Moho associated phases. The displayed models feature a 2.5 km ice sheet, a 1 km sedimentary basin with a Vp of 0.9 km/s, a 30 km crust, and an incident wave with 0.05 slowness.

We expanded upon the approach of [*Winberry*, 2004] to allow for the correct recovery of crustal thickness information from complicated receiver functions recorded on ice sheets. To do this, we forward modeled PRFs and built a crustal model from the top-down, starting by correctly fitting ice sheets (with valuable initial estimates provided by BEDMAP [*Lythe et al.*, 2000]) and possible sedimentary basins with varying velocities, and then fit a crustal structure while trying to maximize the cross-correlation maximum between the synthetic and true PRF. Given the paucity of ice thickness measurements throughout the majority of West Antarctica, we evaluated the forward model's ability to recover ice sheet parameters and compare them to BEDMAP and drilling estimates, where available. Figure 4.4 demonstrates recovered ice thicknesses versus BEDMAP constraints.

Note that where ice sheet thicknesses are very well constrained, there is good agreement between both measurements. There does tend to be substantial variation for stations on the WAIS and the MBL however, as the nearest BEDMAP constraints can be in excess of 500 km away (see Table 1). Furthermore, for most ice stations, it is possible to fit a fairly obvious bulk crustal model to the PRFs via a grid search forward modelling process. Figure 4.5a-b show examples of the forward modeling approach, where we choose to test for a variety of possible parameters, including sediment thickness, sediment velocity, crustal thickness, and crustal V_P/V_S. Given the tradeoff between ice thickness and sediment thickness in the PRF fit, stations where the ice sheet is not well constrained by other means (i.e. drilling) may have a variety of solutions with nearly equal waveform correlation indices.

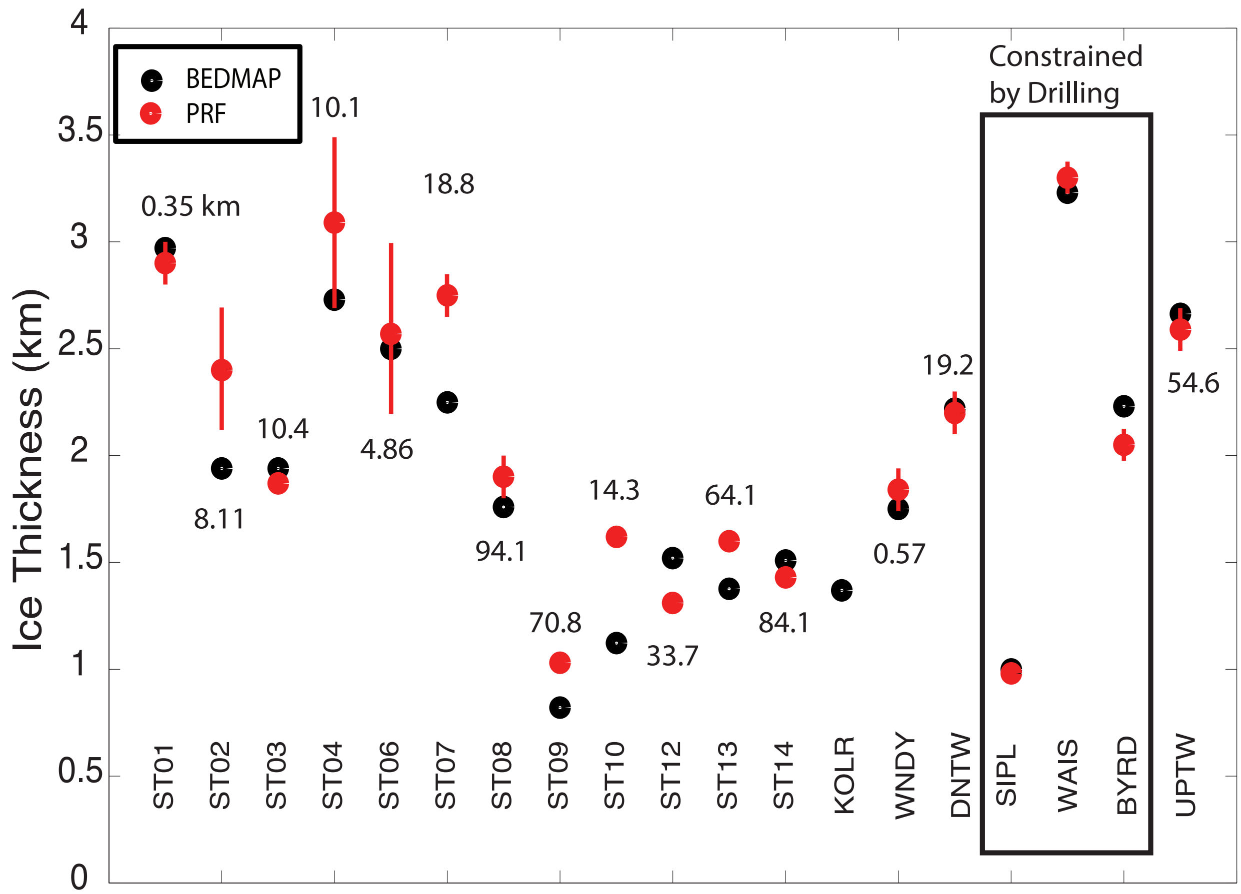

Figure 4.4: Ice thicknesses recovered via forward modeling versus ice thickness constraints compared to BEDMAP estimates for all ice-sited POLENET stations. Red error bars indicate 95% confidence intervals. Thicknesses that have been directly determined by essentially co-sited drilling (SIPL, WAIS, and BYRD) are highlighted by the black box. Distance (km) to the nearest BEDMAP measurement node is indicated for each station in Table 1.

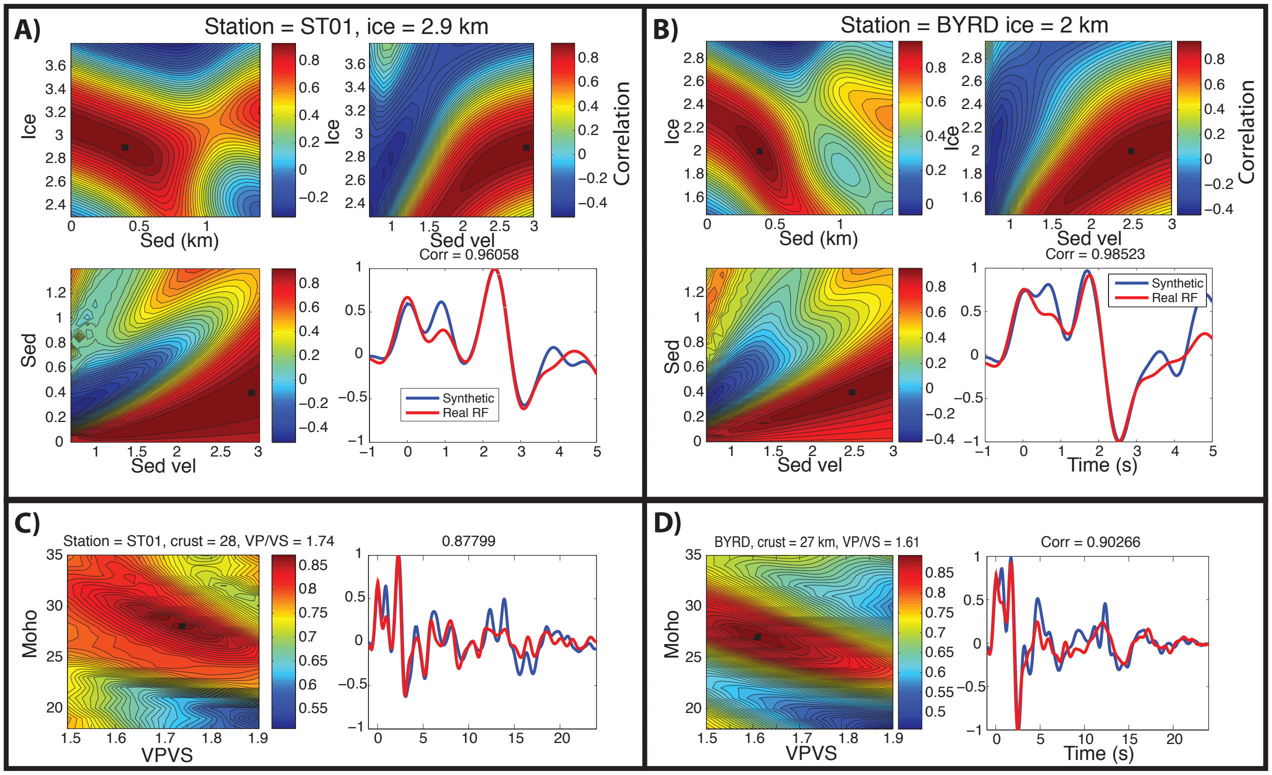

Figure 4.5: Forward modeled receiver functions. A-B) Examples of the earliest portion of forward modeled PRFs with respect to real data. In most cases, the ice sheet thickness can be well recovered along with an apparent sediment layer. Black squares indicate best fit solutions. C-D) Examples of forward modeled receiver functions for ice/sediment/crust components. As a general rule, if the early portion of the PRF can be fairly accurately modeled, then the later portion can be well fit through the simple addition of a crust. We may then use these roughly modeled receiver functions as priors for an inversion scheme that will not allow for extravagant ice thickness models.

We allow for the V_p for the sedimentary basins to range from 0.5 to 4 km/s, while setting the sedimentary basin Poisson's ratio to 0.25, as in [*Winberry,* 2004], to approximate Ross Sea sediment parameters. This particular assumption could be inappropriate given the unknown nature of subglacial sediments in West Antarctica, but it was necessary given the increasingly prohibitive computational costs of forward modeling a multitude of parameters. Ice velocity was fixed at 3.87 km/s, following studies of P-wave velocity in ice of various temperatures [*Kohnen,* 1974] with a Poisson's ratio of 0.33. Correlation maxima were found to be as high as 0.98, and only a small number of stations proved to be ultimately difficult to successfully model.

After an initial fit is obtained for the shallow structure, we append an infinite crust to the model, setting crustal V_p to a nominal value of 6.3 km/s while letting the V_p/V_s ratio vary from 1.5 to 1.9, thus giving us a fit for the first 25 s of the computed PRF. Fitting further layers is possible, but becomes increasingly difficult if complex crustal or upper mantle structure exists. Where PPPS or PPSS multiples are visible, synthetic fits tend to be much more accurate, though over all the forward modeling averages a correlation index of ~ 0.85 with respect to the actual data. Figure 4.5c-d shows examples of the first 20 s of ideally fit receiver functions, allowing for correlation indices of up to 0.9, along with ellipses showing the best parameter fits. Following this forward modeling approach, we use the resulting models as a prior model to further invert the PRFs using a Bayesian inversion, as described below.

Complications were observed at a few stations in the POLENET transect (ST04, ST06, ST09) in the delay of the P-S conversion from the base of the ice sheet relative to the later PPPS from within the ice sheet. Possible explanations include seismic anisotropy in the ice [*Bentley*, 1971], or variable basal inclinations that can confuse the correct fitting of the earliest portions of the PRFs via simple synthetic models. Basal dip could also produce substantial timing differences between the predicted ice sheet multiples for a given thickness and the computed PRFs. Failure to correctly model the earliest portion of the PRFs can thus result in poor crustal fits in the subsequent gridsearch, and manual fitting with more substantial uncertainties must be applied to estimate a usable prior. A poorly modeled ice sheet may further cause later inversion steps to attempt to compensate for this problem by creating highly improbable models with very large alternating low/high velocity zones. Figure 4.6 shows BEDMAP basal elevations along with the local integrated gradient of BEDMAP values for a 30 by 30 km square around each station, offering estimates of where one might find high basal dip or other complexities in basal topography, although the resolution of BEDMAP is nonuniform and many areas in West Antarctica are very sparsely sampled in the underlying BEDMAP constraints.

Figure 4.7 displays examples of poorly fitted early portions of PRFs, and the impact on multiples for varying degrees of basal dip. An ice sheet presenting a basal dip which decreases the apparent incidence angle of the ray with respect to the ice sheet will result in a slightly delayed PS conversion from the ice sheet and a much earlier PPPS multiple, thus potentially accounting for the mismatch in the modeled ice sheet, and thus masquerading as a sediment layer.

We can explore for consistent data features assocaited with anisotropy or basal dip at complex stations by examining PRF gathers arranged by event

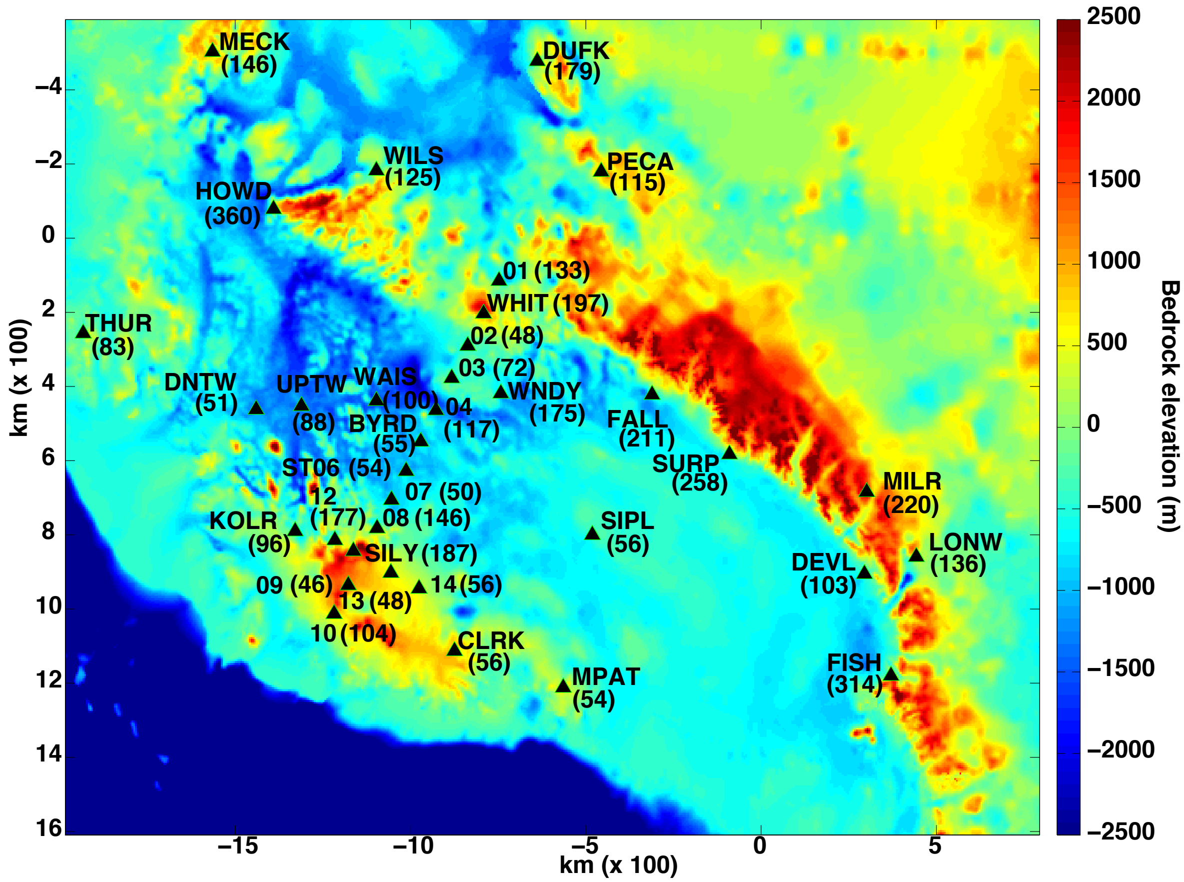

Figure 4.6: Map of basal elevations across West Antarctica from BEDMAP [*Lythe et al.*, 2000]. Station specific basal gradients averaged over a 30 x 30 km square region centered on each station is indicated in parentheses; stations with large values might feature particularly complicated or azimuth dependent PRFs due to complex ice bed topography. BEDMAP grid measurements are particularly lacking in the northern portion of the WAIS transect and in Marie Byrd Land, resulting in a potentially smooth bias to topographic gradients estimates in these areas. The white triangles represent other stations from past deployments included in the crustal map in Figure 4.10.

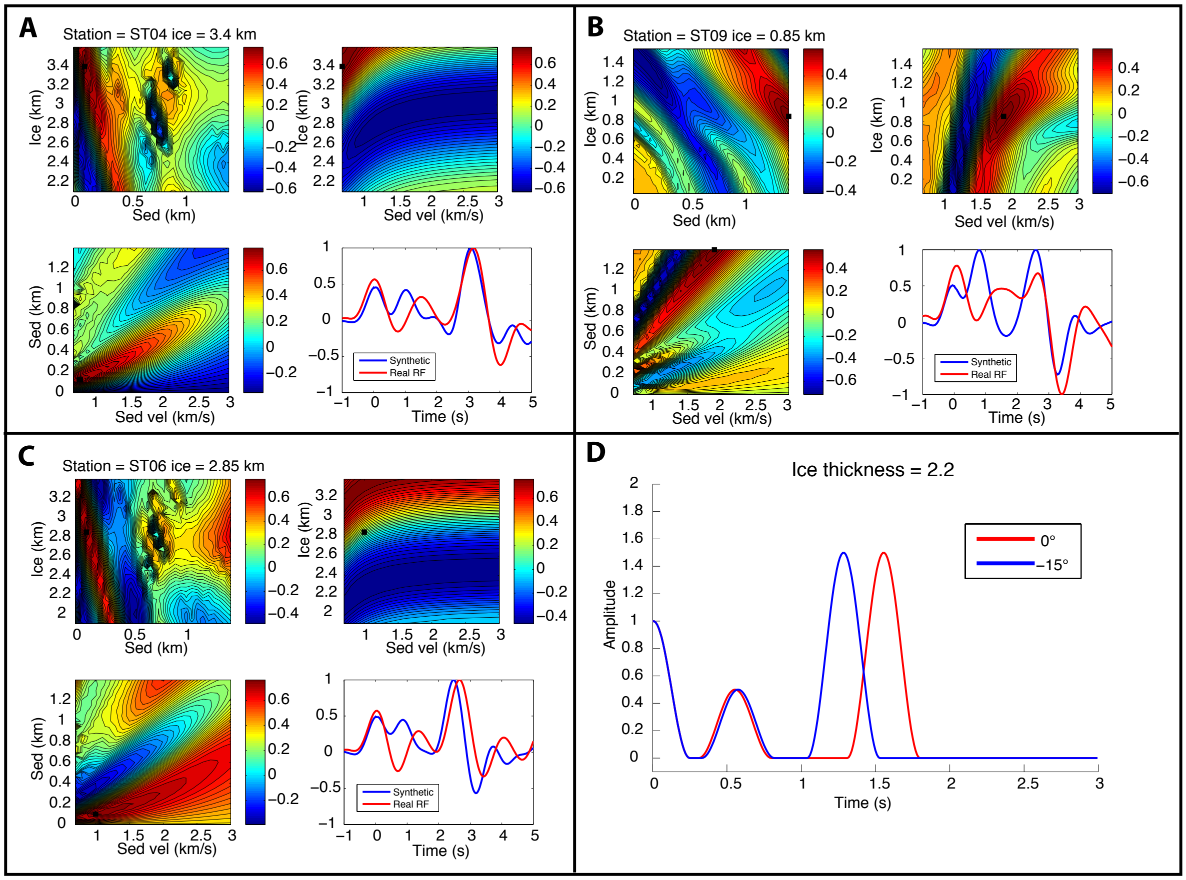

Figure 4.7: (A-C) Example of poorly fitted shallow layers for problematic stations. (D) Demonstration of the effect of a dipping ice sheet on the modeling of early multiples for an ice sheet with a 15 degree dip that reduces the apparent incidence angle of the ray. A slight dip of the ice sheet may in fact masquerade itself as a sedimentary basin given its substantial effect of the later multiple in the early portion of the signal. Note however that the earliest PS conversion from the base of the ice sheet will be contracted rather than delayed in the event of a later PPPS multiple from a dipping ice, thus making it possible to distinguish between dipping layers and shallow sediments for future studies.

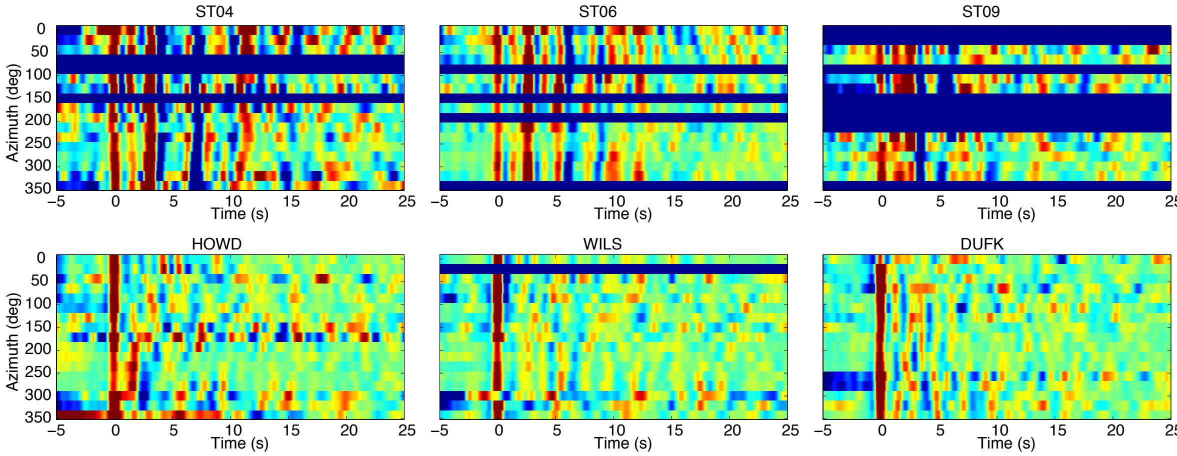

Figure 4.8: Azimuth-binned PRFs for stations ST04, ST06, ST09, HOWD, DUFK and WILS, showing substantial variability with azimuth. ST06 is particularly difficult to accurately forward model for an ice station, whereas HOWD and DUFK show a high degree of azimuthal dependance with respect to shallow structure due to their locations on the flanks of nunatak structures. These stations have higher uncertainties on crustal estimates.

backazimuth. Figure 4.8 shows azimuthally binned gathers for which a simple ice/sediment/crust model was insufficient, or where the evident crustal complexity confused crustal estimates. The generalized sub-ice gradient metric calculated from BEDMAP (Figure 4.6) suggests that ST04 has the highest potential for highly variable basal topography, but the metric is subject to the unavoidable spatial aliasing of the various BEDMAP data sets. An azimuthal moveout can be observed in the PS conversion from the base of the icesheet for these stations, though the effect on the PPPS multiple is far less than predicted by our simple basal dip model. Later multiples show substantial azimuthal dependance, suggesting some degree of geometrical complexity to the ice sheet. Despite the mismatch in the early multiples however, we may still model the later portion of the RFs fairly well in the inversion step, giving us a plausible crustal estimate for all ice stations.

Although we do not implement a methodology here to handle dipping layer PRFs, future studies utilizing PRFs over ice sheets could better account for basal topography to more accurately model waveforms at some stations. We note that a small basal dip can account for much of the delay in the ice sheet PPPS, and that there is a tradeoff with inferred low velocity sub-ice (e.g. sedimentary basin) structure, although the effect on the PS phase is opposite. One must therefore be cautious when simply fitting the PPPS from the icesheet to infer the presence of a sedimentary basin if the early waveform fit is poor, even if the ice thickness is well constrained. Where the early fit is very good, however, a sedimentary basin is more likely to be resolvable, and we can ultimately use this information to build a more robust prior for subsequent inversion, as described below.

4.4 Markov Chain Monte Carlo inversion

The backbone portion of the POLENET deployment is generally composed of stations deployed on nunataks, mountain crests, and occasional coastal locations. Consequently (and as suggested by the bed gradient metrics of Figure 4.6) many of these stations have large local asymmetric subaerial or sub-ice topographic variations that produce strong azimuthal variations and generally complex crustal PRFs. In such cases, evaluating the Moho depth and V_p/V_s ratio via multiple fitting, e.g., [*Zhu and Kanamori,* 2000], typically does not yield acceptable results.

Employing a more robust methodology, we invert both rock and ice station receiver functions via a Markov Chain Monte Carlo algorithm (MCMC) [*Aster et al.,* 2012, *Bodin et al.,* 2012]. Such methods offer the advantages of a linear increase in computation time with parameter numbers, and only the forward problem must be solved. We assume a Poisson's ratio of 0.27 for the crust, and allow the velocity of the layers to vary freely within limits set by station specific priors. We fix the elastic parameters of the first layer (in the case of ice stations) and only let the thickness vary, as unrealistic models for the ice sheet will otherwise be found given the tradeoff between thickness and velocity in generating the ice sheet signature. Where there are definite maxima in the forward modeled priors, we also introduce sediments, though the model is allowed to vary out of it.

One of the primary difficulties with inverting waveforms generated from ice stations, is our inherent inability to perfectly fit the amplitudes of the ice multiples. Given the large amplitudes of these multiples, there is a substantial misfit gain to be made by introducing a plethora of unrealistic alternating low/high velocity jumps. To reduce the prevalence of such model structure, we the inversion using Total Variation (TV) e.g., [*Aster et al.,* 2012] , which favors models featuring minimal total derivatives, thus penalizing large negative velocity jumps. Given the boundaries set by the prior models, large positive jumps are largely unaffected, allowing for the Moho to be very well resolved. The TV regularization model seminorm is

$$TV(\mathbf{m}) = \sum_{i=1}^{n-1} |m_{i+1} - m_i| = \|\mathbf{Lm}\|_1 \tag{4.3}$$

where $\mathbf{m}$ is the current model, $\mathbf{L}$ is the first-order roughening matrix, and the subscript 1 indicates the 1-norm [*Aster et al.,* 2012]. The objective function calculated at every forward model iteration then becomes a weighted sum of the misfit and the TV regularization seminorm

$$M_i = \|\mathbf{Gm} - \mathbf{d}\|_2^2 + \alpha\|\mathbf{Lm}\|_1 \tag{4.4}$$

where, α is an empirically determined weighting factor used to favor defined velocity jumps at the cost of data fit. For ice stations, we use an experimentally determined α of 0.25, while for rock stations we use 0.02.

The MCMC algorithm requires the definition of a probability-based acceptance relation. To sufficiently sample the posterior distribution we use an associated proposal function that allows the velocity and layer thicknesses to take steps of up to 1 km/s and 1 km respectively, using realizations of a uniform random variable, which results in an acceptance rate of 0.3-0.5 for new models. Figure 4.9 shows example inversion results for several representative rock and ice stations (see Supplement for all results). Stations associated with apparently simple crustal structures, which are also interpretable by multiple fitting [*Zhu and Kanamori*, 2000] (e.g., MPAT, WHIT), show very good agreement with the MCMC results, thus bolstering our confidence in results at other stations. Inversions for ice stations with structures that are well-fit during the forward modeling steps do not vary substantially from the priors, as expected. Uncertainties on Moho determinations were estimated using the transition depth range from the crustal velocity probability peak to the mantle velocity probability peak. Given the very tight distributions generated by this particular approach, we choose to set the uncertainty as the range over which the crustal probability begins to decay from its pre-Moho maximum to where the post-Moho peak reaches a local maximum in mantle velocities.

For the aforementioned stations which present particularly complex crustal structures and/or near-station subareal or sub-ice topography, it is difficult to umambiguously interpret Moho conversions. The most likely crustal thickness determinations (the maximum a posteriori models) for all stations and associated posteriori-derived uncertainties are noted in Table 1. Where possible, we fit a 10-layer model with prior layer depths determined by the initial forward model step. We allow the depths to vary freely, and the velocities of the layers to within ± 0.3 km/s of the prior, based on IASPEI 1991 [*Kennett,* 1991] crustal velocities. Where the 10-layer model cannot provide an adequate fit, we further examine 30-layer models that allow the velocities to vary more substantially. Problematic fits generally arise for stations featuring particularly strong azimuth dependance (Figure 4.8).

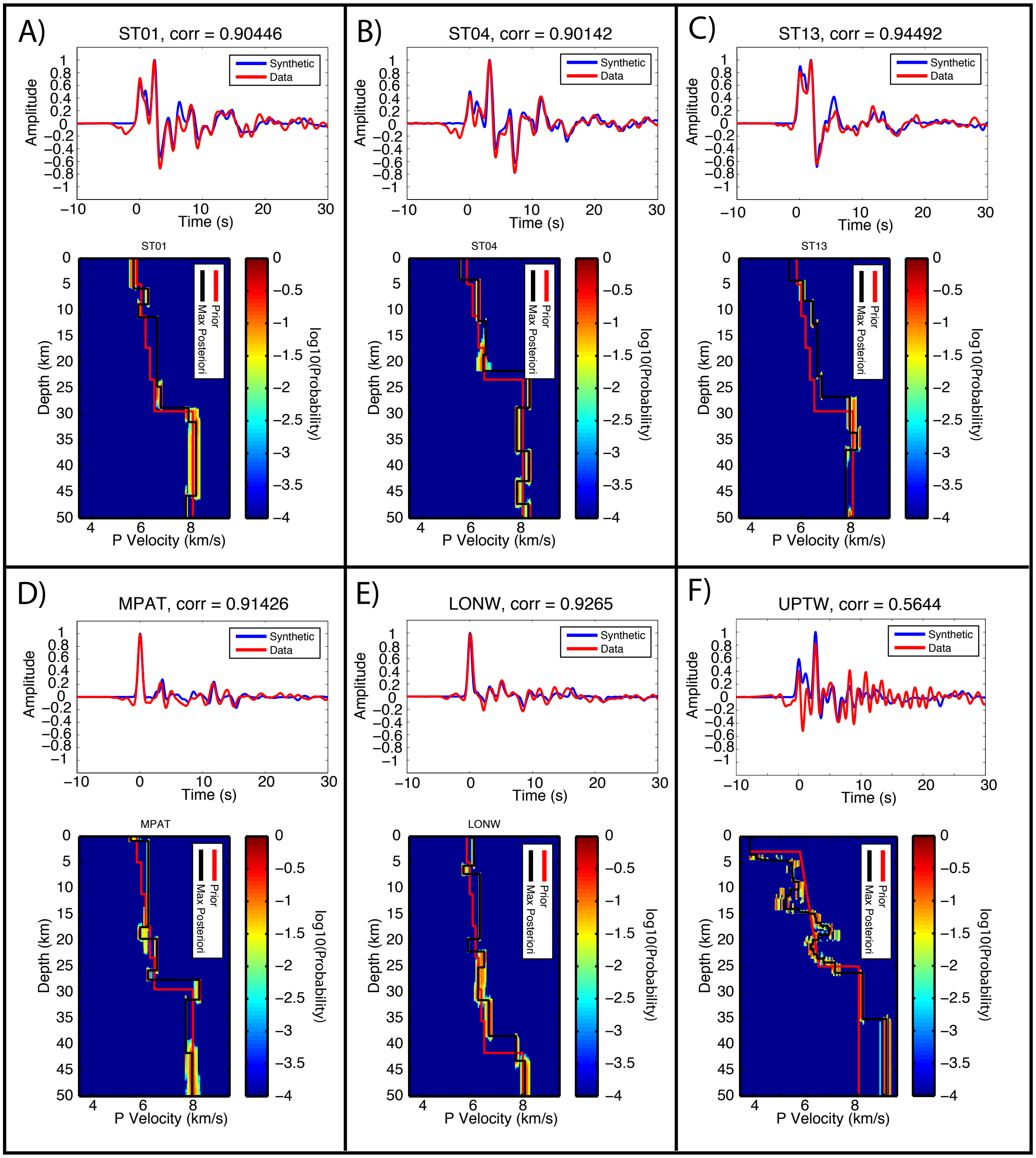
A)
ST01, corr = 0.90446
B)
ST04, corr = 0.90142
C)
ST13, corr = 0.94492
D)
MPAT, corr = 0.91426
E)
LONW, corr = 0.9265
F)
UPTW, corr = 0.5644
Synthetic
Data
Amplitude
Time (s)
Prior
Max Posteriori
Depth (km)
P Velocity (km/s)
log10(Probability)

Figure 4.9: Results from the MCMC inversion. A-E) Examples of probability density plots after a burn-in of 5000 models generally display very tight distributions due to the maximum variability regularization and tight constraints from the prior. A-C are ice station, D, E are rock stations. Ice sheet parameters as determined by the forward model are absolutely constrained in the prior, so depth inversions here represent structure below the ice sheet, where depth = 0 is the base of the ice sheet. Where possible, we aim fit a simple model (10 layers, 0.5 km/s maximal deviation from iasp91 velocities, no limit on depth variation of layers) and avoid large negative velocity jumps in the resulting model. F) Example of a more complex model for station UPTW. Where waveform fits are insufficient given a simple model, we allow for more variability in the velocity variations and the number of depth parameters, and we allow the ice thickness to vary freely. Depth = 0 here is the free surface, and the inferred ice thickness must be subtracted from the Moho estimate for inversions of this type.

4.5 Crustal thickness in West Antarctica

Table 4.1 presents comprehensive results from the forward modeled and inverted PRF receiver functions for POLENET stations. Crustal thicknesses across the West Antarctic transect are generally thin, ranging from 21-28 km, with modest thickening into the Marie Byrd Land volcanic province up to 31 km, greater thickening under Mt Whitmore (WHIT), and much greater thickening into the Ellsworth Mountains (HOWD, WILS). A number of transect stations feature a forward modeled early best fit with relatively fast underlying sediments, suggesting a normal crustal gradient and a lack of basin structures. The central portion of the transect, notably in the region of ST04, ST06, and BYRD, does however display results suggesting several hundreds of meters of very low velocity sediments. This is not surprising given the pronounced subglacial topography underlying those stations, and previous studies of sedimentary basins in the area, but we are hesitant to conclusively attribute sedimentary basin thicknesses due to the aforementioned basal dip influence on early multiples, and the lack of accurate

Station	Lat	Lon	Elev. (km)	Ice (km)	Moho (km)	Error (km)	BEDMAP node distance (km)	Location
ST01	-83.2279	-98.7419	2.03	2.97	28.7	0.3	0.35	Ice cap
ST02	-82.0690	-109.1243	1.72	1.94	26.6	0.6	8.11	Ice cap
ST03	-81.4065	-113.1504	1.66	1.94	26.8	0.2	10.4	Ice cap
ST04	-80.7150	-116.5782	1.52	2.73	21.6	0.2	10.1	Ice cap
ST06	-79.3316	-121.8196	1.52	2.50	23	1.9	4.86	Ice cap
ST07	-78.6387	-123.7953	1.59	2.25	23.4	0.2	18.8	Ice cap
ST08	-77.9576	-125.5313	1.78	1.76	28.4	0.2	94.1	Ice cap
ST09	-76.5309	-128.4734	2.25	0.82	27.3	0.3	70.8	Ice cap
ST10	-75.8143	-129.7489	1.75	0.82	23.0	0.4	14.3	Ice cap
ST12	-76.8970	-123.8160	2.20	1.52	24.2	0.4	33.7	Ice cap
ST13	-77.5609	-130.5139	1.86	1.52	26.6	0.4	64.1	Ice cap
ST14	-77.8378	-134.0802	1.64	1.51	28.6	0.4	84.1	Ice cap
CLRK	-77.3231	-141.8485	1.04	0.00	30.3	0.2	33.8	Mt Clarke
KOLR	-76.1545	-120.7276	1.89	1.37	N/A	N/A	20.5	Kohler Glacier
WNDY	-82.3695	-119.4129	0.94	1.75	26.5	0.4	0.58	Windy
FALL	-85.3066	-143.6284	0.29	0.00	24.3	0.3	46.3	Fallone Nunatak
SILY	-77.1332	-125.9660	2.09	0.00	30.6	0.1	80.5	Mt Sidley
DNTW	-76.4571	-107.7804	1.04	3.23	23.6	0.2	19.2	Down Thwaits
WHIT	-82.6823	-104.3867	1.29	0.00	31.5	0.6	5.28	Mt Whitmore
MPAT	-78.0297	-155.0220	0.54	0.00	27.6	0.2	129.4	Mt Patterson
SIPL	-81.6405	-148.9555	0.65	1.03	27.0	2.0	3.10	Siple Dome
MECK	-75.2807	-72.1849	1.08	0.00	26.3	0.8	516.4	Merrick Mountains
HOWD	-77.5285	-86.7694	1.50	0.00	44.4	3.1	96.7	Howard Nunatak
WILS	-80.0396	-80.5587	0.69	0.00	41.0	1.1	195.5	Wilson Nunatak
DUFK	-82.8619	-53.2007	0.97	0.00	25.5	1.2	491.0	Dufek Massif
PECA	-85.6124	-68.5527	1.51	0.00	30.4	1.1	193.6	Pecora Escarpment
LONW	-81.3466	152.7350	1.55	0.00	38.3	0.5	793.1	Lone Wolf
MILR	-83.3063	156.2517	1.90	0.00	45.0	0.5	652.4	Miller Range
SURP	-84.7199	-171.2018	0.41	0.00	26.1	0.6	262.1	Cape Surprise
DEVL	-81.4757	161.9745	0.10	0.00	17.0	1.3	646.3	Devlin Island
FISH	-78.9276	162.5652	0.27	0.00	16.5	0.8	729.4	Fishtail Point
WAIS	-79.4181	-111.7776	1.80	3.23	23.2	0.2	17.7	WAIS divide
BYRD	-80.0168	-119.4730	1.52	2.23	25.3	0.3	0.14	BYRD camp
THUR	-72.5301	-97.5606	0.24	0.00	24.8	0.3	350.5	Thurston Island
UPTW	-77.5797	-109.0396	1.33	2.66	26.0	0.7	54.6	Upper Thwaits

Table 4.1: Crust and ice values for POLENET

measurements for ice sheet thickness in the area. Future studies involving variable dip forward modeling may help elucidate this issue. Stations ST04 and ST06 also feature particularly thin crustal measurements, which is likely in part due to the fact that they are situated over very deep basins in an extensional regime defined by the West Antarctic Rift System. We also see particularly thin crust on the rift side of the Trans-Antarctic Mountains with moho depths of as little as 17 km at stations DEVL and FISH, very near where a hypothesized mantle plume is responsible for volcanic activity at Mt Erebus. Figure 4.10 a shows a crustal map encompassing all available Antarctic stations, including a slice view of the West Antarctic transect portions of the deployment.

We smoothly perturbed a surface wave tomography model [*Sun et al.*, 2011] with crustal determinations from POLENET and previous experiments (AGAP, TAMSEIS, ANUBIS, GSN, others) to generate the most accurate crustal map of Antarctica to date. 4.10b shows slice views of the lines denoted A-A′ and B-B′ in

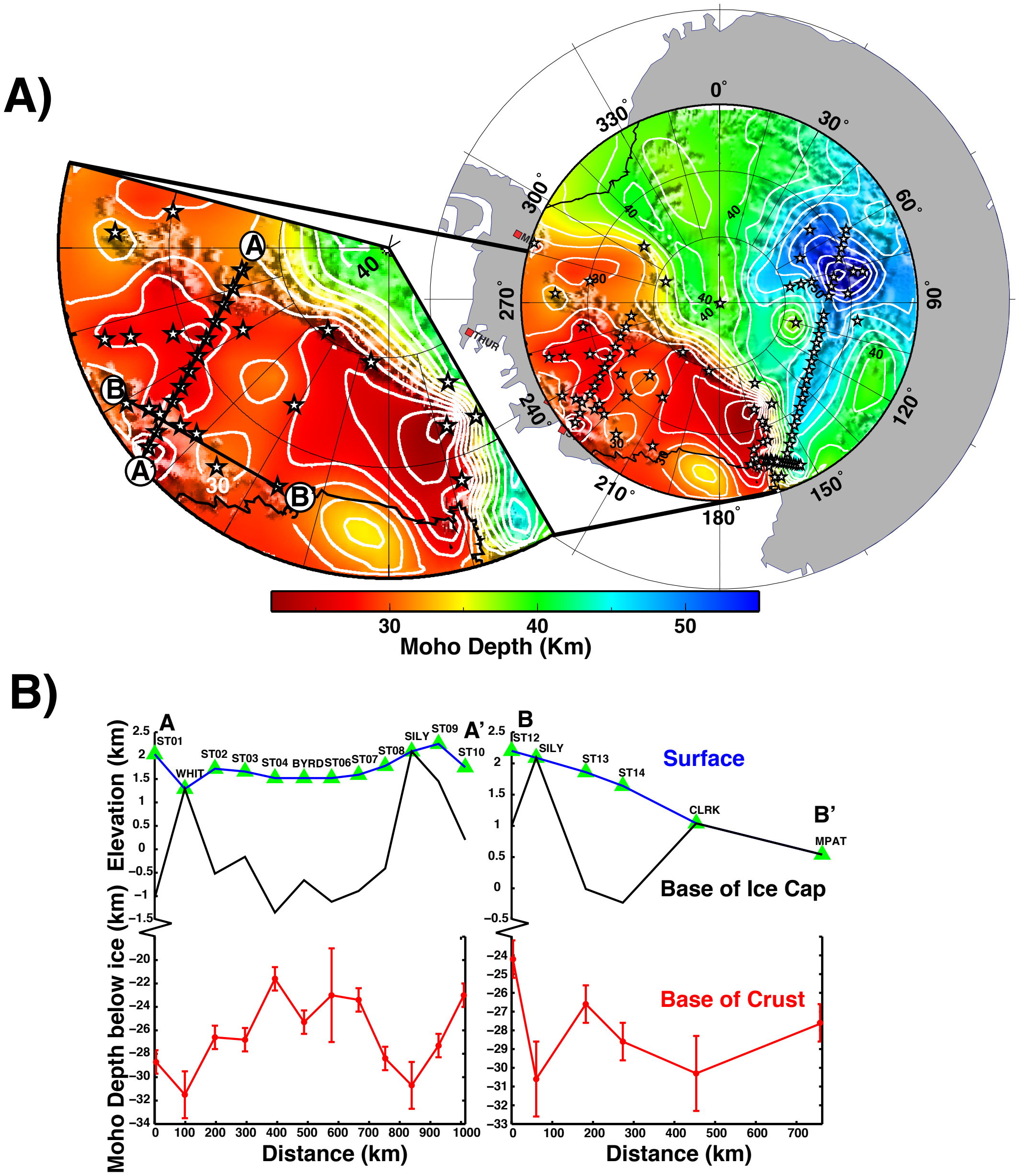

Figure 4.10: Crustal thickness map for Antarctica. A) Surface wave model (Sun et al) smoothly perturbed with receiver function results for all of Antartica, encompassing POLENET, AGAP, TAMSEIS, GSN, ANUBIS, and other experiments (see Appendix A). B) Crustal thickness profile for the transect A-A′. C) Crustal thickness profile for the transect B-B′.

4.10a. Note the symmetry between basal elevation and Moho depth for line A-A′. Such local crustal compensation further improves our confidence in our crustal determinations for these complex receiver functions.

4.6 Geological interpretation

There has been a great deal of speculation concerning the general stability of the West Antarctic Ice Sheet, and the implications of crustal and mantle properties on the near future evolution of the ice sheet and underlying rift system. As mentioned in the general introductory section, the WARS presents a large body of evidence for it being a mostly dormant, relatively cool rift system, despite a few contradictions in the form of missing sedimentation in subglacial troughs and evidence for young subglacial volcanism across the WAIS [*Winberry,* 2004, *LeMasurier,* 2008].

Our findings, summarized by Figure 4.10, show reciprocity between localized crustal thinning and the presence of subglacial troughs, thus suggesting that the WAIS has undergone discrete periods of ductile extension, perhaps due to reactivation of pre-existing weak zones. This episodic rifting behavior is supported by evidence for concurrently episodic rift shoulder uplift in the TAM [*Behrendt,* 1999], though rates have been debated [*Wilch and McIntosh,* 2000]. Overall, the WAIS seems to have accommodated extension more or less uniformly over its dominantly late Mesozoic to Cenozoic periods of extension. Though rift systems are typically accompanied by mantle upwelling, examples without slow upper mantle velocities have been reported, such as the Baikal Rift [*Tiberi et al,* 2003, *Liu and Gao,* 2006], where a substantially dilated mantle transition zone was observed, pointing to a cool upper mantle and the lack of a mantle plume as an origin to rifting. This has been tentatively explained by the initiation of a period of high surface heat flux over the rift area in the past, which led over time to a cooler mantle. Land gravity surveys have suggested that most of the WAIS, which features crust as thin as $\sim$20 km under subglacial troughs, is more or less compensated in the crust [*Jordan et al.*, 2010, *Huerta*, 2012], further reinforcing the idea that the mantle beneath the WAIS is normal, and that the hypothesized mantle plume beneath MBL does not extend beneath the WAIS. Indeed, P and S-wave tomography efforts for POLENET have identified a prominent low velocity anomaly under the MBL that appears to extend past 410 km, further supporting a mantle plume model for MBL uplift and crustal thinning, but a relatively normal/fast upper mantle was observed beneath the WAIS and the Whitmore/Ellsworth block. [*Nyblade*, 2011].

Alongside tomographic studies, there exists a slew of evidence relating potential plume activity to uplift in the MBL and the TAM. The MBL currently consists of an uplifted and faulted basement of alkaline basaltic rocks, topped with 18 trachytic shield volcanoes, and basalts found there are identical to oceanic island basalts sampled in known mantle plume systems [*LeMasurier and Rex*, 1989, *LeMasurier*, 2008]. Crustal values recovered here have confirmed sparse previous [*Winberry*, 2004, *Block et al.*, 2009] studies suggesting a thin crust under the WAIS, and have further corroborated suspicions of a thin, mantle-compensated crust in the Marie Byrd Land volcanic province. A thin MBL crust therefore contradicts views of a much thicker crust-compensated MBL [*Luyendyk et al.*, 2003], and reinforces the idea of a particularly hot buoyant mantle anomaly beneath the MBL.

Recent satellite gravity studies through GRACE [*Block et al.,* 2009] have also detected very large gravity anomalies under the MBL, indicative of either a substantial crustal root or a buoyant upper mantle. Gravity may be used to estimate "missing crust" with respect to airy isostacy when inputing crustal determinations from the joint surface wave and receiver function map. A comparison of the current gravity-based crustal map of Antarctica with our map presented here suggests that the MBL may be compensated in mantle by as much as an equivalent 20 km root [*Huerta,* 2012], a trait shared by most of the Trans-Antarctic Mountains, whereas the WAIS is more or less compensated in the crust to very slightly mantle compensated. GRACE satellite data also places substantial crustal thinning in the Ellsworth Mountains (HOWD, WILS), which is not observed here, though there is considerable ambiguity in the receiver functions deployed on those escarpments due to complex azimuth dependent crustal structure. Aerogravity studies have also identified a zone of particularly pronounced thinning in the Pine Island Glacier area (stations UPTW and DNTW) which may be the result of the newly identified Pine Island Rift [*Jordan et al.,* 2010]. Surface wave tomography of Antarctica including the POLENET array has also suggested particularly thin crust in that region [*Sun et al.,* 2011], and this is supported by the results of our PRFs and surface wave tomography [*Sun et al.,* 2011].

Though it is conceivable that mantle velocities may be somewhat slow, with the WAIS crustal compensation explained by the extremely shallow Moho values found here (thus not necessitating a deep crustal root for Airy isostacy), it is more likely, given the lack of such low velocities under the WAIS as imaged by POLENET body wave tomography [*Nyblade,* 2011], and the absence of any localized uplifted crust [*Huerta,* 2012] as one might expect if plume activity were present under the WAIS, we favor a model where there exist low velocity anomalies under the Terror Rift and the MBL that do not extend significantly under the WAIS. Note that this does not preclude rift related active volcanism under the some portions of the WAIS near the rift shoulders, as has been observed through radar near the Whitmore Mountains, a proposed rift shoulder extension to the WARS [*Blankenship et al.,* 1992]. It does however oppose the idea of very young widespread volcanism underlying the WAIS [*Behrendt,* 1999], and any likelihood of Neogene extension in subglacial basins [*LeMasurier,* 2008]. Our results are therefore consistent with a cool, largely dormant rift system, rather than an active one. In progress studies of mantle discontinuities via receiver functions may shed light on this matter.

In modeling the potential evolution of the WAIS, we must consider a variety of parameters, such as lithospheric thickness, heat flow and mantle viscosity. Small variations in these parameters can have substantial effects on ice sheet growth and melt rates [*Pollard et al.,* 2005], and must therefore be estimated very carefully. The crustal structure estimated here can be compared to continental regions of similar lithospheric thickness to infer heat flow rates [*Pollard et al.,* 2005, *Nyblade,* 1999], and tomographic images can be used to determine mantle viscosity. As such, the results presented here will be crucial in formulating future glaciological models of the evolution of the WAIS, and determining its ultimate role in global climate change.

4.7 Conclusions

We have demonstrated that inherent difficulties involved in interpreting P-receiver functions over complex shallow media involving ice sheets can be over-come through a combination of forward modeling and inversion approaches even if there is a limited amount of a priori information concerning the layer thicknesses and velocities. Given the extremely large impedance contrast between the crust and the ice sheet, it is imperative to correctly model the ice sheet multiples if we are to subsequently fit a crustal model. As West Antarctic subglacial topography can be substantial, the effect of basal dip along with potential sedimentary basins on the generation of multiples must be taken into account if a simple flat layer model cannot correctly fit early converted phases. These discrepancies in modeled early multiples can potentially be interpreted as shallow sedimentary basins, though basal dip can generate similar signatures even when the exact ice sheet thickness is known. Future studies involving PRFs over ice sheets should approach interpretation through a forward model capable of handling dipping layers and variable Poisson's ratios. We have subsequently applied an MCMC inversion scheme to PRFs from POLENET, and combined these results with previous receiver function studies and ongoing surface wave tomography to generate an updated crustal map of Antarctica, showing a thin crust across the West Antarctic Ice Sheet with thickening into the Ellesworth Mountains and modest thickening over the Marie Bryd Land dome. These measurements combined with current tomographic efforts support a thin crust under the WAIS overlying a normal to slightly slower mantle, and a hot mantle anomaly underlying a thin, uplifted crust under the MBL. Further corroborations in the joint model support the presence of highly thinned crust near the newly identified Pine Island Rift. Crustal determinations generated here, when compared to gravity studies, yield estimates of the degree of crustal under-compensation for West Antarctica, suggesting that as much as 20 km of crust may be "missing" from under the MBL and Trans-Antarctic Mountains, supporting models featuring substantial mantle upwelling in those areas, and much less under the WAIS. Crustal determinations presented here will play an important in generating future models of WAIS evolution in the scope of global climate change.

EPILOGUE AND FUTURE WORKS

The results presented in this dissertation open several avenues for future studies. Results pertaining to wavefield equipartition have confirmed that Strombolian eruption coda reaches a diffuse state in a few seconds after the short period onset, thus fulfilling the theoretical requirements for Green's function recovery via correlation. Also of interest is the observation that icequakes, initially thought to be too small to carry energy to a meaningful distance or depth, also reach equipartition, as is evident by the very similar frequency dependent energy ratios noted over multiple transient events. Given that lower amplitude transient signals may not attain equipartition, or may not display a diffuse character for a useable length of time, the use of small permanent arrays embedded in a larger deployment could be used to identify transient signals, such as the 250 000+ icequakes from [*Knox*, 2012], which would match the local frequency dependent energy ratio computed from larger events, such as eruptions. As such, any event locally displaying equipartition for an arbitrary length of time could be used to bolster real-time eruption-derived scattering models. As the Green's function has been shown to require a large amount of data for convergence (e.g. ambient noise, [*Campillo*, 2003]), it is not unreasonable to expect the same from body waves, and the addition of several hundred thousand icequake-derived Green's functions could help with reducing noise levels substantially as well as filling in gaps in coverage where eruptive activity is low. The advantage here is that icequake generation presents, at least for Erebus, a highly seasonal dependence [*Knox*, 2012], thus guaranteeing an updated image of the Erebus magmatic system at regular intervals. Some degree of exploration as to the potential convergence of the local Green's functions using this type of source would have to be conducted as a first step.

Furthermore, modeling of the radiative transfer equation have shown that the time a wavefield takes to reach equipartition and the length of time this character is shown to be stable depends greatly on the source-station distance and the density of scatterers. Distant stations will tend to record longer codas, thus maintaining equipartition for longer, though the coda length is also dependent on the dissipative characteristics of the medium. For Strombolian eruptions recorded on Erebus, stations as far as HOO (6 km) display pronounced coda ideal for scattering studies, though for icequakes, where the source amplitude and the source-station distance present much more variability, a system of embedded very small arrays as mentioned above could be used to evaluate signals on an event to event basis. Given the convergence of the scattering model for station numbers above $\sim$30, a well distributed permanent array of a similar number of broadband stations could conceivably recover a high resolution temporally varying model of Erebus for any high frequency transient signal.

The prospect of using icequakes also makes this method possible at other less persistently active volcanoes that happen to feature ice caps, such as volcanoes in the Cascades, some of which have been identified as high risk systems. Given that the source location does not matter, as all source-specific information is lost in the equipartitioned wavefield, one could furthermore install a single repeating impulsive source, such as a large automated hammer system, to generate repeating anthropogenic signals that could be used to evaluate the scattering structure of a medium. The propensity for such a setup to generate a large quantity of events would likely guarantee Green's function convergence within the depth sensitivity range of the source. Properly calibrating source power however may require finite difference modeling which takes into account dissipation effects or practical laboratory experiments to test for the extent of convergence of the medium's Green's function with a variety of source parameters.

On the subject of receiver functions, studies through deployments in Antarctica are subject to a variety of shallow structural complexities which must be taken into account before meaningful information about the crustal and mantle can be recovered. Given the extreme contrast in the Poisson's ratios between ice sheets, sedimentary basins and the underlying crust, and in light of the high amplitude signatures such contrasts generate, it is particularly important to properly model the shallow most layers. Future works using receiver functions in Antarctica will have need for a forward model capable of handling dipping or arbitrarily shaped layers in order to minimize fitting artifacts in later inversions steps, which are typically the result of poorly fit early multiples. Furthermore, even with accurate estimates of ice sheet thickness inferred by drilling, any complexity in basal topography can effectively masquerade as a sedimentary basin. We suggest that in order to properly constrain sedimentary basin thickness, a priori knowledge of basal topography must also be known, and as such perhaps future efforts to map out sediment thickness across West Antarctica will be bolstered by radar surveys of the transect lines presented here.

A subsequent broadband deployment is currently being planned over the Ross Sea, where novel approaches will have to be developed in order to recover information from the crust due to the presence of a water layer that will necessarily obscure any upcoming S-wave signature. Furthermore, mantle discontinuities thus far remain largely elusive in West Antarctica. Although synthetic modeling reveals that ice sheet and sedimentary basin multiples may extend well into the arrival times of mantle transition zone conversions, such arrivals should still be identifiable given their generally lower frequency. The reasons for which mantle structure can not be reliably imaged, despite weak emergence at several stations, is unknown, though it is not a product of the deconvolution as several different methods were tried. Future works may elucidate this mystery.

APPENDIX A

The following table is a list of all other stations used in the making of the Antarctic crustal map (Figure 4.10). Latitude/longitude, inferred Moho depth, estimated error on the Moho depth, ice sheet thickness, station elevation and reference experiments are noted. For the most part, these additional stations are limited to East Antarctica, and Moho estimates for experiments denoted TAMSEIS, GAMSEIS and AGAP were conducted using S-wave receiver functions through the works of [*Hansen et al.*, 2009]. The algorithm used in these estimates only provides a standard error of $\sim$2 km, thus the uniformity on posted errors.

Station	Lat	Lon	Moho (km)	Error (km)	Ice (km)	Elevation (km)	Project
N124	-82.0745	107.6406	45	2	2.61	3.36	GAMSEIS
N132	-82.0751	101.9534	41.9	2	3.54	3.44	GAMSEIS
N140	-82.0086	96.76920	46.2	2	3.06	3.57	GAMSEIS
N156	-81.6726	86.50450	44	2	2.36	3.84	GAMSEIS
N165	-81.4084	81.76040	53.7	2	2.83	3.97	GAMSEIS
N173	-81.1122	77.47360	56.7	2	2.59	4.06	GAMSEIS
N182	-80.7363	73.18980	55.7	2	2.07	4.05	GAMSEIS
N190	-80.3275	69.43100	48.3	2	3.34	3.92	GAMSEIS
N198	-79.8597	65.96070	50.3	2	2.99	3.78	GAMSEIS
N206	-79.3947	62.85560	47.2	2	3.10	3.66	GAMSEIS
N215	-78.9045	59.99430	44.6	2	3.03	3.55	GAMSEIS
P061	-84.4996	77.22380	43.1	2	2.88	3.51	AGAP
P071	-83.6465	77.33470	40.2	2	2.82	3.65	AGAP
P080	-82.8054	77.36400	45.1	2	2.96	3.81	AGAP
P116	-79.5669	77.04510	54.9	2	1.76	3.93	AGAP
P124	-78.8718	77.65700	57.5	2	1.45	3.61	AGAP
GM01	-83.9858	104.7291	31.4	2	3.12	3.72	AGAP
GM02	-79.4251	97.58150	39.5	2	2.81	3.72	AGAP
GM03	-80.2169	85.94390	53.4	2	2.75	3.92	AGAP
GM04	-82.9997	61.11240	48.4	2	3.06	3.77	AGAP
GM05	-81.1841	51.15880	46.7	2	3.51	3.77	AGAP
BYRD	-80.0160	-119.547	27	2	2.16	0	ANUBIS
MBLO	-78.0930	-130.224	25	2	1.78	0	ANUBIS
SDMO	-81.6150	-148.850	27	2	0.98	0.65	ANUBIS
MTM	-79.4960	-100.012	21	2	3.21	2.03	ANUBIS
ISDE	-80.0000	-134.993	28	2	1.56	0	ANUBIS
CPHI	-75.0745	162.6484	34	2	0	0.34	TAMSEIS
OND	-80.7457	-125.7358	28	2	2.01	0	ANUBIS
STC	-82.3575	-136.4062	31	2	1.03	0	ANUBIS
E000	-77.62621667	163.6175	22.7	2	0	0.74	TAMSEIS
E002	-77.57501667	163.0077667	22.4	2	0	0.79	TAMSEIS
E004	-77.41330556	162.0660833	29.5	2	0	0.63	TAMSEIS
E006	-77.37028333	161.6255667	29.9	2	0	0.46	TAMSEIS
E008	-77.28166667	160.5033333	38.4	2	0	0.99	TAMSEIS
E010	-77.18528333	160.0098	39	2	0	1.65	TAMSEIS
E012	-77.04613333	159.3246667	40.5	2	0.54	1.92	TAMSEIS
E014	-76.98983333	158.6216667	39.2	2	0.69	2.09	TAMSEIS
JNCT	-76.92877778	157.9012222	36.9	2	0.82	2.13	TAMSEIS
E018	-76.8234	157.22368	39.2	2	1.59	2.09	TAMSEIS
E020	-76.7295	156.54715	43.5	2	1.52	2.12	TAMSEIS
E022	-76.62796667	155.9025333	44	2	1.92	2.15	TAMSEIS
E024	-76.5346	155.2500	44.2	2	1.57	2.21	TAMSEIS
E026	-76.42475	154.75815	44	2	1.58	2.21	TAMSEIS
E028	-76.30746667	154.0384333	43.6	2	2.05	2.25	TAMSEIS
E030	-76.25103333	153.37925	43.4	2	2.07	2.26	TAMSEIS
N000	-76.00873333	160.3784167	32.8	2	0	1.56	TAMSEIS
N020	-77.46783333	155.8175	38.6	2	1.86	2.28	TAMSEIS
N028	-78.02958	153.65086	43.6	2	2.27	2.21	TAMSEIS
N036	-78.55078333	151.27755	41.8	2	1.98	2.24	TAMSEIS
N044	-79.0692	148.6159333	44.7	2	2.44	2.27	TAMSEIS
N052	-79.5441	145.7488833	45	2	2.32	2.27	TAMSEIS
N060	-80.00001667	142.5935833	45.1	2	2.70	2.26	TAMSEIS
N068	-80.39105	138.9200	45	2	2.89	2.36	TAMSEIS
N076	-80.80606667	135.4325667	45.4	2	2.35	2.47	TAMSEIS
N084	-81.16006667	131.4673333	44	2	2.44	2.65	TAMSEIS
N092	-81.4621	126.9822333	44	2	2.71	2.79	TAMSEIS
N100	-81.69101151	122.4672241	42.9	2	2.60	2.93	TAMSEIS
N108	-81.8791	117.6036	44.4	2	2.60	3.06	TAMSEIS
N116	-82.00936667	112.5697833	42.7	2	2.26	3.18	TAMSEIS
QSPA	-89.929	144.438	34	2	2.81	2.85	GSN
TNV	-77.517	161.853	18.8	2	0	0.04	GSN
CPHI	-75.07	162.65	32	2	0	0.34	TAMSEIS
MAGL	-76.14	162.41	34.4	2	0.20	0.22	TAMSEIS
VNDA	-77.52	161.85	35.3	2	0	0.15	GSN
CBOB	-77.03	163.17	30	7.4	0	-0.04	TAMSEIS
CASE	-80.44	160.10	24	3.5	0	1.19	TAMSEIS
MINN	-78.55	166.88	30	2.4	0	0.43	TAMSEIS
CBRI	-77.25	166.43	19	2.7	0	0.3	TAMSEIS
CCRZ	-77.52	169.09	25	4.5	0	0.89	TAMSEIS
MAGL	-76.14	162.41	33	4.7	0.20	0.22	TAMSEIS
CTEA	-78.94	160.76	30	1.8	0	1.25	TAMSEIS
DIHI	-79.85	159.48	33	2.2	0	1	TAMSEIS
E004	-77.41330556	162.0660833	34	1.1	0	0.63	TAMSEIS
E006	-77.37028333	161.6255667	30	2.1	0	0.46	TAMSEIS
E008	-77.28166667	160.5033333	38	1.3	0	0.99	TAMSEIS
E010	-77.18528333	160.0098	39	0.6	0	1.65	TAMSEIS
N000	-76.00873333	160.3784167	39	1.2	0	1.56	TAMSEIS
SBA	-77.85	166.76	27	0.3	0	0.02	GT

Table 4.2: Other stations used in the Antarctic crustal map

APPENDIX B

Data storage and archiving is conducted by the IRIS PASSCAL Data Management Center. In order to request a usable database of teleseismic events for the POLENET experiment, the following procedure must be followed. The DMC (http://www.iris.edu/dms/dmc/) provides a variety of tools to facilitate the request of large datasets, and we use two of these, SOD and Breqfast, to construct our database used to compute PRFs in West Antarctica. As POLENET is a partially restricted archive, and SOD cannot submit requests for restricted data, we use SOD to produce Breqfast requests for individual events, which are then downloaded as encrypted SEED archives. The SOD script for generating requests for the POLENET database is as follows:

```
<sod>
        <properties>
        <eventLag>
            <unit>HOUR</unit>
            <value>0</value>
        </eventLag>
        <eventChannelPairProcessing>noCheck</eventChannelPairProcessing>
    </properties>
    <eventArm>
        <eventFinder>
            <name>IRIS_EventDC</name>
            <dns>edu/iris/dmc</dns>
            <pointDistance>
                <unit>DEGREE</unit>
                <min>25</min>
                <max>95</max>
                <latitude>-90</latitude>
                <longitude>0</longitude>
            </pointDistance>
            <originDepthRange>
                <unit>KILOMETER</unit>
                <min>0</min>
                <max>200</max>
            </originDepthRange>
            <originTimeRange>
```

```
            <startTime>
                2008-02-01T00:00:00.000Z %% Start time range
            </startTime>
            <endTime>
                2011-12-31T23:59:59.999Z %% End time range
            </endTime>
        </originTimeRange>
        <magnitudeRange>
            <magType>MB</magType>
            <magType>MW</magType>
            <min>5.5</min> %% Magnitude cutoff
            <max>10</max>
        </magnitudeRange>
        <catalog>PREF</catalog>
    </eventFinder>
    <removeEventDuplicate/>
</eventArm>
<networkArm>
    <networkFinder>
        <name>IRIS_NetworkDC</name>
        <dns>edu/iris/dmc</dns>
    </networkFinder>
    <networkOR>
        <networkCode>YT</networkCode> %% Network code
    </networkOR>
    <stationAND>
        <stationOR>
            <stationCode>ST01</stationCode>
            <stationCode>ST02</stationCode>
            <stationCode>ST03</stationCode>
            <stationCode>ST04</stationCode>
            <stationCode>ST06</stationCode>
            <stationCode>ST07</stationCode>
            <stationCode>ST08</stationCode>
            <stationCode>ST09</stationCode>
            <stationCode>ST10</stationCode>
            <stationCode>ST12</stationCode>
            <stationCode>ST13</stationCode>
            <stationCode>ST14</stationCode>
            <stationCode>SILY</stationCode>
            <stationCode>CLRK</stationCode>
            <stationCode>DNTW</stationCode>
            <stationCode>FALL</stationCode>
            <stationCode>KOLR</stationCode>
            <stationCode>WNDY</stationCode>
            <stationCode>WHIT</stationCode>
            <stationCode>LONW</stationCode>
            <stationCode>MILR</stationCode>
            <stationCode>MPAT</stationCode>
            <stationCode>SIPL</stationCode>
            <stationCode>SURP</stationCode>
            <stationCode>DEVL</stationCode>
            <stationCode>DUFK</stationCode>
            <stationCode>FISH</stationCode>
            <stationCode>HOWD</stationCode>
            <stationCode>MECK</stationCode>
            <stationCode>PECA</stationCode>
            <stationCode>WAIS</stationCode>
            <stationCode>WILS</stationCode>
            <stationCode>BYRD</stationCode>
            <stationCode>THUR</stationCode>
            <stationCode>UNGL</stationCode>
            <stationCode>UPTW</stationCode>
```

```
        </stationOR>
    </stationAND>
     <channelAND>
        <bandCode>B</bandCode>
        <gainCode>H</gainCode>
     </channelAND>
</networkArm>

<waveformArm>
                <eventStationAND>
                    <distanceRange>
                        <unit>DEGREE</unit>
                        <min>25</min> %% Min and Max angle
                        <max>95</max>
                    </distanceRange>
                </eventStationAND>
    <phaseRequest>
            <model>ak135</model>
            <beginPhase>ttp</beginPhase> %% Chosen Phase (P)
            <beginOffset>
                    <unit>MINUTE</unit>
                    <value>-1</value> %% Time before phase
            </beginOffset>
            <endPhase>ttp</endPhase>
                <endOffset>
                    <unit>MINUTE</unit>
                    <value>2</value> %% Time after phase
                </endOffset>
    </phaseRequest>
    <requestNOT>
        <breqFastRequest>
            <workingDir>/fs/raid/users/jchaput/Desktop/POLENET_CODE/requests_S/</workingDir>
            <name>Julien Chaput</name>
            <inst>New Mexico Institute of Mining and Technology</inst>
            <mail>New Mexico Institute of Mining and Technology,
            Department of Earth and Environmental Science, MSEC 208,
            801 Leroy Place, Socorro, New Mexico 87801</mail>
            <email>jchaput@ees.nmt.edu</email>
            <phone>575-418-9617</phone>
            <fax>none</fax>
            <media>Electronic</media>
            <altmedia1>Electronic</altmedia1>
            <altmedia2>Electronic</altmedia2>
            <quality>b</quality>
        </breqFastRequest>
    </requestNOT>

   <!-- <requestPrint />  view request for debugging purposes -->
    <fixedDataCenter>
                <name>IRIS_DataCenter</name>
                <dns>edu/iris/dmc</dns>
    </fixedDataCenter>
    <fullCoverage />
    <responseGain />
    <rMean />
    <rTrend />

    <printlineSeismogramProcess>
        <filename>SOD_seismograms_P.log</filename>
        <template>Got $seismograms.size() seismograms,
        Event_${event.getTime('yyyy_DDD_HH_mm_ss')}, ${event.latitude},
        ${event.longitude}, ${event.depth}, ${station.codes}.${channel.code},
        ${station.latitude}, ${station.longitude}</template>
```

```
        </printlineSeismogramProcess>

    </waveformArm>
</sod>
```

To execute this script, SOD must be downloaded and properly referenced in the startup path file. There have been past issues with running SOD with 64-bit platforms, though this issue may be fixed at this time. In a terminal window, this script may be called as:

```
sod f request_script.xml
```

For every event between 25 and 95 degrees from 2008/01 to 2011/12, and for depths of 10-200 km with magnitudes over 5.5, qualifying events will generate Breqfast requests, which are then mailed to the DMC (in c-shell):

```
foreach i(*.breq)
mail breq_fast@iris.washington.edu < $i
end
```

Once the data is ready, the DMC will also provide an e-mail detailing how to log into the automated data server and download the requested data. For users on Mac platforms, consider inputting the following commands once logged in to avoid instabilities:

```
epsv
prompt
binary
```

For restricted datasets, decrypt the data as follows:

```
foreach i (*.openssl)
set pp = ‘echo $i | sed ’s/.openssl//’‘
/usr/bin/openssl enc -d -des-cbc -salt -in
$i -out $pp -pass pass:{password}
end
```

And convert the decrypted SEED volumes to SAC format using this:

```
foreach i (20*)

set kk = ‘echo $i‘
mkdir ./P_DATA2/$kk

echo $i >> input.rd
echo  >> input.rd
echo  >> input.rd
echo d >> input.rd
echo  >> input.rd
echo  >> input.rd
echo  >> input.rd
echo  >> input.rd
echo  >> input.rd
echo  >> input.rd
echo  >> input.rd
echo  >> input.rd
```

```
echo  >> input.rd
echo  >> input.rd
echo  >> input.rd
echo  >> input.rd
echo  >> input.rd
echo  >> input.rd

rdseed < input.rd

echo

foreach jj (*.SAC)
    mv $jj ./P_DATA2/$kk/$jj
end

rm input.rd
end
```

The directories and wildcards are to be changed to the local directory tree. The data length sent back by the DMC can sometimes differ from the parameters set in the script. This is unavoidable, and on the DMC end.

REFERENCES

[*Aki and Richards,* 1980] Aki, K., Richards, P., Quantitative Seismology, University Science Books, 700 pp., 1980

[*Aki,* 1957] Aki, K., Space and time spectra of stationary stochastic waves, with special reference to microtremors, *Bull. Earthq. Res. Inst.*, Vol. 35, pp. 415-456, 1957

[*Aki and Chouet,* 1975] Aki, K., Chouet, B., Origin of coda waves: Source, attenuation, and scattering effects, *J. Geophys. Res.*, Vol. 80, No. 23, pp. 3224-3343, 1975

[*Ammon,* 1991] Ammon, C. J., The isolation of receiver effects from teleseismic P waveforms, *Bull. Seism. Soc. Am.*, Vol. 81, pp. 2504-2510, 1991

[*Aster et al.,* 1990] Aster, R., Shearer, P., Berger, J., Quantitative measurements of shear wave polarizations at the Anza seismic network, Southern California: Implications for shear wave splitting and earthquake prediction, *J. Geophys. Res.*, Vol. 95, pp. 12449-12473, 1990

[*Aster et al.,* 2003] Aster, R., et al., Very long period oscillations of Mount Erebus Volcano, *J. Geophys. Res.*, 108(B11), pp. 2522-2544, doi: 10.1029/2002JB002101, 2003.

[*Aster et al.,* 2004] Aster, R., et al, Real-time data received from Mount Erebus volcano, Antarctica, *Eos Transactions of AGU*, Vol. 85, Iss. 10, pp. 97-102, 2004

[*Aster et al.,* 2008] Aster, R., et al., Moment tensor inversion of very long period seismic signals from Strombolian eruptions of Erebus Volcano, *J. Volcanol. Geotherm. Res.*, Vol. 177, Iss. 3, pp. 635-647, doi:10.1016/j.jvolgeores.2008.08.013, 2008.

[*Aster et al.,* 2012] Aster, R.C., Borcher, B., Thurber, C.H., Parameter Estimation and Inverse Problems, Second Edition, 301 pp., 2012.

[*Bannister et al.,* 2000] Bannister, S., et al, Shear-wave velocities under the Transantarctic Mountains and Terror rift from surface wave inversion, *Geop. Res. Lett.*, Vol. 27, No. 2, pp.281-294, 2000

[*Bannister et al.,* 2003] Bannister, S.C., et al., Variations in crustal structure across the transition from west to east Antarctica, Southern Victoria Land, *Geophys. J. Int.*, Vol. 155, Iss. 3, pp. 870-884, 2003

[*Barros et al.,* 2012] De Barros, L., et al., Imaging magma storage below Teide volcano (Tenerife) using scattered seismic wavefields, *Geophys. J. Int.*, Vol. 191, Iss. 2, pp. 695-706, doi: 10.1111/j.1365-246X.2012.05637, 2012

[*Behrendt and Cooper,* 1991] Behrendt J., Cooper A., Evidence of rapid Cenozoic uplift of the shoulder escarpment of the Cenozoic West Antarctic rift system and a speculation on possible climate forcing, *Geology*, Vol. 19, pp. 315-319, 1991

[*Behrendt*, 1999] Behrendt, J., Crustal and lithospheric structure of the West Antarctic Rift System from geophysical investigations a review, *Global and Planetary Change*, Vol. 23, pp. 25-44, 1999

[*Bell et al.,* 1998] Bell R.E., et al., Influence of subglacial geology on the onset of a West Antarctic ice stream from aerogeophysical observations, *Nature*, Vol. 394, pp. 58-62, 1998

[*Bentley,* 1973] Bentley, C., R., Crustal structure of Antarctica, *Tectonophysics*, Vol. 20, pp. 229-240, 1973

[*Bentley,* 1971] Bentley, C., R., Seismic anisotropy in the West Antarctic ice sheet, *AGU Antarctic. Res. Ser.*, Vol. 16, pp. 131-177, 1971

[*Bianco et al.,* 2006] Bianco, F., et al., Shear wave splitting changes associated with the 2001 volcanic eruption on Mt Etna, *Geophys. J. Int.*, Vol. 167, Iss. 2, pp. 959-967, 2006

[*Blankenship et al.,* 1992] Blankenship D., et al., Active volcanism beneath the West Antarctic ice sheet and implications for ice-sheet stability, *Nature*, Vol. 361, pp. 526-529, 1992

[*Block et al.,* 2009] Block A., Bell R., Studinger M., Antarctic crustal thickness from satellite gravity: Implications for the Transantarctic and Gamburtsev Subglacial Mountains, *Earth Planet. Sci. Lett.*, Vol. 288, pp. 194-203, 2009

[*Bodin et al.,* 2012] Bodin T., M. et al., Transdimensional inversion of receiver functions and surface wave dispersion, *J. Geophys. Res.*, Vol. 117, B02301, 24 pp., 2012

[*Brenguier et al.,* 2007] Brenguier, F., et al., V., 3D surface wave tomography of the Piton de la Fournaise volcano using seismic noise correlations, *Geop. Res. Lett.*, Vol. 34, 5 pp., 2007.

[*Brenguier et al.,* 2008] Brenguier, F., et al, Towards forecasting volcanic eruptions using seismic noise, *Nature Geoscience*, Vol. 1, Iss. 2, pp. 126-130, 2008

[*Brink and Taylor,* 2002] Brink, U., Taylor, M., Crustal structure of central Lake Baikal: Insights into intracontinental rifting, *J. Geophys. Res.*, Vol. 107, No. B7, 15 pp., 10.1029/2001JB000300, 2002

[*Campillo,* 2003] Campillo, M., and A. Paul, Long-range correlations in the diffuse seismic coda, *Science*, Vol. 299, pp. 547549, 2003

[*Chaput et al.,* 2012] Chaput, J., et al, Imaging of Erebus volcano using body wave seismic interferometry of Strombolian eruption coda, *Geop. Res. Lett.*, Vol. 39, 5 pp., 2012

[*Cho,* 2011] Cho, T., Removing Reverberation in ice sheets from receiver functions, *Seism. Res. Lett.*, Vol. 82, pp. 207-210, 2011

[*Claerbout,* 1968] Claerbout, J. F., Synthesis of a layered medium from its acoustic transmission response, *Geophysics*, Vol. 33, pp. 264269, 1968.

[*Clowes et al.,* 2005] Clowes, R., et al., Lithospheric structure in northwestern Canada from Lithoprobe seismic refraction and related studies: a synthesis, *Can. Jour. of Ear. Sci.*, Vol. 42, Iss. 6, pp. 1277-1293, 10.1139/e04-069, 2005

[*Cooper et al.,* 1987] Cooper, A., Davey, F., Behrendt, J., Seismic stratigraphy and structure of the Victoria Land Basin, western Ross Sea, Antarctica, The Antarctic continental margin; geology and geophysics of the western Ross Sea, *Circum-Pacific Council for Energy and Mineral Resources, Earth Science Series*, Houston TX, USA, pp. 27-76, 1987

[*Cooper et al.,* 1995] Cooper, A.K., Barker, P.F., Geology and Seismic Stratigraphy of the Antarctic Margin, *Antarct. Res. Ser.*, Vol. 68, American Geophysical Union, 303 pp., 1995

[*Crampin et al.,* 1984] Crampin, S., Evans, R., Atkinson, B., Earthquake prediction: A new physical basis, *Geophys. J. R. Astron. Soc*, Vol. 76, pp. 147-156, 1984

[*Danesi and Morelli,* 2001] Danesi S., Morelli A., Structure of the upper mantle under the Antarctic Plate from surface wave tomography, *Geop. Res. Lett.*, Vol. 28, pp. 4395-4398, 2001

[*Dibble et al.,* 1982] Dibble, R., Kienle, J., Kyle, P., Shibuya, K., Geophysical studies of Erebus Volcano, Antarctica, from December 1974 to January 1982, *N.Z.J. Geol. Geophys.*, Vol. 27, pp. 425-455, 1982

[*Dibble et al.,* 1994] Dibble, R., Obrien, B., Rowe, C., The velocity structure of Mount Erebus, Antarctica, and its lava lake, Volcanological and Environmental Studies of Mt Erebus, Antarctica, *Antarct. Res. Ser.*, Vol. 66, pp. 1-16, AGU, Washington, D.C., 1994

[*Dibble,* 1994] Dibble, R., Velocity modeling in the erupting magma column of Mount Erebus, Antarctica, Volcanological and Environmental Studies of Mt Erebus, Antarctica, *Antarct. Res. Ser.*, Vol. 66, pp. 17-33, AGU, Washington D.C., 1994

[*Draganov,* 2009] Draganov, D., et al, Reflection images from ambient seismic noise, *Geophysics*, Vol. 74, pp. A63-A67, 2009

[*Esser et al.,* 2004] Esser, R., et al., 40Ar/39Ar dating of the eruptive history of Mount Erebus, Antarctica: volcano evolution, *Bull. Volc.*, Vol. 66, pp. 671-686, 2004

[*Fitzgerald et al.,* 1992] Fitzgerald, P., The Transantarctic Mountains of southern Victoria Land; the application of apatite fission track analysis to a rift shoulder uplift, *Tectonics*, Vol. 11, No. 3, pp. 634-662, 1992

[*Giggenbach,* 1973] Giggenbach W. F., Kyle P. R., Lyon G. L., Present volcanic activity on Mount Erebus, Ross Island, Antarctica, *Geology*, Vol. 1, pp. 135-136, 1973.

[*Gerst et al.,* 2008] Gerst, A., Hort, M., Kyle, P., A 4D view of Strombolian eruptions and man-made explosions using multiple Doppler radar instruments, *J. Volcanol. Geotherm. Res.*, Vol. 177, No. 3, 13 pp., 2008

[*Gret,* 2004] Gret, A., Time-lapse monitoring with coda wave interferometry, PhD Dissertation, CWP, Colorado School of Mines, 2004

[*Haney et al.,* 2011] Haney, M. M., et al., Interpretation of Rayleigh-wave ellipticity observed with multicomponent passive seismic interferometry at Hekla Volcano, Iceland: *The Leading Edge*, Vol. 30, pp. 526-531, 2011

[*Hansen et al.,* 2009] Hansen, S.E., et al., Using S-wave receiver functions to estimate crustal structure beneath ice sheets: An application to the Transantarctic Mountains and East Antarctic craton, *Geochem. Geophys. Geosyst.*, Vol. 10, Q08014, 10 pp., doi: 10.1029/2009GC002576, 2009

[*Hansen et al.,* 2011] Hansen, S.E., et al., Crustal structure of the Gamburtsev Mountains, East Antarctica, from S-wave receiver functions and Rayleigh wave phase velocities, *Earth Planet. Sci. Lett.*, Vol. 300, Iss. 3-4, pp. 395-401, 2011

[*Harpel et al.,* 2004] Harpel, C.J., et al., 40Ar/39Ar dating of the eruptive history of Mount Erebus, Antarctica: summit flows, tephra, and caldera collapse. *Bull. Volc.*, Vol. 66, pp. 687-702, 2004.

[*Hayes et al.,* 1975] Hayes, D., et al., Initial reports of the Deep Sea Drilling Project, Washington D.C., US Government Printing Office, 1975

[*Hennino et al.,* 2001] Hennino, R., et al, Observation of equipartition of seismic waves, *Physical Review Letters*, Vol. 86, No. 15, pp. 3447-3450, 2001

[*Helffrich,* 2006] Helffrich, G., Extended-time multi-taper frequency domain cross-correlation receiver function estimation, *Bull. Seism. Soc. Am.*, Vol. 96, pp. 344-347, 2006

[*Hong,* 2012] Hong, T., Menke, W., Imaging laterally varying regional hetergeneities from seismic coda using a source-array analysis, *Phys. Eart. Plan. Int.*, Vol. 166, Iss. 3-4, pp.188-202, 2008

[*Huerta,* 2012] Huerta, A., Crust and mantle compensation for POLENET crustal values, *Pers. Comm.*, 2012

[*Jordan et al.,* 2010] Jordan T.A., et al., Aerogravity evidence for major crustal thinning under the Pine Island Glacier region (West Antarctica), *Bull. Geo. Soc. Am.*, Vol. 122, pp. 714-726, 2010

[*Jones et al.,* 2008] Jones, K.R., et al., Infrasonic tracking of large bubble bursts and ash venting at Erebus volcano, Antarctica. *J. Volcanol. Geotherm. Res.*, Vol. 177, pp. 661-672, 2008

[*Karner et al.,* 2005] Karner, G.D., Studinger, M., Bell, R.E., Gravity anomalies of sedimentary basins and their mechanical implications: Application to the Ross Sea basins, West Antarctica, *Earth Planet. Sci. Lett.*, Vol. 235, pp. 577 - 596, 2005

[*Kelly et al.,* 2008] Kelly, P., et al., Refinement of the late Quaternary geologic history of Erebus volcano, Antarctica using 40Ar/39Ar and 36Cl age determinations, *J. Volcanol. Geotherm. Res.*, Vol. 177, Iss. 3, pp. 569-577, 2008

[*Kennett*, 1991] Kennett, B.L.N. (Compiler and Editor), *IASPEI 1991 Seismological Tables*, Bibliotech, Canberra, Australia, 167 pp., 1991

[*Kohnen,* 1974] Kohnen, H., The temperature dependence of seismic waves in ice, *Journal of Glaciology*, Vol. 13, No. 67, pp. 144-147, 1974

[*Knox,* 2012] Knox, H., Eruptive characteristics and glacial earthquake investigation on Erebus volcano, Antarctica, Dissertation, 2012.

[*Kyle,* 1990] Kyle, P.R., Erebus volcanic province: summary, Volcanism of the Antarctic Plate and Southern Oceans, *Antarct. Res. Ser.*, Vol. 48, AGU, pp. 18-25, 1990

[*Kyle et al.,* 2008] Kyle, P., et al., A Sr, Nd, Hf, and Pb isotope perspective on the genesis and long-term evolution of alkaline magmas from Erebus volcano, Antarctica, *J. Volcanol. Geotherm. Res.*, Vol. 177, Iss. 3, pp. 606-618, 2008

[*Lahaie and Grasso,* 1998] Lahaie, F., Grasso, J.R., A fluid-rock interaction cellular automaton of volcano mechanics: Application to the Piton de la Fournaise, *J. Geophys. Res.*, Vol. 103, pp. 9637-9649, 1998

[*Langston,* 1979] Langston, C. A., Structure under Mount Rainier, Washington, inferred from teleseismic body waves, *J. Geophys. Res.* Vol. 84, pp. 4749-4762, 1979

[*Lawrence et al.,* 2006] Lawrence, J.F., et al., Crust and upper mantle structure of the Transantarctic Mountains and surrounding regions from receiver functions, surface waves, and gravity: Implications for uplift models , *Geochem. Geophys. Geosyst.*, Vol. 7, 23 pp., Q10011, doi: 10.1029/2006GC001282, 2006

[*LeMasurier and Rex,* 1989] LeMasurier, W., Rex, D., Evolution of linear volcanic ranges in Marie Byrd Land, Antarctica, *J. Geophys. Res.*, Vol. 94, pp. 7223-7236, 1989

[*Lemasurier and Landis,* 1996] Lemasurier, W., Landis, C., Mantle plume activity recorded by low-relief erosion surfaces in West Antarctica and New Zealand, *GSA bulletin*, Vol. 108, No. 11, pp.1450-1466, 1996

[*LeMasurier,* 2008] LeMasurier, W., Neogene extension and basin deepening in the West Antarctic rift inferred from comparisons with the East African rift and other analogs, *Geology*, Vol. 36, pp. 347-250, 2008

[*Luyendyk et al.,* 2003] Luyendyk, B.P., C.H. Smith, G. Druivenga, Gravity measurements on King Edward VII Peninsula, Marie Byrd Land, West Antarctica, during GANOVEX VII, *Geolog. Jahrb.*, Vol. 95, pp. 101-126, 2003

[*Lythe et al.,* 2000] Lythe, M.B., Vaughan, D.G. and the BEDMAP Consortium, *BEDMAP - bed topography of the Antarctic. 1:10,000,000 scale map*, British Antarctic Survey (Misc) 9. Cambridge, British Antarctic Survey, 2000

[*Park and Levin,* 2000] Park, J, Levin V., Receiver functions from multiple-taper spectral correlation estimates, *Bull. Seism. Soc. Am.*, Vol. 90, pp. 1507-1520, 2000

[*Liu and Gao,* 2006] Liu, K., Gao, S., Mantle transition zone discontinuities beneath the Baikal rift and adjacent areas, *J. Geophys. Res.*, Vol. 111, 10 pp., B11301, 2006

[*Lobkis and Weaver,* 2001] Lobkis, O., Weaver, R., On the emergence of the Green's function in the correlations of a diffuse field, *J. Acoust. Soc. Am.*, Vol. 110, pp. 30113017, 2001

[*Margerin et al.,* 2000] Margerin, L., Campillo, M., Von Tiggelen, B., Monte Carlo simulation of multiple scattering of elastic waves, *J. Geophys. Res.*, Vol. 105, pp. 7873-7892, 2000

[*Margerin and Campillo,* 2009] Margerin, L., et al, Energy partition of seismic coda waves in layered media: theory and application to Pinyon Flats Observatory, *Geophys. J. Int.*, Vol. 177, pp. 571-585, 2009

[*McClusky,* 2010] McClusky, S., Kinematics of the southern Red Sea-Afar triple junction and implications for plate dynamics, *Geop. Res. Lett.*, Vol. 37, (5):L05301, 5 pp., doi:10.1029/2009GL041127, 2010

[*Morelli and Danesi,* 2004] Morelli A., Danesi S., Seismological imaging of the Antarctic continental lithosphere: a review, *Global and Planetary Change*, Vol. 42, pp. 155-165, 2004

[*Pollard et al.,* 2005] Pollard, D., DeConto R., Nyblade A., Sensitivity of Cenozoic Antarctic ice sheet variations to geothermal heat flux, *Global and Planetary Change*, Vol. 49, Iss. 1-2, pp. 63-74, 2005

[*Nyblade,* 2011] Nyblade, A., et al., Upper mantle structure beneath the Whitmore Mountains, West Antarctic Rift System, and Marie Byrd Land from Body Wave Tomography, *Eos Trans. AGU, Fall Meet. Suppl.*, 2011

[*Nyblade,* 1999] Nyblade, A.A., Heat flow and the structure of Precambrian lithosphere, *Lithos.*, Vol. 48, pp. 81-91, 1999

[*Oppenheimer and Kyle,* 2008] Oppenheimer, C., Kyle, P.R., Volcanology of Erebus volcano, Antarctica, *J. Volcanol. Geotherm. Res.*, Vol.177, v-vii, 3 pp., 2008

[*Oppenheimer and Kyle,* 2008] Oppenheimer, C., Kyle, P.R., Probing the magma plumbing of Erebus volcano, Antarctica, by open-path FTIR, *J. Volcanol. Geotherm. Res.*, Vol. 177, pp. 743-754, 2008

[*Panter et al.,* 2006] Panter K.S., et al, The origin of HIMU in the SW Pacific; evidence from intraplate volcanism in southern New Zealand and Subantarctic islands, *Journal of Petrology*, Vol. 47, pp. 1673-1704, 2006

[*Panter and Winter,* 2008] Panter K.S., Winter, B., Geology of the side crater of the Erebus volcano, Antarctica, *J. Volcanol. Geotherm. Res.*, Vol. 177 (3), pp. 578-588, doi:10.1016/j.jvolgeores.2008.04.019, 2008

[*Patane et al.,* 2006] Patane, D., et al, Time-resolved seismic tomography detects magma intrusions at Mount Etna, *Science*, Vol. 313, pp. 821-823, 2006

[*Poupinet et al.,* 1996] Poupinet, G.; Ratdomopurbo, A.; Coutant, O., On the use of earthquake multiplets to study fractures and the temporal evolution of an active volcano, Seismic signals on active volcanoes; possible precursors of volcanic eruptions, Nicolosi, Italy, Sept. 21-25, *Ann. Geofis.*, Vol. 39:4, pp. 253-264, 1996

[*Ritzwoller et al.,* 2001] Ritzwoller, M.H., et al., The structure of the crust and upper mantle beneath Antarctica and the surrounding oceans, *J. Geophys. Res.*, Vol. 106(B12), pp. 30645-30670, 2001

[*Rost and Thomas*, 2002] Rost, S., Thomas, C., Array seismology: Methods and applications, *Reviews of Geophyiscs*, Vol. 40, 1008, 27 pp., doi:10.1029/2000RG000100, 2002

[*Roux et al.,* 2005] Roux, P., et al., P-waves from cross-correlation of seismic noise, *Geop. Res. Lett.*, Vol.32, 4 pp., 2005

[*Rowe et al.,* 1998] Rowe, C.A., et al., Seismic and acoustic observations of lava lake explosions at Mount Erebus volcano, Antarctica, *EOS, Trans. AGU* 79(45): S12C-10, Vol. 101, No. 1, pp. 105-128, 1998

[*Ruiz,* 2003] Ruiz, M., Analysis of Tremor Activity at Mt Erebus Volcano, Antarctica, Master's Thesis, New Mexico Tech, 2003

[*Salvini et al.,* 1997] Salvini, F., et al., Cenozoic geodynamics of the Ross Sea region, Antarctica: Crustal extension, intraplate strike-slip faulting, and tectonic inheritance, *J. Geophys. Res.*, Vol. 102, No. B11, 24 pp., 1997

[*Sanchez-Sesma and Campillo,* 2006] Sanchez-Sesma, F., Campillo, M., Retrieval of the Green's function from cross-correlation: The canonical elastic problem, *Bull. Seism. Soc. Am.*, Vol. 96, No. 3, pp.1182-1191, 2006

[*Sato et al.,* 1997] Sato, H., Nakahara, H., Ohtake, M., Synthesis of scattered energy density for nonspherical radiation from a point shear-dislocation source based on the radiative transfer theory, *Phys. Eart. Plan. Int.*, Vol. 104, pp. 1-13, 1997

[*Sens-Schonfelder and Wegler,* 2006] Sens-Schonfelder, C., Wegler, U., Passive image interferometry and seasonal variations of seismic velocities at Merapi Volcano, Indonesia, *Geop. Res. Lett.*, Vol. 33, 5 pp., 2006

[*Shapiro,* 2004] Shapiro, N., Campillo, M., Emergence of broadband Rayleigh waves from correlations of the mabient seismic noise, *Geop. Res. Lett.*, Vol. 31, 5 pp., 2004

[*Shapiro et al.,* 2005] Shapiro, N. M., et al., M., High resolution surface-wave tomography from ambient seismic noise, *Science*, Vol. 307, pp. 16151618, 2005

[*Shaw et al.,* 1991] Shaw, H.R., Chouet, B., Fractal properties of magma transport in Hawaii and critical self-organization of Tremor, *J. Geophys. Res.*, Vol. 96, pp. 931-945, 1991

[*Sheehan et al.*, 1991] Sheehan, A., et al., Collaborative Research: Measurements of Crustal Deformation and a Multidisciplinary Geophysical Investigation of the Rio Grande Rift, Earthscope, NSF 0454541, 2012

[*Shibuya et al.,* 1983] Shibuya, K., et al., Study of the seismic and volcanic activity of Mount Erebus, Antarctica, 1981-1982, in Proceedings of 3rd Symposium on Antarctic Geoscience, *Mem.Nat.Inst.Pol.Res.*, Tokyo Special Issue, Vol. 28, pp. 54-66, 1983

[*Shuler et al.,* 2008] Shuler, A., et al., Ambient Noise Tomography at Bezymianny Volcano, Kamchatka, *AGU fall meeting*, 2008

[*Sieminski et al.,* 2003] Sieminski A., E. Debayle, J. Leveque, Seismic evidence for deep low-velocity anomalies in the transition zone beneath West Antarctica, *Earth Planet. Sci. Lett.*, Vol. 216, pp. 645-661, 2003

[*Snieder,* 2004] Snieder, R., Extracting the Green's function from the correlation of coda waves: A derivation based on stationary phase, *Phys. Rev. E*, Vol. 69, 046,610, 8 pp., 2004

[*Snieder and Haggerty,* 2004] Snieder, R., Haggerty, M, Monitoring a temporal change of seismic velocity in a volcano: Application to the 1992 eruption of Mt. Merapi, *Geop. Res. Lett.*, Vol. 22, pp. 775-778, 2004

[*Snieder,* 2006] Snieder, R., et al, Spatial variation in Mount St. Helens clones from coda wave analysis, Center for Wave Phenomena, *cwp543*, 6 pp., 2006

[*Studinger et al.,* 2006] Studinger, M.R., et al., Crustal architecture of the Transantarctic between the Scott and Reedy Glacier Region and South Pole from aerogeophysical data, *Earth Planet. Sci. Lett.*, Vol. 250, pp. 182-199, 2006

[*Sun et al.,* 2011] Sun, X., et al., Crust and upper mantle structure beneath Antarctica from seismic ambient noise study, *Eos Trans. AGU, Fall Meet. Suppl.*, 2011

[*Tiberi et al*, 2003] Tiberi C., et al., Deep structure of the Baikal rift zone revealed by joint inversion of gravity and seismology, *J. Geophys. Res.*, Vol. 108, No .B3, 2133, 15 pp., 2003

[*Tonegawa et al.,* 2009] Tonegawa, T., et al., Seismic interferometry of teleseismic S-wave coda for retrieval of body waves: an application to the Philippine Sea slab underneath the Japanese Islands, *Geophys. J .Int.*, vol.178, pp. 1574-1586, 2009

[*Tonegawa,* 2010] Tonegawa, T., Kiwawu, N., Inter-source body wave propagations derived from seismic interferometry, *Geophys. J. Int.*, Vol.183, pp. 861-868, 2010

[*Van Manen et al.,* 2006] Van Manen, D, Curtis, A., Robertsson, J., Interferometric modeling of wave propagation in inhomogeneous elastic media using time reversal and reciprocity, *Geophysics*, Vol.71, No. 4, 49 pp., 2006

[*Van Tiggelen,* 2003] Van Tiggelen, B., Green function retrieval and time reversal in a disordered world, *Phys. Rev. Lett.*, Vol. 91, 243904, 4 pp., 2003

[*Wannamaker et al.,* 1996] Wannamaker, P.E., Stodt, J.A., and Olsen, L., Dormant state of rifting below the Byrd subglacial basin, West Antarctica, implied by magnetotelluric (MT) profiling, *Geop. Res. Lett.*, Vol. 23, pp. 29832986, 1996

[*Wapenaar et al.,* 2004] Wapenaar, K.,Thorbecke, J., Draganov, D., Relations between reflection and transmission responses of three-dimensional inhomogeneous medias, *Geophys. J. Int.*, Vol. 156, pp. 179-194, 2004

[*Wapenaar,* 2006] Wapenaar, K.,Fokkema, J. , Green's function representations for seismic interferometry, *Geophysics*, Vol. 71, pp. 33-46, 2006

[*Watson et al.,* 2006] Watson, T., et al., P and S velocity structure of the upper mantle beneath the Transantarctic Mountains, East Antarctic craton, and Ross Sea from travel time tomography, *Geochem., Geophys. Geosyst.*, Vol. 7, Q07005, 17 pp., 2006

[*Weaver and Lobkis,* 2004] Weaver, R., Lobkis, O., Diffuse fields in open systems and the emergence of the Green's function, *J. Acoustic. Soc. Am.*, Vol. 116, pp. 2731-2734, 2004

[*Wiens,* 2006] Wiens, D., et al., P and S velocity structure of the upper mantle beneath the Transantarctic Mountains, East Antarctic craton, and Ross Sea from travel time tomography, *Geochem., Geophys. Geosyst.*, Vol. 7, Q07005, 17 pp., 2006

[*Wilch et al.*, 1993] Wilch, T.I., et al., Minimal PliocenePleistocene uplift of the dry valleys sector of the Transantarctic Mountains: a key parameter in ice sheet reconstructions, *Geology*, Vol. 21, pp. 841844, 1993

[*Wilch and McIntosh*, 2000] Wilch,T.I., McIntosh, W.C., Eocene and Oligocene volcanism at Mount Petras, Marie Byrd Land: implications for middle Cenozoic ice sheet reconstructions in West Antarctica, *Antarctic Science*, Vol. 12, Iss. 4, pp. 477-491, 2000

[*Wilson et al.*, 2005] Wilson, D., et al., Lithospheric Structure of the Rio Grande Rift, *Nature*, Vol. 433, doi:10.1038/nature03297, 4 pp., 2005

[*Wilson and Aster*, 2005] Wilson, D., R. Aster, Seismic imaging of the crust and uppermantle using regularized joint receiver functions,frequency.wave number filtering, and multimode Kirchhoff migration, *J. Geophys. Res.*, Vol. 110, B05305, doi:10.1029/2004JB003430, 12 pp., 2005

[*Winberry*, 2004] Winberry,. J., Anandankrishnan, S., Crustal structure of the West Antarctic rift system and Marie Byrd Land hotspot, *Geology*, Vol. 32, No. 1, pp. 977-980, 2004

[*Anandakrishnan and Winberry*, 2004] Anandakrishnan S., P. Winberry, Antarctic subglacial sedimentary layer thickness from receiver function analysis. *Global and Planetary Change*, Vol. 42, pp. 167-176, 2004

[*Yamamoto*, 2010] Yamamoto, M., Sato, H., Multiple scattering and mode conversion revealed by an active seismic experiment at Asama volcano, Japan, *J. Geophys. Res.*, Vol. 115, 14 pp., 2010

[*Zandomeneghi et al.*, 2012] Zandomeneghi, D., et al., Internal structure of Erebus volcano, Antarctica imaged by high-resolution active-source tomography, submitted, *J. Geophys. Res.*, 2012

[*Zheng et al.*, 2008] Zheng, S., et al, Surface wave tomography of China from ambient seismic noise correlation, *Geochem., Geophys. Geosyst.*, Vol. 9, No.5, 8 pp., 2008

[*Zhu and Kanamori*, 2000] Zhu, L., H. Kanamori, Moho depth variation in southern California from teleseismic receiver functions, *J. Geophys. Res.*, Vol. 105, pp. 2969-2980, 2000